Unravelling CO2 and Electrolyte effects in Bubbly Flows

Interplay between Rheology, Hydrodynamics and Mass Transfer

Mandalahalli, M.M.

DOI
10.4233/uuid:1de807c4-25f1-4d56-b9a8-dedb9d4637c1

Publication date
2024

Document Version
Final published version

Citation (APA)
Mandalahalli, M. M. (2024). *Unravelling CO2 and Electrolyte effects in Bubbly Flows: Interplay between Rheology, Hydrodynamics and Mass Transfer*. [Dissertation (TU Delft), Delft University of Technology]. https://doi.org/10.4233/uuid:1de807c4-25f1-4d56-b9a8-dedb9d4637c1

UNRAVELLING CO_2 AND ELECTROLYTE EFFECTS IN BUBBLY FLOWS

INTERPLAY BETWEEN RHEOLOGY, HYDRODYNAMICS AND MASS TRANSFER

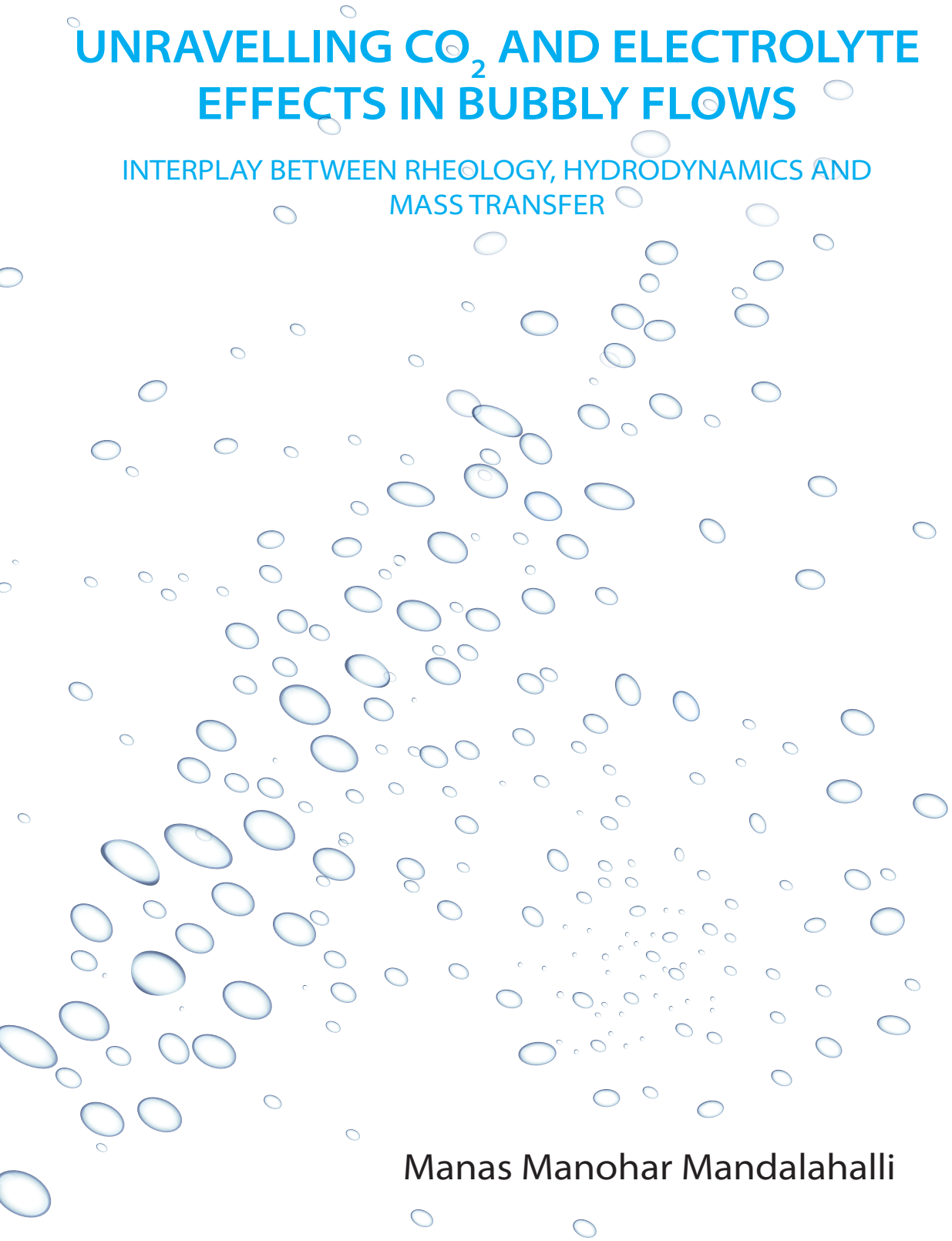

Manas Manohar Mandalahalli

Propositions

accompanying the dissertation

UNRAVELLING CO_2 AND ELECTROLYTE EFFECTS IN BUBBLY FLOWS

INTERPLAY BETWEEN RHEOLOGY, HYDRODYNAMICS AND MASS TRANSFER

by

Manas Manohar MANDALAHALLI

1. Simplifying small-scale interactions in multiphase flows creates pathways in reducing empiricism involved in designing large-scale systems.
   (*Chapter 1 & 5, this thesis*)

2. Characterizing the bubble size distribution where they are generated is sufficient to describe the overall hydrodynamics in electrolyzers. (*Chapter 2, this thesis*)

3. Contrary to a single bubble rise in a liquid with surfactants, single bubble rise in electrolyte solutions exhibits a *pure-liquid* type behaviour; this can be attributed to the fast diffusion of ions between the bulk and the gas-liquid interface.
   (*Chapter 3, this thesis*)

4. The obscure nature of contaminant influences should be decoupled from the wake effects, in understanding the interplay between a single bubble rise and interfacial mass transfer. (*Chapter 4, this thesis*)

5. Dimensional analysis follows the causality principle, correlation does not necessarily reflect the underlying mechanisms.

6. In order to be meaningful, small scale research into novel materials and processes should involve an analysis of techno-economics and scalability.

7. Propaganda of unity masks the true economics in a union of (nation) states, challenged by an imposition of uniformity.

8. Social welfare system is a privilege for rich countries, paid for by its capitalistic economy.

9. Effectiveness of an industry-academia collaboration can be greatly enhanced if the industry is honest about its challenges & academia of its intentions.

10. The location and the extracurriculars make a conference more attractive than its content.

11. Universities seeking a higher international outlook need to consider the societal consequences of a large international student population.

12. "Radioactive" debate surrounding nuclear energy waste is limiting the society from harnessing its potential as a clean energy source.

These propositions are regarded as opposable and defendable, and have been approved as such by the promotor prof. dr. R.F Mudde and co-promotor dr. eng. L.M. Portela.

Stellingen

behorende bij het proefschrift

UNRAVELLING CO_2 AND ELECTROLYTE EFFECTS IN BUBBLY FLOWS

INTERPLAY BETWEEN RHEOLOGY, HYDRODYNAMICS AND MASS TRANSFER

door

Manas Manohar MANDALAHALLI

1. Het vereenvoudigen van interacties op kleine schaal vermindert de behoefte voor empirische modellen voor het ontwerp van systemen op grote schaal . (*Hoofdstuk 1 & 5, dit proefschrift*)
2. Het karakteriseren van de belgrooteverdeling op de locatie van het onstaan van de bellen is voldoende om de de globale hydrodynamica in elektrolyse processen te beschrijven. (*Hoofdstuk 2, dit proefschrift*).
3. Ten opzichte van een enkele bel die stijgt in een vloeistof met oppervlakteactieve stoffen, enkele bellen die stijgen in een elektrolytoplossing vertonen gedrag zoals gezien in *zuivere vloeistoffen*; dit kan verklaard worden door de snelle diffusie van ionen tussen de massa en het gas-vloeistof oppervlak. (*Hoofdstuk 3, dit proefschrift*)
4. Het obscure effect van verontreiniging moet apart gezien worden van de effecten van het zog in het begrijpen van de interactie tussen een enkel stijgende bel en massaoverdracht door het grensvlak. (*Hoofdstuk 4, dit proefschrift*)
5. Dimensieanalyse voldoet aan het causaliteitsprincipe; correlatie beschrijft niet noodzakelijkerwijs het onderliggende mechanisme.
6. Voor een zinvolle studie, onderzoek op laboratorium schaal naar nieuwe materialen en processen moet ook een analyse bevatten van de techno-economische haalbaarheid en mogelijkheid tot opschaling.
7. Eenheidspropaganda verdoezelt de werkelijke staat van de economie in een unie van (natie)staten, welke is uitgedaagd door een oplegging van uniformiteit.
8. Sociaal welzijn is een voorrecht voor rijke landen en is betaald door zijn kapitalistische economie.
9. De effectiviteit van een industriële en academische samenwerking kan in grote mate vergroot worden wanneer de industriële partner eerlijk is over zijn uitdagingen en de academische over zijn intenties.
10. De locatie en de bijkomstigheden maken een conferentie meer aantrekkelijk dan haar eigen inhoud.
11. Universiteiten die een hogere internationale status zoeken moeten de gemeenschappelijke consequenties van een grote aanwezigheid internationale studenten beschouwen.
12. Radioactieve debatten over kernafval limiteert de gemeenschap in het gebruik van een potentieel schone energiebron.

Deze stellingen worden opponeerbaar en verdedigbaar geacht en zijn als zodanig goedgekeurd door de promotor prof. dr. R.F Mudde and co-promotor dr. eng. L.M. Portela.

Unravelling CO_2 and Electrolyte effects in Bubbly Flows

Interplay between Rheology, Hydrodynamics and Mass Transfer

UNRAVELLING CO_2 AND ELECTROLYTE EFFECTS IN BUBBLY FLOWS

INTERPLAY BETWEEN RHEOLOGY, HYDRODYNAMICS AND MASS TRANSFER

Dissertation

for the purpose of obtaining the degree of doctor
at Delft University of Technology,
by the authority of the Rector Magnificus prof. dr. ir. T.H.J.J. van der Hagen,
chair of the Board of Doctorates,
to be defended publicly on 04 June 2024 at 1500 hrs

———

by

Manas Manohar MANDALAHALLI

Master of Science in Chemical Engineering, University of Twente, the Netherlands
born in Hindupur, India

This dissertation has been approved by the promotors.

promotor: Prof. dr. R.F. Mudde
copromotor: Dr. Eng. L.M. Portela

Composition of the doctoral committee:

Rector Magnificus,	chairperson
Prof. dr. R.F. Mudde,	Delft University of Technology, promotor
Dr. Eng. L.M. Portela,	Delft University of Technology, copromotor
Independent members:	
Prof. dr. ir. J. T. Padding,	Delft University of Technology, NL
Prof. dr. ir. C. Poelma,	Delft University of Technology, NL
Prof. dr. ir. J. A. M. Kuipers,	Eindhoven University of Technology, NL
Prof. dr. A. Tomiyama,	Kobe University, Japan
Prof. dr. D. Legendre,	IMF Toulouse, France

The research reported in this work is part of the Industrial Partnership Programme *i36 Dense Bubbly Flows* that is carried out under an agreement between Nouryon Speciality Chemicals B.V., DSM Innovation Center B.V., SABIC Global Technologies B.V., Shell Global Solutions B.V., Tata Steel Nederland Technology B.V. and the Netherlands Organisation for Scientific Research (NWO).

Nederlandse titel : Ontrafelen van CO_2- en elektrolyteffecten in Bubbelstromen: Wisselwerking tussen Reologie, Hydrodynamica en Massaoverdracht

Keywords:	Mass transfer, Electrolytes, Bubble dynamics, Experiments
Printed by:	Proefschriftmaken B.V.
Front & Back:	Illustrations of a bubble plume & a bubble column with electrolyte ions and CO_2 molecules.

ISBN: 978-94-6384-587-8

An electronic version of this dissertation is available at
http://repository.tudelft.nl/.

“Science is concerned with what is possible
while engineering is concerned with choosing,
from among the many ways possible ways,
one that meets a number of often
poorly stated economic and practical objectives.”

~ Richard Hamming

“vipaTTi Se badhakar aNubhav SikhaaNe vaaLaa viDyaaLay
Naa To aaj Tak khuLaa hai Naa kabhii khuLegaa. ”

“There is no greater school that teaches life experiences than its own challenges.”

~ Munshi Premchand

CONTENTS

SUMMARY

Bubbly flows are ubiquitously found in natural systems and are widely used in (bio)-chemical and energy-producing processes. A variety of design options, ease of maintenance, and a large operability window make bubble columns a commonplace across industries, ranging from oil processing to biotechnology and electrolyzers. Despite their wide applicability and advantages, the complexity of designing and optimizing large-scale bubble columns arises from inherent multiphysics - multiscale phenomena. The design and scale-up methodologies, from laboratory to large-scale, require a detailed understanding of the interplay between the different physical phenomena and processes, for a variety of fluid compositions and operation conditions, at various scales: from single bubbles to dense bubbly flows in industrial situations. For example: (i) the interplay between rheology, hydrodynamics and interfacial phenomena for a single bubble; (ii) the interplay between the collective dynamics of the bubbles inside the column, the bubble size distribution and the bubble generation process.

The current thesis, a part of an industry-academia partnership programme, is aimed at getting a better fundamental understanding of the interplay between the different physical phenomena and processes in bubble flows, inspired by two practical cases: CO_2 absorption and electrolysis. In addressing questions relevant to specific processes, the vast body of literature available on bubble hydrodynamics needs to be considered. In **Chapter 1**, we provide a simplified overview of the current knowledge-base on micro-(single bubble), meso-(bubble clusters), and macro-scales (dense flow), and on the interplay between single-bubble phenomena, collective dynamics of bubbles and bubble size distribution. The key missing aspects from the literature form the basis for key research questions: (i) how does electrolyte-induced inhibition of bubble coalescence affects the hydrodynamics in a dense recirculating flow?; (ii) how does electrolytes at high concentrations affect the rise of a single ellipsoidal bubble?; (iii) how does bubble shrinkage influence the rise characteristics of a single bubble?; (iv) what is the role of bubble shape and path oscillations in the interplay between hydrodynamics and mass transfer?

In the case of electrolysis, a practical challenge arises from the presence of large quantities of sub-millimeter size bubbles; these small bubbles, upon generation, occupy the electrode surface and reduce the overall efficiency of the process. A gaslift electrolyzer design is often adopted, wherein the liquid recirculation aids in removing bubbles from the surface. The large quantities (a few mol/liter) of electrolytes used, and their effect on the inhibition of coalescence between two bubbles, play a key role here. In **Chapter 2**, we study the role of electrolytes on overall hydrodynamics in a recirculating bubble column (gas fractions up to about 15%), employing a microporous sparger mimick the role of an electrode surface. Due to the opaqueness at high gas fractions, a combination of X-ray imaging (for gas fraction), high-speed imaging (for bubble size distribution), and bubble imaging velocimetry (for bubble velocity) was employed in characterizing the hydrodynamics. While ellipsoidal bubbles (2-3 mm) were observed for water, the addition of electrolytes (up to 2 mol/liter NaCl) leads to an increasing fraction

of microbubbles (~ 200-300 μm). We conclude that the knowledge of the bubble size distribution of the bubbles generated at the sparger is sufficient to describe the overall hydrodynamics of the column; smaller bubbles, as a consequence of electrolytes, cause foaming at the free surface and recirculate in the column, reducing the circulation velocity. Based on our results, we develop a simple quasi-1D mechanistic model, which gives reasonable quantitative prediction of the overall hydrodynamics of the column.

In **Chapter 3**, we investigate the role of (chlorate) electrolysis conditions, a high concentration of single & mixed electrolytes in water, at temperatures up to 80°C, on the rise of a single ellipsoidal H_2 bubble. Bubbles in the ellipsoidal regime can exhibit a complex interplay between bubble motion and rheology; the presence of contaminants in the liquid can introduce additional rheological effects at the interface, deviating from well-known correlations for pure liquids. Electrolytes, along with other solutes used in (bio)-chemical processes (surfactants, organics, alcohols), are generally classified as contaminants in the literature. In contrast to such generalization, we observe that for electrolytes at high concentrations, at all temperatures, the bubbles exhibit a pure-liquid type of behaviour; knowledge of bulk physical properties (density, viscosity, and static surface tension) is sufficient to describe the bubble rise characteristics, using well-known non-dimensional correlations for pure liquids.

For the case of CO_2 absorption, often employed in carbon capture systems, the design process relies on an understanding of the interplay between bubble hydrodynamics and gas-liquid mass transfer. This interplay for a single bubble is characterized using the mass transfer coefficient, k_L, a design parameter often obtained from classical models based on interfacial mobility. These models, based on potential/Stokes flow around a spherical bubble, do not agree with the experimental results for larger ellipsoidal and wobbly bubbles (those most found in industrial bubble columns); a deviation often attributed to a possible presence of contaminants in the liquid. In **Chapter 4**, we study the rise of a single CO_2 bubble in water, using fluorescence imaging (for dissolved CO_2 concentration) and bubble tracking (bubble size, shape, and path). We show that the bubble rise velocities exhibit a free-slip pure water behaviour and that the mass transfer is quasi-steady in nature, with equally-sized shrinking CO_2 and non-shrinking N_2 bubbles showing a similar bubble motion. We demonstrate that the wake effects, associated with shape and path oscillations, not included in classical models, play a strong role in describing the interplay between hydrodynamics and mass transfer for ellipsoidal and wobbly bubbles. The wake effects and the differences in hydrodynamics between spherical bubbles and ellipsoidal, and wobbly bubbles, and not contaminant effects, can explain why models based on potential/Stokes flow around a spherical bubble do not provide a good result for ellipsoidal and wobbly bubbles. Based on an analogy between the momentum and mass transfer, we provide a mechanistic correlation that can be used to predict k_L in the ellipsoidal and wobbly regimes, based on knowledge of bubble hydrodynamics.

In the **Appendix A**, we present the results we obtained for a dilute bubble column (without recirculation), for N_2 bubbles with electrolytes (without mass transfer) and for CO_2 bubbles in pure water (with mass transfer). We observe a transition from a homogeneous flow regime (for the case of N_2 in water) to a pseudo-heterogeneous regime with an oscillatory plume. This is due to a change in the bubble size distribution, which is a consequence of: (i) the mass transfer for the CO_2 bubbles in water; (ii) the influ-

ence of the electrolytes on the bubble generation process, for the N_2 bubbles with electrolytes. We also observed that for CO_2 bybbbles in electrolyte solutions, there also exists a transition from homogeneous to a pseudo-heterogeneous regime, with an oscillatory bubble plume. A natural extension of the work (not presented in this thesis) would be a parametrization of the bubble plume dynamics, addressing the individual and collective effects of electrolytes and gas-liquid mass transfer through its influence on the bubble size distribution.

Overall, in this thesis we show how the understanding and decoupling of the different physical phenomena that occur simultaneously in bubble flows can play an important role in the description, improvement and design of complex industrial processes. We were inspired by two practical industrial cases, CO_2 absorption and electrolysis, however, this type of approach can be applied to many other industrial situations. The understanding of the interplay between the different physical phenomena and processes, together with a mechanistic approach, can steer detailed experimental and numerical investigations, and lead to pragmatic non-dimensional correlations with a sound physical basis. Ultimately, this will help in the development of better scale-up methodologies and in the design of more efficient complex industrial processes.

SAMENVATTING

Bellenstromen zijn alomtegenwoordig. Deze meerfasestromingen komen voor in natuurlijke ecosystemen en hebben toepassingen in de (bio-)chemische industrie en energievoorziening. Een verscheidenheid aan ontwerpmogelijkheden, gemak in onderhoud, en wijde inzetbaarheid maken bellenkolommen onmisbaar in verschillende industrieën, variërend van olieraffinage, biotechnologische processen en elektrolyse. Ondanks de brede toepasbaarheid en voordelen is de complexiteit van het ontwerp en het optimaliseren van grootschalige bellenkolomen te wijten aan de samengaande meerschalige en veelomvattende physica. De methodologie van het ontwerpen en het opschalen van laboratorium tot industriële schaal, vereist een gedetailleerde kennis van de wisselwerking tussen de verschillende natuurkundige eigenschappen, verschijnselen en processen, als ook voor een scala aan vloeistofsamenstellingen en een verscheidenheid aan omstandigheden op verschillende lengteschalen: van enkele bellen tot dichte bubbelstromen in industriële processen. Bijvoorbeeld: (i) de wisselwerking tussen reologie, vloeistofdynamica en oppervlakteverschijnselen voor een enkele bel; (ii) de wisselwerking tussen het collectieve gedrag van bellen in een bellenstroom in de kolom, de belgrootteverdeling en de methode van belinjectie.

Dit proefschrift, als onderdeel van een academisch en industrieel samenwerkingsprogramma richt zich op het verbeteren van de fundamentele kennis van de wisselwerking tussen verschillende fysische verschijnselen en processen in bellenstromen geinspireerd door twee praktische toepassingen: koolstofdioxide (CO_2) absorptie en electrolyse. De beschikbare literatuur over de hydrodynamica van bellen is in acht genomen om de onderzoeksvragen relevant aan deze specifieke processen op te stellen en te beantwoorden. **Hoofdstuk 1** geeft een vereenvoudigde weergave van de huidige kennis over micro- (enkele bel), meso- (bellenzwerm), en macroschaal (bellenstroom), en over de wisselwerking tussen microschaal, collectief dynamisch gedrag van bellen en de belgrootteverdeling. Een belangrijk aspect dat afwezig is in de literatuur vormt de basis voor de hier gestelde belangrijke onderzoeksvragen: (i) hoe beinvloedt de elektrolyt gestimuleerde remming van bellen-coalescentie de hydrodynamica in een geconcentreerde circulerende stroming?; (ii) hoe beinvloedt een hoge concentratie elektrolyt het stijggedrag van enkele ellipsvormige bellen?; (iii) hoe beinvloedt het krimpen van bellen de karakteristieke stijging (stijgsnelheid) van een enkele bel?; (iv) wat is de rol van de belvorm en oscillaties in het stromingstraject op de wisselwerking tussen vloeistofmechanica en massaoverdracht?

In het geval van electrolyse, een praktische uitdaging komt voort uit de aanwezigheid van grote hoeveelheden belletjes met een diameter kleiner dan een millimeter; wanneer deze belletjes worden gevormd hechten ze aan het elektrodeoppervlak en reduceren ze de efficiëntie van het hele proces. Een gaslift ontwerp voor een electrolyseproces is er één waarbij de vloeistofrecirculatie bijdraagt aan het verwijderen van belletjes die gehecht zijn aan het elektrodeoppervlak. De grote hoeveelheden (enkele molair) van gebruikt elektrolyt en zijn effect op de vermindering van bellen-coalescentie speelt een

grote rol hierin. **Hoofdstuk 2** beschrijft de rol van elektrolyt op de globale vloeistofdynamica in een bellenkolom met recirculatie (met gasfracties tot ongeveer 15%), waarbij een microporeuse belinjector was gebruikt om de rol van een elektrodeoppervlak na te bootsen. Door de troebelheid van het vloeistof-gas mengsel bij hogere gasfracties, een combinatie van Röntgenfotografie (voor gasfracties) en hogesnelheidsfotografie (voor belgrootteverdeling) en belfotosnelheidsmeting (voor bel snelheden) was gebruikt om de vloeistofdynamica te observeren. Terwijl ellipsvormige bellen (2-3 mm) werden gevormd in water, het toevoegen van elektrolyt (tot 2 molair NaCl) resulteerde in een toename van microbellen in de grootte van ~ 200-300 μm. We concludeerden dat kennis van de belgrootteverdeling van de bellen gevormd door de injector voldoende is om de globale hydrodynamica van de kolom te beschrijven; kleine bellen, als gevolg van de elektrolyt, veroorzaakte schuimvorming op het vrije oppervlak dat recirculeerde in de kolom en daarbij de circulatiesnelheid verkleinde. Gebaseerd op deze resultaten hebben we een eenvoudig quasi-ééndimensionaal mechanistich model ontwiddeld dat de globale hydrodynamica van de kolom beschrijft met aanvaardbare kwantitatieve nauwkeurigheid.

Hoofdstuk 3 bespreekt de rol van (chloraat) electrolyse omstandigheden, een hoge concentratie van enkelvoudige & gemengde elektrolyten in water op het opstijgen van enkele ellipsvormige waterstofbelletjes (H_2) bij temperaturen tot 80°C . Bellen in het ellipsvormige domein kunnen een complexe wisselwerking teweeg brengen tussen de beweging van de bel en de reologie van de vloeistof; de aanwezigheid van verontreiniging in de vloeistof kan aanvullende reologische effecten introduceren aan het oppervlak, afwijkend van bekende correlaties voor zuivere vloeistoffen. Elektrolyten, evenals andere opgeloste stoffen die worden gebruikt in (bio-)chemische processen (zoals oppervlakteactieve stoffen, organische stoffen, en alcoholen) zijn in de literatuur over het algemeen gecategoriseerd als verontreiniging. In tegenstelling tot zulke generalisaties, observeerden we dat voor hoge concentraties elektrolyt en bij elke temperatuur, de bellen, met kennis van stofmengseleigenschappen (dichtheid, viscositeit, statische oppervlaktespaning), een zuiver-vloeistof type gedrag vertoonden welke voldoende is om de belstijgkarakteristieken te beschrijven met welbekende dimensieloze correlaties voor zuivere vloeistoffen.

In het geval van koolstofdioxide absorptie, vaak gebruikt in koolstofafvang en -opslag systemen, steunt het ontwerp van zulke processen op kennis van de wisselwerking tussen de vloeistofmechanica van bellen en massa overdracht tussen gas en vloeistof. Deze wisselwerking voor enkele bellen is gekenmerkt bij het gebruik van de massaoverdrachtscoefficient, k_L, als een ontwerpvariabele die vaak wordt afgeleid van klassieke modellen gebaseerd op de mobiliteit van het oppervlak. Deze modellen, gegrond op potentiaal(niet-roterende) stroming of Stokes stroming langs een bolvormige bel, komen niet overeen met de experimentele resultaten voor grotere ellipsvormige en wiebelende bellen (meest voorkomend in industriële bellenkolommen); een afwijking is vaak toegeschreven aan de mogelijke aanwezigheid van verontreiniging in de vloeistof. In **Hoofdstuk 4** bestudeerden we de stijging van een enkele CO_2 bel in water met gebruik van fluorescentiefotografie (voor concentraties opgeloste CO_2) en hogesnelheidsfotografie (belgrootte, vorm, en afgelegd traject). We laten zien dat de stijgsnelheid gedrag vertoonde gebaseerd op de free-slip (wrijvingsloos oppervlak) voorwaarde in zuiver water en dat de massa overdracht van nature quasi-statisch is, met krimpende CO_2 bellen en niet-

krimpende N_2 bellen met gelijke grootte die vergelijkbare beweging van de bellen laten zien. We demonstreerden dat de effecten van het zog, gerelateerd aan oscillaties van de belvorm en zijn stijgtraject, die niet zijn opgenomen in klassieke modellen, een sterke rol hebben in het beschrijven van de wisselwerking tussen de vloeistofmechanica en massaoverdracht voor ellipsvormige en wiebelende bellen. De effecten van het zog en de verschillen in hydrodynamica tussen bol- en ellipsvormige bellen, en waggelende bellen, en niet het effect van verontreiniging, kan verklaren waarom modellen gebaseerd op potentiaal-/Stokes stroming rond een sferische bel geen goed resultaat opleveren voor ellipsvormige wankelende bellen. Gebaseerd op een analogie met de overdracht van impuls en massa, verstrekken wij een mechanistisch model gebaseerd op principes uit de stromingsleer dat gebruikt kan worden om de massaoverdrachtscoëfficient k_L te schatten in het domein van ellipsvormige en wiegelende bellen,.

In **Appendix A**, kunt u de resultaten vinden die we hebben gevonden voor een bellenstroom met lage gasfractie (zonder recirculatie), voor stikstof bellen met elektrolyt (en zonder massaoverdracht) en voor koolstofdioxide bellen in zuiver water (met massaoverdracht). We observeerden een omslagpunt tussen een homogeen stromingsprofiel (voor N_2 in water) tot een pseudo-heterogeen stromingsprofiel met een slingerende bellentrein. Dit komt door een verandering in de belgrootteverdeling, welke een gevolg is van: (i) de massaoverdracht van CO_2 bellen in water; en (ii) de invloed van de elektrolyt op het belvormingsproces voor N_2 bellen met elektrolyt. Daarnaast vonden we dat voor CO_2 bellen in een elektrolytoplossingen er ook een overgang is tussen een homogeen en pseudo-heterogeen stromingsprofiel, met een schommelende bellentrein. Een natuurlijke vervolgstap (niet beschreven in dit proefschrift) zou een parametrische studie zijn naar de dynamiek van een bellentrein en daarbij de individuele en collectieve effecten addresseren van de elektrolyt en gas-vloeistof massa overdracht dat door de belgrootteverdeling beïnvloed is.

Samenvattend, dit proefschrift laat zien hoe kennis en ontkoppeling van de verschillende natuurkundige verschijnselen die gelijktijdig optreden in bellenstromen een belangrijke rol spelen in het beschrijven, verbeteren en ontwerpen van complexe industriële processen. Hoewel geïnspireerd door twee industriële praktijksituaties, CO_2 absorptie en electrolyse, dit type aanpak kan toegepast worden op een verscheidenheid aan industriële situaties. Het begrijpen van de wisselwerking tussen de verschillende natuurkundige verschijnselen en processen, tezamen met een mechanistische aanpak kan aanzet geven tot gedetailleerde experimentele en numerieke studies en leiden tot een pragmatische dimensieloze correlatie gegrond op een solide natuurwetenschappelijke basis. Uiteindelijk zal dit de ontwikkeling en opschalingscapaciteit bevorderen voor het ontwerp van meer efficiënte complexe industriële processen.

1

INTRODUCTION

BUbbly flows are ubiquitously found in many natural processes and industrial applications. Examples of industrial implementations using gas-liquid flows include: absorption columns for CO_2 capture [1], bioreactors for fermentation [2], Fischer - Tropsch liquefaction to produce transport fuels [3], prevention of salt water intrusion in shipping locks [4], mineral processing from ore [5], wastewater treatment [6] and many more. Depending on the nature of the application, gas bubbles are used for the purposes of mixing the liquid phase (with or without presence of dispersed solids), transfer of gaseous reactants into liquid and/or stripping of the reacted products. Due to advantages of low operational costs, easy maintenance and good heat & mass transfer characteristics [7, 8], bubble columns are commonly used equipment. The simplest form of a bubble column consists of a vertical tuble filled with liquid and gas bubbles injected through a sparger at the bottom, however, quite often different types of internals are placed inside the vertical tube. The buoyancy force of the bubbles can also be used to induce a global circulation, leading to a gaslift column. Understanding transport mechanisms and operational parameters in bubble columns has received considerable attention in the past decades.

1.1. A MULTISCALE & MULTIPHYSICS CHALLENGE

The inherent multi-scale multi-phase phenomena, involving hydrodynamics, mass and heat transfer, in industrial bubble columns, makes a rational design, scale-up and optimization rather challenging. Scale-down pilot studies are useful in developing an empirical knowledge of how design (reactor sizing, internals, sparger type) and operational parameters (pressure, temperature, gas & liquid flow rates) determine the flow behaviour (bubble size distribution, gas holdup, flow regime) and the reactor performance (product yield, kinetics) [e.g. 9–11]. The size distribution of the bubbles generated at the sparger strongly depend on the nature of the sparger, the fluid properties and the operational parameters.

An enervating aspect is the range of scales (Figure 1.1) involved in large scale equipment of size $\sim \mathcal{O}10^1$ [m], where bubble sizes are in the range 10^{-3} - 10^{-2}[m] and the

turbulent flow can have length scales smaller than 10^{-3} [m]. Mesoscale interactions in bubble swarms are influenced by bubble coalescence/breakup and *interfacial* heat and mass transfer, occuring at a further 2-3 orders of magnitude below the smallest bubble size [12]. A phenomenological understanding of the interrelations between hydrodynamics, mass and heat transfer, towards creating designs for practical industrial systems is one of the core issues in the field of chemical (reactor) engineering.

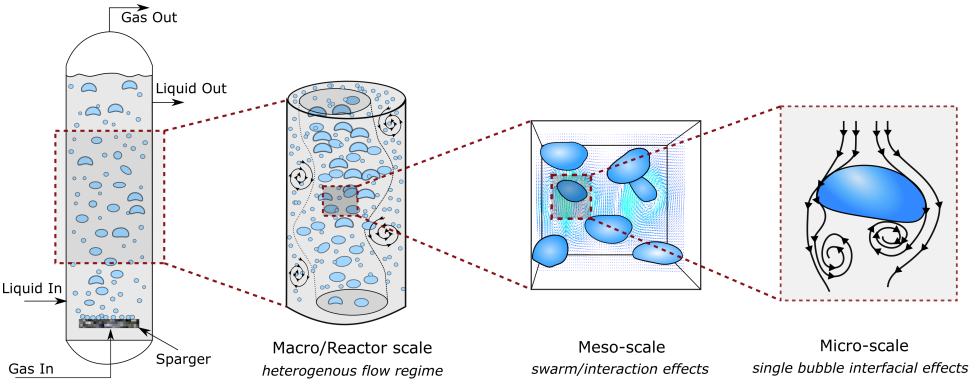

Figure 1.1: Schematic of multiscale phenomena in a bubble column.

THE MICRO-SCALE

A better understanding of the micro-scale phenomena in bubbly flows, i.e. single bubble rise dynamics along with interfacial processes, can reinforce the knowledge at the meso-scale. However, even the elementary situation of a single bubble rising in a quiescent liquid is intricate, due to complex shape changes associated with the interaction of the bubble with its surrounding liquid. Considering a pure liquid case and neglecting the influence of gas properties (viscosity & density), the physical description of the bubble motion involves five parameters: liquid properties (density ρ, viscosity μ, and the surface tension σ), volume based bubble-equivalent diameter d_{eq} and gravity g.

The physical analysis of the bubble dynamics is often described in terms of non-dimensional numbers involving the average bubble rise velocity, U_b: Reynolds number, Re (= $d_{eq}\rho U_b/\mu$), Weber number, We (=$\rho\ U_b^2 d_{eq}/\sigma$)and the drag coefficient C_D (= $4gd_{eq}/3U_b^2$). Each of these numbers, in combination with two other independent non-dimensional numbers, most commonly used being Eötvös number, Eo (=$d_{eq}^2 g/\sigma$) and the Morton number, Mo (=$g\mu^4/\rho\ \sigma^3$), are used in describing the bubble size-shape-velocity relationship for a variety of *pure* fluids [13, 14]. A classical empirical regime map describing the various regimes in bubble motion was given by Clift *et al.* [14], as shown in Figure 1.2a. Fluid properties play a strong role here. A higher surface tension, tends the bubble towards a spherical shape, even at larger bubble sizes. For bubbles in highly viscous liquids, bubbles can maintain a spherical shape at large bubbles sizes, then transition into a dimpled ellipsoid or a skirted shape. For a low viscosity situation, such as air-water systems, the bubble shapes transition from a spherical to an ellipsoidal, wobbly and ultimately a spherical cap, with an increase in bubble size. By considering the drag coefficient, the regimes of bubble behaviour can be broadly classified into three

regimes[15, 16], as shown in Figure 1.2b:

I Viscous-dominated regime (at low *Re*) - Bubbles are spherical in shape, rise velocity increases with increasing bubble diameter. Flow around the bubble is axisymmetric. C_D has a constant relationship with *Re* (C_D=16/*Re*).

II Surface-tension-dominated regime (at intermediate *Re*) - Bubbles deviate from spherical into ellipsoidal and wobbly shapes. Surface tension and inertial forces on the bubble determine the rise velocity. Strong oscillations in shape and bubble path are observed in this regime.

III Inertial regime (at high *Re*) - Bubbles are spherical-cap or skirted in shape and the bubble motion is dominated by inertial forces. Velocity increases with equivalent diameter in this regime and C_D reaches a constant.

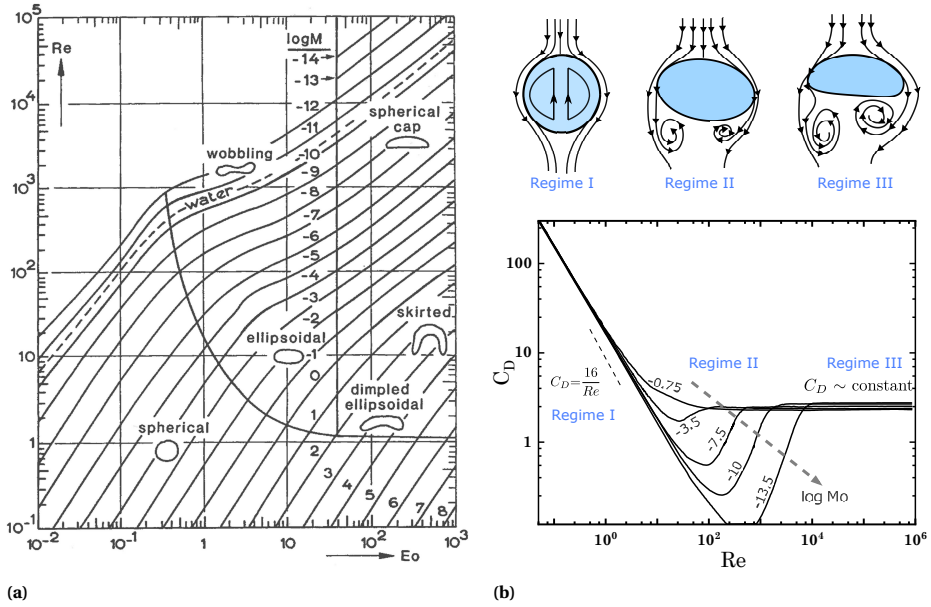

(a) (b)

Figure 1.2: (a) Clift-Grace-Weber map (adapted from [14]) showing the various regimes in bubble motion in *Re-Eo-Mo*. (b) Drag coefficient prediction for a variety of bubbles (adapted from [17]) with a schematic representation of bubble wakes.

Under practical conditions in industrial bubble columns, bubbles tend to be in the ellipsoidal and wobbly regimes [e.g. 11, 18]. The bubble regime depends on the type of liquid (e.g. water-type or organic content in the liquid), the nature of sparger and the operational conditions. Here, pressure and temperature play a role as well. A higher pressure leads to an increase in the gas density and smaller bubbles being generated from the spargers [18]. A higher temperature corresponds to a decrease in both viscosity and surface tension of the liquid, both leading a smaller bubble [9].

MESO- AND MACRO-SCALE

At *mesoscale*, complex bubble-bubble interactions make the rise behaviour of bubbles more intricate than that of a single bubble. On one hand, collective effect of bubbles in a swarm can accelerate or hinder the rise velocities of individual bubbles; on the other hand, bubble-bubble interactions, through coalescence and breakup, can change the bubble size distribution (BSD). The BSD depends both on how the bubbles are generated at the sparger and on bubble coalescence and breakup; it can have a strong influence on the bubble-bubble interaction, which, in turn, can strongly influence the BSD.

In practical models towards predicting the collective effects on the bubble rise velocity and drag coefficient, the single bubble behaviour is corrected by a gas fraction (α_g) dependent factor; α_g is determined by the rise velocity of the bubbles and the superficial gas velocity (v_{sg}, i.e., the flow rate of gas divided by the cross-sectional of the column). Amongst several proposed correlations in the literature [e.g. 19–23], there exists discrepancies, primarily arising from the BSD and the flow regime considered.

In a homogenous regime (at low α_g), the swarm rise is hindered due to the reduction of the buoyancy force on the bubble, leading to a lower slip velocity and a higher drag coefficient [e.g. 19, 20, 22]. In a heterogeneous regime (at higher α_g), bubbles clustering leads to their collective motion being faster than a single bubble; a lowering of drag coefficient is observed in this case. Clustering of bubbles is associated with a wider distribution of bubble sizes, where smaller bubbles are entrained in the wake of larger bubbles [19, 23].

Under practical conditions, *macro-scale* dynamics of larger bubble columns can only be described as semi- to fully-heterogeneous, characterized by bi-modal bubble size distribution. Identification of the regime transition, from a homogeneous to a chaotic regime, has been a subject of detailed investigation [24]. The ability to create a narrow BSD is strongly dependent on the nature of the sparger and the fluid properties. A uniform distributed fine-pore sparger can maintain a homogeneous regime up to a large gas fractions, as shown by Sharaf *et al.* [25] and Mudde *et al.* [26]. Under such conditions, identification of the flow regime and measurement of coarse macroscopic properties, such as initial bubble size and mean bubble size, are useful in *empirically* correlating the geometric (column sizing, sparger size) and the operational parameters (pressure, temperature, gas and liquid flow rates).

The mechanisms governing the bubble breakup and coalescence has been a topic of large body of literature [e.g. 27]. Turbulent fluctuations is the main reason for bubble breakup; classical models are based on a critical Weber number, We_{crit}, as a criterion, whereby sufficiently high turbulent kinetic energy overcomes the bubble surface energy. Coalescence mechanisms are governed by the frequency of collisions (dependent on bubble density/gas fraction) and the efficiency of collisions leading to a fruitful coalescence [28]. For practical bubble column designs, the coalescence & breakup models are incorporated into Population Balance Equations (PBEs), which are coupled with CFD simulations to obtain bubble size distribution. However, these models are dependent on uncertain assumptions and empirical investigations for homogeneous bubble motions. Translation of such models to large scale systems (with a large number of bubbles) is limited by computationally-efficient methods and reliable experimental dataset for validation [29].

EXPERIMENTAL & NUMERICAL TECHNIQUES

In a multiscale approach, a general procedure for understanding bubbly flows is (i) a reduction in complexity of multiple bubble interaction with detailed investigations at interfacial and (single) bubble level, and (ii) a development of mechanistic models/ correlations useful for characterizing dense bubbly flows. A few examples of studies, both numerical and experimental, at each scale are depicted in Figure 1.3.

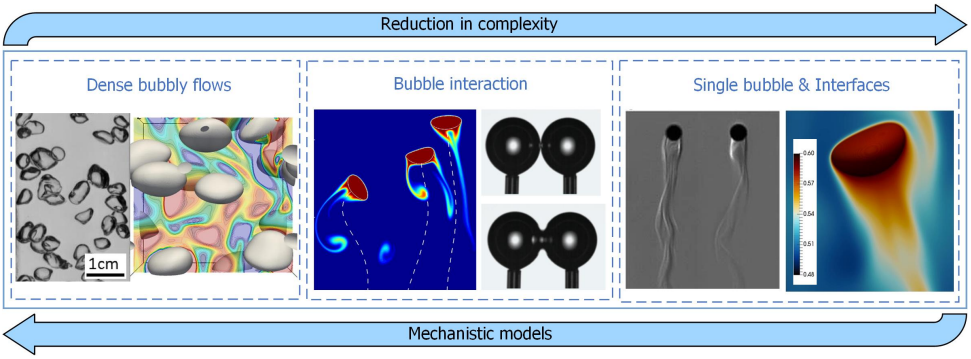

Figure 1.3: Multiscale studies in bubbly flows: from interfaces to dense swarms. Images reproduced experimental and numerical investigations [30–34].

An ideal measurement technique would provide a non-invasive, direct and instantaneous 3D measurement, encompassing the entire geometry and not limited by the complexity/opaqueness of the flow. In reality, however, such techniques seldom exist, leading to specific methods used at different scales. A pragmatic approach in deciphering the underlying multiphase mechanisms would be the utilization of a combination of measurements techniques in decoupling the scale-specific effects.

At interfacial level, specialized techniques, such as Particle image velocimetry (PIV) [35], Schlieren imaging [32] and Planar Laser induced Fluorescence (P-LIF) [36], enable decoupling the bubble motion and wake effects. Advances in high speed imaging and post-processing methods enable these techniques to be implemented for multiple bubbles in semi-dilute situations [37]. However, as the flow becomes dense and opaque, measurement of bubbles sizes, velocities or gas fractions are limited to either intrusive techniques (e.g. four-point probe [38], wire-mesh sensors [39]) or non-intrusive techniques with spatial and/or temporal limitations (e.g. X-ray imaging [40], electrical resistance tomography [41]).

Advances in CFD simulations, accompanied by an increase in computation power, are used to investigate bubbly flows from a single bubble to a dense case with a large number of bubbles [e.g. 42]. Rigorous Direct Numerical Simulation (DNS) techniques, such as front tracking methods and sub-grid scale modelling [e.g. 43], enables a better description of the micro-phenomena at the interface and forms the basis for developing correlations for a bubble swarm. However, similar to the experimental techniques, the challenge is in resolving different length scales for a multiphysics phenomena, such as the interplay between hydrodynamics and mass transfer.

1

THE MISSING LINKS

While several unanswered questions and challenges exist in complex bubbly flows, we would like to point out two such important missing links, which form a basis for addressing the topics and research questions described later:

- Liquid properties & purity effects - In reality, most practical implementations of bubbly flows do not operate with *pure* liquids and contain a multitude of additives (electrolytes, surfactants, organics, etc.) at different concentrations. However, a majority of the current models for scale-up are dependent on empirical investigations with air-water systems and a few cases of viscous liquids; while addressing a deviation from these models as a possible contaminant effect.

  Contaminant effects find their basis in classical studies done with tap-water, showing strong influence on the rise velocity (Clift *et al.* [14, Figure 7.3]) and the drag coefficient [44]. While, a multitude of studies are performed for a variety of liquids & additives, such investigations are performed at meso- or macro-scale [e.g. 24]; decoupling effects of additives on bubble generation, coalescence/breakup and swarm effects become highly specific to the system studied. While the nature and concentration of additives vary depending on the application, a generalized understanding of rheological effects at the gas-liquid interface would aid in classifying these fluids as pure (vis-à-vis their agreement with known correlations) or in developing specific models for their kinetics at the interface.

- Dynamic bubble behaviour and interfacial transport - For bubbles that deviate from a spherical into ellipsoidal and wobbly shapes, surface tension and inertial forces become dominant. In these bubble regimes, wake-induced effects play a strong role, reflected in their zig-zag/helical paths and strong oscillations in shape [45]. While, such effects are reflected in their averaged rise characteristics, i.e., the rise velocity and the drag coefficient (Figure 1.2), they strongly influence the local interfacial mass and heat transfer characteristics, as observed for the case of dissolving ellipsoidal bubbles [46]. A strong missing link here is an understanding of the interplay between the dynamic bubble behaviour and the mass transfer. Such wake-induced effect needs to be understood at microscale for a single bubble, before accounting for its influence, or lack thereof, in a bubble swarm.

1.2. MOTIVATION AND TOPICS

The current project is part of the NWO-Industrial Partnership Programme (NWO-IPP) *Dense Bubbly Flows*, with a motivation to provide a fundamental understanding of the mechanisms in bubbly flow inspired from industrial practice. We focus on two challenges from practical cases: CO_2 capture and electrolysis. The research questions are outlined in the further sections. An *inevitable* question arises here, regarding the applicability of academic experimental research to a real-industrial case, vis-à-vis the difference in scales. Design and improvement methodologies for these industrial processes are dependent on *heuristics* and simplified phenomenological models; here, we believe, a mechanistic approach, beyond the experimental data for validation, can aid in the development of pragmatic models.

1.2.1. ELECTROLYTES: COALESCENCE AND RISE DYNAMICS

In various electrochemcial processes, e.g. chlorate, chlor-alkali and CO_2, gas bubbles are produced at electrode surfaces [47]. Bubbles play a dichotomous role in these gas-evolving process [48]: (i) larger, millimeter sized, bubbles enhance convection, and thereby the mass transfer rates; (ii) smaller, micron-size, bubbles at the surface (Figure 1.4a) reduce the surface area available for electrode reactions and, thereby, increasing the overpotential and negatively influencing the reaction kinetics. Bubble nucleation, coalescence and detachment from the electrode surface play a strong role in the overall efficiency of the process. Bubble coalescence, by which the available surface area limitation can be subdued, is strongly inhibited by the high concentration of dissolved electrolytes usually involved in these electrochemical processes.

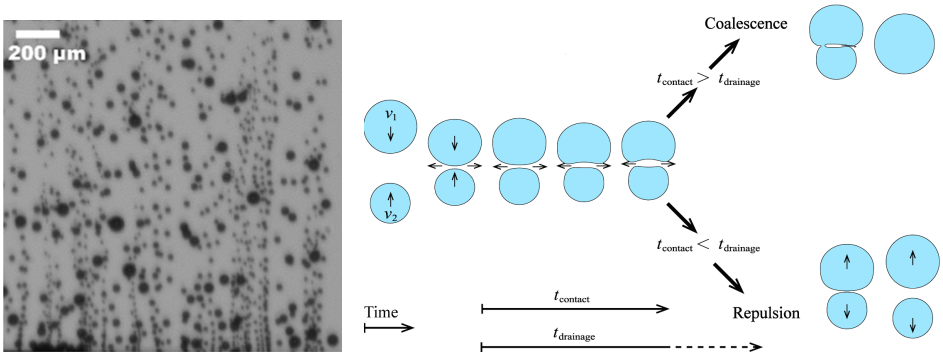

(a) (b)

Figure 1.4: (a) H_2 bubbles rising from an electrode surface [49], (b) Sketch showing the drainage and film rupture processes of bubble coalescence [28].

Inhibition of bubble coalescence due to electrolytic presence has been a topic of detailed investigations at an interfacial level. Generally agreed mechanism in the literature is a 'Gibbs-Marangoni' effect: presence of ions during the drainage and film rupture stages (as shown in Figure 1.4b), retard the coalescence process, leading to a repulsion between the bubbles [50]. For engineering purposes, the electrolyte effect is characterized in terms of a *transition concentration* C_{trans}: minimum electrolyte concentration beyond which the inhibition effect is observed. A majority of the current literature studies have focused on the coalescence efficiency in two-bubble systems (ratio of coalesced bubbles/number of contacted) as a function of bubble contact time, approach velocity and the specific nature of constituent ions of the electrolyte [33, 51]. However, the role of electrolytes in the overall bubble hydrodynamics, from single bubble to dense flow, remains largely unanswered. Based on the above, the following research questions have been formulated for this topic:

- *How does electrolyte induced bubble coalescence inhibition affect the local and global hydrodynamics in a dense recirculating flow?*

The key in answering this question is understanding the role of electrolytes in the bubble formation, at a sparger that can *mimic* microbubble generation at an electrode surface; producing large gas fractions of H_2 bubbles using electrodes would pose a safety risk.

We choose for an airlift type column, as this is adopted in industrial practice of chlorate electrolysis [52]. Such a design also provides the advantage of enhanced global mixing, while also intensifying bubble detachment from the sparger surface by the recirculating liquid flow. This question has been addressed in **Chapter 2** of the current thesis. The focus is to correlate the influence of the bubble size distribution at the sparger to the flow profile, local and global gas fractions obtained in the column.

- *How does electrolytes at high concentrations affect rise of single ellipsoidal bubble?*

All additives to air-water systems (surfactants, electrolytes, alcohols, organics, etc.) have been generally classified as contaminants, with respect to its influence on bubble rise characteristics [51]. Whereas surfactants, even at low concentrations ($\sim \mathcal{O}10^{-3}$ mol/liter), have been well-studied as a component affecting the interfacial characteristics and the bubble behaviour, the influence of smaller electrolyte ions on the bubble rise is not well-understood. In this context, we study the role of high electrolyte concentrations at high temperature (up to 80°C), conditions relevant to electrolysis process, on the motion of a single ellipsoidal bubble and compare it against available correlations. Knowledge of pure or impure liquid behaviour will enable to use the appropriate correlations for describing bubble rise characteristics. This question has been addressed in **Chapter 3** of the current thesis.

1.2.2. GAS-LIQUID MASS TRANSFER AND BUBBLE MOTION

Understanding the underlying mechanisms for gas-liquid mass transfer has been a subject of extensive research in past decades, only accelerated by the new-age reactor design requirements for applications such as: CO_2 capture and CO_2 electrolysis. The mechanisms of gas-liquid mass transfer are controlled by an interplay between the molecular diffusion and convective transport [53], as schematized in Figure 1.5. In a thin film around the interface, within the mass transfer boundary layer, the transport is controlled by molecular diffusion. Beyond this thin film, convective flow over the bubble governs the transport of species and mixing in the bulk liquid.

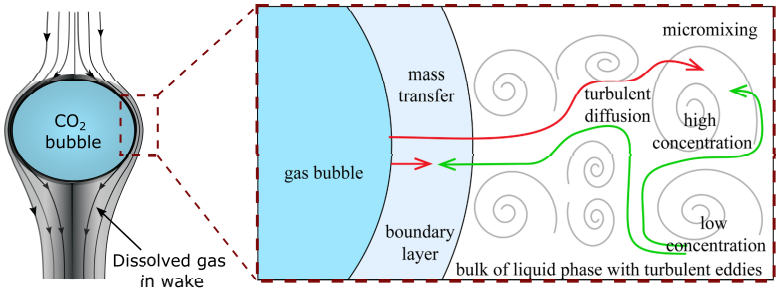

Figure 1.5: Schematic of mass transfer from a single bubble (adapted from [54])

While there exists an added complexity in describing the mass transfer and mixing in a dense flow, such endeavours often rely on a good comprehension of single bubble behaviour. The classical mass transfer models describing the correlation between flow and mass transfer, Higbie's penetration theory and Frossling's particle theory, are based on

assumptions of potential and Stokes's flow, respectively, around a spherical bubble [55]; the theoretical assumptions of these models do not reflect the reality of a rising bubble in experimental studies [56]. This is specially the case for bubbles in ellipsoidal and wobbly regime, most found in practical bubble columns. Despite this, most mass transfer correlations used in practical designs are empirical and semi-empirical extensions of the classical models.

On the other hand, bubbles in ellipsoidal and wobbly regime have wake-induced effects, such as: shape and path oscillations (as described earlier); these effects are not considered in the mass transfer correlations. While the concepts of path and shape oscillations are well-studied, both numerically and experimentally, in describing the dynamic behaviour of a bubble, their implications on gas-liquid mass transfer have been poorly understood [54]. An analogical understanding of the interplay between the two mechanisms, hydrodynamics and mass transfer, is therefore required in describing the underlying mechanisms in the rise of shrinking bubbles. The following research questions have been formulated for this topic and are addressed in **Chapter 4** of the thesis:

- *How does bubble shrinkage influence the rise characteristics of a single bubble?*

Dissolving CO_2 bubbles, during their lifetime in a bubble column, exhibit different rise behaviour (bubble shape, rise velocity); this is accompanied by a change in bubble regime (Figure 1.2), as an initial large ellipsoidal/wobbly bubble tends towards a spherical shape. Difference in mass transfer characteristics for different regimes have been attributed to possible contaminant effects, with studies done in tap water [57]. While surfactant presence does influence the interfacial mobility and, thereby, the dynamic rise behaviour, such effects needs to be separated from a pure-water case. In this context, we study the rise characteristics of shrinking (CO_2) and non-shrinking (N_2) bubbles in demineralized water.

- *What is the role of bubble shape and path oscillations in the interplay between hydrodynamics and mass transfer?*

A generalized mass transfer correlation should include the specific dynamic bubble behaviours in different regimes. For the practical cases of ellipsoidal & wobbly bubbles, where, wake effects are strongly observed, we study the influence of path and shape oscillations on the interplay between hydrodynamics and mass transfer. Further, drawing an analogy between the two mechanisms can aid in developing pragmatic correlations towards predicting mass transfer characteristics based on the knowledge of bubble hydrodynamic parameters, such as drag coefficient.

1.3. OUTLINE OF THE THESIS

In this thesis we address the two aforementioned topics, electrolytes and CO_2 mass transfer, and their influence on bubbly flows. Chapters 2, 3 and 4 are self-contained articles that have been published/in-preparation in scientific journals. A brief literature overview and details of experimental techniques used are explained in each chapter. Notations and abbreviations used are specific for each context and are included at the beginning of each chapter.

Chapter 2 presents a study on electrolytic addition in dense homogeneous recirculating flow. In a consequent opaque flow, non-intrusive measurements techniques, high-

speed imaging, bubble imaging velocimetry (BIV) and X-ray imaging, are used to measure bubble size distribution, bubble velocity and gas fraction profiles, respectively. The role of the electrolyte in coalescence inhibition at the sparger and further hydrodynamics of the airlift column is compared with a 1D drift flux model.

Chapter 3 reports on the role of liquid temperature (up to 80°C), and the presence of simple and mixed electrolytes on the rise dynamics of an ellipsoidal H_2 bubble. Based on the change in measured liquid properties (viscosity, density and surface tension), the obtained results are compared to non-dimensional correlations, for rise velocity and deformation in pure liquids, available in the literature. Furthermore, we show that a simplified correlation of the drag coefficient fits all experimental data.

Chapter 4 presents a study on rising CO_2 and N_2 bubbles. For these bubbles, their size, trajectory, and rise velocity have been measured using a moving camera system, while the dissolved CO_2 is studied using a Planar Laser-induced fluorescence (P-LIF) technique. We explore the interplay between hydrodynamics and mass transfer using well-studied regimes in bubble behaviour. Our results show that the interrelation between mass transfer and bubble rise dynamics is quasi-steady in nature and strongly dependent on wake-induced effects: shape and path oscillations.

Chapter 5 presents the overall conclusions of the work, discusses the broader applicability of the findings and gives an outlook of future possibilities in this field. Here, a further investigation of dilute bubbly flow case with electrolyte and gas-liquid mass transfer with CO_2 bubbles has also been addressed.

REFERENCES

[1] P.-C. Chen, C.-H. Huang, T. Su, H.-W. Chen, M.-W. Yang, and J.-M. Tsao, *Optimum conditions for the capture of carbon dioxide with a bubble-column scrubber,* International Journal of Greenhouse Gas Control **35**, 47 (2015).

[2] Y. Kawase and M. Moo-Young, *Hydrodynamics in bubble column bioreactors with fermentation broths having a yield stress,* Applied microbiology and biotechnology **30**, 596 (1989).

[3] L. V. Teixeira, L. F. Moutinho, and A. S. Romão-Dumaresq, *Gas fermentation of c1 feedstocks: commercialization status and future prospects,* Biofuels, Bioproducts and Biorefining **12**, 1103 (2018).

[4] A. Talebi, S. Salehi Neyshabouri, and H. Khoshgou, *Investigation on factors affecting the performance of the air bubble curtain in preventing the penetration of salinity,* International Journal of Environmental Science and Technology **19**, 10599 (2022).

[5] R. Santana, J. Ribeiro, M. Santos, A. Reis, C. Ataíde, and M. A. Barrozo, *Flotation of fine apatitic ore using microbubbles,* Separation and Purification Technology **98**, 402 (2012).

[6] V. N. Lima, C. S. Rodrigues, E. F. Sampaio, and L. M. Madeira, *Insights into real industrial wastewater treatment by fenton's oxidation in gas bubbling reactors,* Journal of Environmental Management **265**, 110501 (2020).

[7] N. Deen, R. Mudde, J. Kuipers, P. Zehner, and M. Kraume, *Bubble columns, Ullmann's Encyclopedia of Industrial Chemistry*, Ullmann's Encyclopedia of Industrial Chemistry (2010).

[8] W.-D. Deckwer and R. W. Field, *Bubble column reactors*, 3rd ed., Vol. 200 (Wiley New York, 1992).

[9] P. Rollbusch, M. Bothe, M. Becker, M. Ludwig, M. Grünewald, M. Schlüter, and R. Franke, *Bubble columns operated under industrially relevant conditions – current understanding of design parameters,* Chemical Engineering Science **126**, 660 (2015).

[10] Y. T. Shah, B. G. Kelkar, S. P. Godbole, and W.-D. Deckwer, *Design parameters estimations for bubble column reactors,* AIChE Journal **28**, 353 (1982).

[11] M. Bothe, M.-A. Christlieb, M. Hoffmann, O. Tedjasukmana, F. Michaux, P. Rollbusch, M. Becker, and M. Schlüter, *Bubble size and bubble velocity distribution in bubble columns under industrial conditions,* The Canadian Journal of Chemical Engineering **95**, 902 (2017).

[12] H. A. Jakobsen, *Chemical reactor modeling: Multiphase Reactive Flows*, 2nd ed., edited by H. A. Jakobsen (Springer, 2014).

[13] L. Amaya-Bower and T. Lee, *Single bubble rising dynamics for moderate reynolds number using lattice boltzmann method,* Computers & Fluids **39**, 1191 (2010).

[14] R. Clift, J. Grace, and M. Weber, *Bubbles, Drops and Particles* (New York: Academic Press, 1978).

[15] A. Tomiyama, I. Kataoka, I. Zun, and T. Sakaguchi, *Drag coefficients of single bubbles under normal and micro gravity conditions,* JSME International Journal Series B Fluids and Thermal Engineering **41**, 472 (1998).

[16] A. A. Kulkarni and J. B. Joshi, *Bubble formation and bubble rise velocity in gas- liquid systems: a review,* Industrial & Engineering Chemistry Research **44**, 5873 (2005).

[17] D. Rodrigue, *A general and correlation for the rise and velocity and of single and gas bubbles,* The Canadian Journal of Chemical Engineering **82** (2004), 10.1002/cjce.5450820219.

[18] P. M. Wilkinson and L. L. v. Dierendonck, *Pressure and gas density effects on bubble break-up and gas hold-up in bubble columns,* Chemical Engineering Science **45**, 2309 (1990).

[19] M. Simonnet, C. Gentric, E. Olmos, and N. Midoux, *Experimental determination of the drag coefficient in a swarm of bubbles,* Chemical Engineering Science **62**, 858 (2007).

[20] D. D. McClure, J. M. Kavanagh, D. F. Fletcher, and G. W. Barton, *Experimental investigation into the drag volume fraction correction term for gas-liquid bubbly flows,* Chemical Engineering Science **170**, 91 (2017).

[21] I. Roghair, M. Van Sint Annaland, and H. J. Kuipers, *Drag force and clustering in bubble swarms,* AIChE Journal **59**, 1791 (2013).

[22] D. Colombet, D. Legendre, F. Risso, A. Cockx, and P. Guiraud, *Dynamics and mass transfer of rising bubbles in a homogenous swarm at large gas volume fraction,* Journal of Fluid Mechanics **763**, 254 (2015).

[23] C. Muilwijk and H. E. Van den Akker, *The effect of liquid co-flow on gas fractions, bubble velocities and chord lengths in bubbly flows. part i: Uniform gas sparging and liquid co-flow,* International Journal of Multiphase Flow **137**, 103498 (2021).

[24] G. Besagni and F. Inzoli, *The effect of liquid phase properties on bubble column fluid dynamics: Gas holdup, flow regime transition, bubble size distributions and shapes, interfacial areas and foaming phenomena,* Chemical Engineering Science **170**, 270 (2017).

[25] S. Sharaf, M. Zednikova, M. C. Ruzicka, and B. J. Azzopardi, *Global and local hydrodynamics of bubble columns effect of gas distributor,* Chemical Engineering Journal **288**, 489 (2016).

[26] R. Mudde, W. Harteveld, and H. Van den Akker, *Uniform flow in bubble columns,* Industrial & Engineering Chemistry Research **48**, 148 (2009).

[27] Y. Liao and D. Lucas, *A literature review of theoretical models for drop and bubble breakup in turbulent dispersions,* Chemical Engineering Science **64**, 3389 (2009).

[28] J. Kamp and M. Kraume, *From single drop coalescence to droplet swarms scale-up considering the influence of collision velocity and drop size on coalescence probability,* Chemical Engineering Science **156**, 162 (2016).

[29] L. Gemello, C. Plais, F. Augier, and D. L. Marchisio, *Population balance modelling of bubble columns under the heterogeneous flow regime,* Chemical Engineering Journal **372**, 590 (2019).

[30] Y. Jin and M. Schlüter, *Direct numerical simulation of the interfacial mass transfer of a bubble in self-induced turbulent flows,* International Journal of Heat and Mass Transfer **135**, 1248 (2019).

[31] B. Aboulhasanzadeh, S. Thomas, M. Taeibi-Rahni, and G. Tryggvason, *Multiscale computations of mass transfer from buoyant bubbles,* Chemical Engineering Science **75**, 456 (2012).

[32] C. Veldhuis, A. Biesheuvel, L. van Wijngaarden, and D. Lohse, *Motion and wake structure of spherical particles,* Nonlinearity **18**, C1 (2004).

[33] S. Orvalho, P. Stanovsky, and M. C. Ruzicka, *Bubble coalescence in electrolytes: effect of bubble approach velocity,* Chemical Engineering Journal **406**, 125926 (2021).

[34] N. Balcázar-Arciniega, O. Antepara, J. Rigola, and A. Oliva, *A level-set model for mass transfer in bubbly flows,* International Journal of Heat and Mass Transfer **138**, 335 (2019).

[35] A. Dueñas, I. Wieland, W. Marcum, and Q. Wu, *Form drag coefficient quantification on rising bubbles using particle image velocimetry,* Flow Measurement and Instrumentation **80**, 101988 (2021).

[36] J. Francois, N. Dietrich, P. Guiraud, and A. Cockx, *Direct measurement of mass transfer around a single bubble by micro-plifi,* Chemical Engineering Science **66**, 3328 (2011), 10th International Conference on GasLiquid and GasLiquidSolid Reactor Engineering.

[37] P. Kováts, D. Thévenin, and K. Zähringer, *Influence of viscosity and surface tension on bubble dynamics and mass transfer in a model bubble column,* International Journal of Multiphase Flow **123**, 103174 (2020).

[38] J. Xue, M. Al-Dahhan, M. P. Dudukovic, and R. F. Mudde, *Bubble dynamics measurements using four-point optical probe,* The Canadian Journal of Chemical Engineering **81**, 375 (2003).

[39] R. Kipping, H. Kryk, E. Schleicher, M. Gustke, and U. Hampel, *Application of a wire-mesh sensor for the study of chemical species conversion in a bubble column,* Chemical Engineering & Technology **40**, 1425 (2017).

[40] M. M. Mandalahalli, E. C. Wagner, L. M. Portela, and R. F. Mudde, *Electrolyte effects on recirculating dense bubbly flow: An experimental study using x-ray imaging,* AIChE Journal **66**, e16696 (2020).

[41] B. K. Singh, A. Quiyoom, and V. V. Buwa, *Dynamics of gas–liquid flow in a cylindrical bubble column: Comparison of electrical resistance tomography and voidage probe measurements,* Chemical Engineering Science **158**, 124 (2017).

[42] M. A. Taborda, P. Kováts, K. Zähringer, and M. Sommerfeld, *The influence of liquid properties on flow structure, bubble dynamics and mass transfer in a laboratory bubble column: Experimental analysis versus numerical modelling and computation,* Chemical Engineering Research and Design **185**, 51 (2022).

[43] C. M. Y. Claassen, S. Islam, E. A. J. F. F. Peters, N. G. Deen, J. A. M. H. Kuipers, and M. W. Baltussen, *An improved subgrid scale model for front-tracking based simulations of mass transfer from bubbles,* AIChE Journal **66**, e16889 (2020).

[44] A. Tomiyama, G. Celata, S. Hosokawa, and S. Yoshida, *Terminal velocity of single bubbles in surface tension force dominant regime,* International Journal of Multiphase Flow **28**, 1497 (2002).

[45] J. Magnaudet and G. Mougin, *Wake instability of a fixed spheroidal bubble,* Journal of Fluid Mechanics **572**, 311337 (2007).

[46] J. Huang and T. Saito, *Influences of gas–liquid interface contamination on bubble motions, bubble wakes, and instantaneous mass transfer,* Chemical Engineering Science **157**, 182 (2017).

[47] A. Angulo, P. van der Linde, H. Gardeniers, M. Modestino, and D. Fernández Rivas, *Influence of bubbles on the energy conversion efficiency of electrochemical reactors,* Joule **4**, 555 (2020).

[48] J. K. Lee and A. Bazylak, *Bubbles: The good, the bad, and the ugly,* Joule **5**, 19 (2021).

[49] P. Chandran, S. Bakshi, and D. Chatterjee, *Study on the characteristics of hydrogen bubble formation and its transport during electrolysis of water,* Chemical Engineering Science **138**, 99 (2015).

[50] M. Firouzi, T. Howes, and A. V. Nguyen, *A quantitative review of the transition salt concentration for inhibiting bubble coalescence,* Advances in Colloid and Interface Science **222**, 305 (2015), reinhard Miller, Honorary Issue.

[51] S. Orvalho, M. C. Ruzicka, and J. Drahos, *Bubble column with electrolytes: Gas holdup and flow regimes,* Industrial & Engineering Chemistry Research **48**, 8237 (2009).

[52] A. Cornell, *Chlorate cathodes and electrode design,* in *Encyclopedia of Applied Electrochemistry*, edited by G. Kreysa, K.-i. Ota, and R. F. Savinell (Springer New York, New York, NY, 2014) pp. 175–181.

[53] D. Turney and S. Banerjee, *Transport phenomena at interfaces between turbulent fluids,* AIChE Journal **54**, 344 (2008).

[54] S. lin Yan, X. qing Wang, L. tao Zhu, X. bao Zhang, and Z. hong Luo, *Mechanisms and modeling of bubble dynamic behaviors and mass transfer under gravity: A review,* Chemical Engineering Science **277**, 118854 (2023).

[55] M. Baltussen, *How fundamental knowledge on mass transfer in bubbly flows will help process intensification,* Chemical Engineering and Processing - Process Intensification **187**, 109344 (2023).

[56] J. Solsvik, *Lagrangian modeling of mass transfer from a single bubble rising in stagnant liquid,* Chemical Engineering Science **190**, 370 (2018).

[57] W. Nock, S. Heaven, and C. Banks, *Mass transfer and gas–liquid interface properties of single CO_2 bubbles rising in tap water,* Chemical Engineering Science **140**, 171 (2016).

2

ELECTROLYTE EFFECTS IN RECIRCULATING DENSE BUBBLY FLOWS

"In regione caecorum rex est luscus."
(In the country of the blind the one-eyed man is king)

~ Desiderius Erasmus Roterodamus, *Adagia* (1500)

In this chapter, the effect of an electrolyte (up to 2M of NaCl dissolved in water) on a homogeneous dense bubbly flow, in an airlift bubble column, is studied using non-intrusive techniques. X-ray and high-speed imaging are used to investigate the bubble size distribution, the local and the global gas-fraction profiles. The major effect of the electrolyte is the bubble size distribution at the fine-pore sparger, which is a consequence of the bubble coalescence inhibition promoted by the electrolyte. The bubble plume widening, the increase in overall gas-fraction, and the onset of bubble recirculation in the column, can all be explained by the bubble size reduction at the fine-pore spargers. As a result of the bubble size reduction, the overall role of the electrolyte is in a reduction of the driving force for the liquid recirculation. Furthermore, an accumulation of the small bubbles causes a layer of foam at the free surface, which is dynamic in nature and induces additional bubble recirculation.

This chapter has been published as M.M. Mandalahalli, E.C. Wagner, L.M. Portela, and R.F. Mudde, *Electrolyte effects on recirculating dense bubbly flow: An experimental study using x-ray imaging*, AIChE Journal, **66**, e16696 (2020) [1]. Experimental data set is available on the 4TU Research data platform [2].

NOMENCLATURE

Greek symbols

$\alpha_{\text{g,pixel}}$	pixel-wise gas fraction on X-ray detector [-]
μ_0	X-ray attenuation coefficient [-]
α_{R}	Riser section gas fraction [-]
α_{D}	Downcomer section gas fraction [-]

Other symbols and abbreviations

v_{sg}	Gas superficial velocity [m/s]
C_{trans}	Transition salt concentration [mol/liter]
C_s	Salt concentration [mol/liter]
$d_{b,avg}$	Average bubble size [mm]
I_{pixel}	Pixel-wise intensity on X-ray detector [-]
I_0	X-ray Pixel-wise intensity without material [-]
X	Material depth between source & detector [mm]
U_b	Bubble rise velocity [m/s]
v_c	liquid circulation velocity [m/s]
$\text{H}_{\text{L,i}}$	Initial liquid height [mm]
W_{plume}	Width of bubble plume [mm]
W_s	Width of sparger = 25 [mm]

Subscripts

I_{gas}	X-ray intensity attenuated with presence of gas
$I_{\text{no,gas}}$	X-ray intensity of column filled only with liquid
$R,salt$, $R,nosalt$	riser section with & without salt
$D,salt$, $D,nosalt$	downcomer section with & without salt

2.1. INTRODUCTION

ELectrolytes can be found in many industrial gas-liquid unit-operations, such as: electrolysers, wastewater treatment and froth flotations [e.g. 3, 4]. In pneumatically agitated equipment, such as bubble columns, the bubble dynamics determines the mixing, heat and mass transfer between the phases. Airlift or gaslift columns are a variant of the bubble columns, where the mixing also depends on the global circulation of the liquid; they have lower shear-rates, shorter mixing-times and a larger operating-flow window, when compared to bubble columns; hence, they are widely used in chemical and bio-processes applications [5].

The presence of surface active agents (such as: electrolytes, dissolved organics and surfactants in the liquid) can alter the performance of these processes. The complex hydrodynamics, combined with mass and heat transport, makes the design of airlift bubble columns still heavily reliant on phenomenological models. The majority of bubbly flow research has focused on ideal air-water systems and a better understanding of the effects of the surface active agents is needed, in order to develop efficient design models; in particular, for the airlift columns.

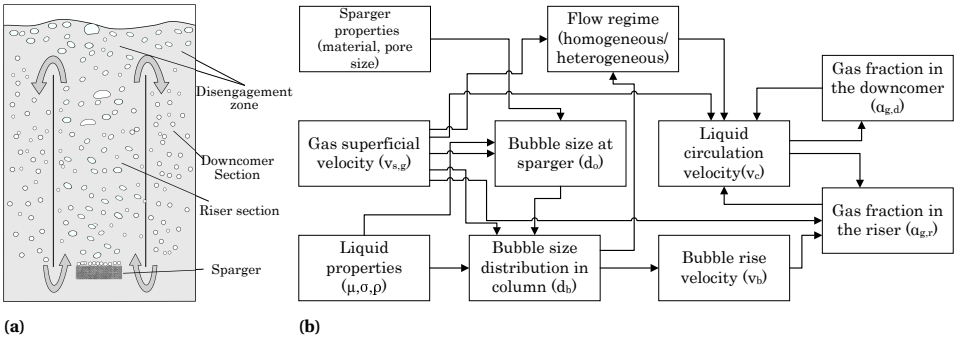

Figure 2.1: (a) Schematic of an internal airlift column (b) Relationship diagram of variables in hydrodynamic design of an airlift column (inspired from [6]).

Several designs are used in airlift columns. The simplest design uses a configuration with an internal circulation, in which two sections, the riser and the downcomer, are divided by a draft tube or a separator plate (Figure 2.1a). The inter-relations between various flow and setup parameters (Figure 2.1b) determine the hydrodynamics of the bubbly flow [6]. The bubble size distribution and the gas fraction are parameters that determine the bubble residence time distribution and interfacial area, relevant for heat and mass transfer operations. The bubble size distribution and heterogeneity of the flow are dependent on the selection of the sparger (type, material, pore sizes), physical properties of the liquid and the gas superficial velocity, v_{sg} [7]. Mudde *et al.* [8] showed that an homogeneous bubbly flow can be achieved up to 55% gas fraction with an arrangement of fine needle spargers. In particular, for airlift columns, the gas fraction profile in the riser section determines the carryover of gas into the downcomer section [9].

The role of electrolytes or inorganic salts can occur through three effects: (i) changes in the bulk liquid properties and a reported reduction in bubble rise velocity [10], (ii) a reduction in the bubble size at the sparger, and (iii) impact on bubble-bubble interac-

tions in the column and, thereby, on the bubble size distribution. Acting as "negative surfactants", the ions usually are repelled from the gas-liquid interface, inhibiting coalescence between bubbles [11]. The mechanism for coalescence inhibition can loosely be explained based on Marangoni effects due to a slight increase in surface tension, and the ion distribution at the interface [12]. For engineering purposes, the electrolyte effect is characterized by a transition salt concentration, C_{trans}, defined as the concentration beyond which the coalescence inhibition effect is observed between two bubbles [13]. For the salt considered in current study, sodium chloride (NaCl), the C_{trans} is found to be between 0.17 - 0.25M (moles/liter) [14]. The bubble size reduction at the sparger, in presence of salt, is dependent on the pore density of the sparger, the salt concentration and the gas superficial velocity. Reduced bubble sizes and thus increased residence time, leads to an overall increase in the gas fraction [15]. Besides v_{sg}, bubble interactions in the column are dependent also on the local gas fraction. Besagni and Inzoli [16] observed formation of rapid moving non-coalescing "bubble clusters", even at low salt concentrations (0.17M NaCl), which reduces the overall gas-phase residence time and the overall gas holdup. A better understanding of the electrolyte effect on bubble size and thereby on the gas fraction is therefore of interest in understanding the hydrodynamics of bubble columns and airlift columns.

The measurement of a polydispersed dense flow for spatial distribution of bubble sizes and gas fraction is a challenge. Non-invasive high-speed imaging and further image processing can provide a detailed picture of the bubble size distribution, bubble velocities and local gas-fraction [17]. However, at large gas-fractions in a wide column, the acquisition is limited to near-wall regions, making the extrapolation to the entire column, unreliable. Optical probes can provide single point measurements for bubbles substantially bigger than the tip size; however, the use of multiple probes can potentially disrupt the flow [18]. Since optical probes can only detect bubbles larger than the tip size, with a large fraction of small bubbles at high salt concentrations, this would lead to a bias towards a smaller fraction of bigger bubbles determining the local gas fraction. Radiation based techniques such as X-ray imaging have been widely used to characterize dense multiphase flows: fluidized bed [19], slurry bubble columns [20] and granular flows [21]. The X-ray imaging technique usually has a good spatial resolution, however, at a laboratory-scale is limited by time-averaging [22]. This limitation can be overcome by using high-speed X-ray radiography. However, high-speed X-ray radiography usually requires specialized equipment and large synchrotron X-ray source [23].

The aim of this work is to get a better understanding of the effect of dissolved salt, over a large concentration range (0-2M NaCl), on a homogeneous bubbly flow, in an airlift column. The role of salt, in the bubble plume behaviour and the gas-carryover in to downcomer section, is understood through its impact on the bubble size distribution at fine-pore bubble spargers. The use of high-speed imaging and X-ray imaging techniques, for measurement of the bubble size distribution, the time-averaged local and global gas fractions, are explained in-detail in the next section. To further explain the airlift column hydrodynamics, in electrolyte solutions, as a consequence of the bubble size reduction, a comparison of the experimental results of is made with a simple 1D drift-flux liquid recirculation model, based on the measured average bubble size at the fine-pore sparger.

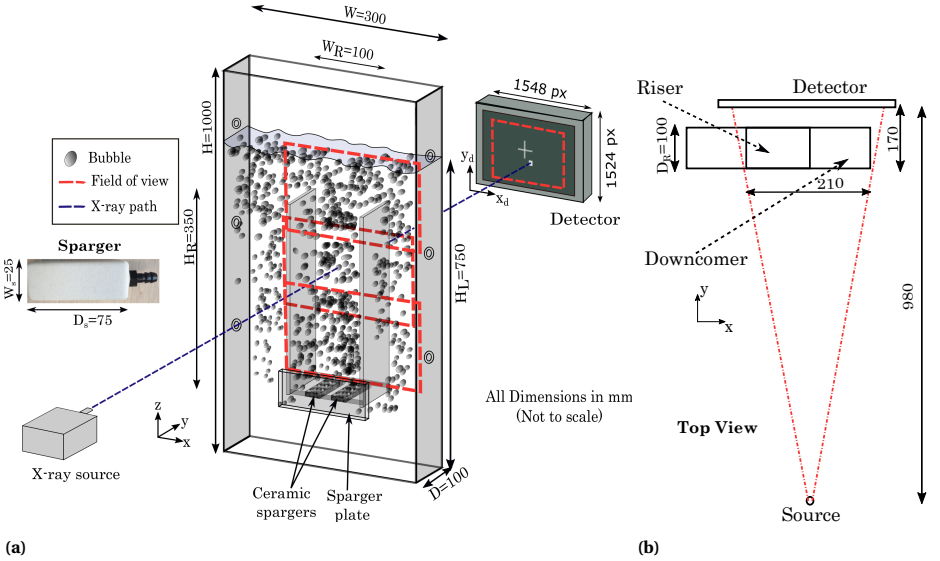

Figure 2.2: Airlift column setup: (a) schematic with column and sparger dimensions, rectangles showing the overlapping X-ray fields of view ; (b) top view showing the location of the column w.r.t. the X-ray source-detector. All dimensions are in millimetres (not to scale)

2.2. EXPERIMENTAL METHODOLOGY

2.2.1. EXPERIMENTAL SETUP AND X-RAY IMAGING

Experiments are performed in an internal loop airlift bubble column (WxDxH = 300 mm x 100 mm x 1000 mm), with riser section dimensions equal to W_RxD_Rx H_R = 100 mm x 100 mm x 400 mm. In order to avoid additional X-ray attenuation and salt induced corrosion, metal components are not used; the setup is built using perspex, with fittings made of PFA polymer. The column, as shown in Figure 2.2, is equipped with two ceramic fine-pore bubble spargers (Pentaires), with an average pore size of 50 μm and dimensions, W_sxD_sx H_s = 25 mm x 75 mm x 25 mm; placed at the bottom of the riser section (200 mm above the bottom of the column). The spargers are attached to the front end of the column using a sparger plate, that extends 50 mm into the riser section. The bottom surface of the spargers are sealed with glue, to avoid accumulation of gas bubbles. The degassed liquid height is maintained at H_L=750 mm (150 mm above the riser section). De-mineralized water and nitrogen gas are used as the liquid and gas phases, respectively. Purified sodium chloride (laboratory grade NaCl) is used as salt, at concentrations: 0.2M, 0.5M, 1M and 2M. The gas flow rate is controlled by a thermal mass flow controller (Bronkhorst B.V.). Change in fluid properties (density, viscosity and surface tension), due to electrolyte addition, are shown in Table 2.1. The superficial gas velocity, v_{sg}, defined as the ratio of the inlet gas flow rate to the riser cross-sectional area, is varied in the range of 0.8 cm/s to 4.8 cm/s.

A source-detector pair is used to measure the attenuation of the X-ray through various sections of the airlift column. In order to include both the riser and downcomer sections in the field of view, the column is placed close to the detector, as shown in the top view, Figure 2.2b. The X-ray measurements are performed in three overlapping field-

of-views, above the sparger plate (shown in rectangles in Figure 2.2a). The source is operated at 120 KeV and 1.6 mA, in order to achieve maximum contrast between the water and gas phases. The spot size of the X-ray source is 1mm. The flat detector (Xineous-3131 CMOS model), consists of a 307 mm x 302 mm sensitive area, with a 1548 x 1524 pixel array. Each pixel has a size of 198 μm x 198 μm, with 14 bits of pixel depth, with maximum intensity counts equal to 16000. The image acquisition frequency is 20Hz.

The measurement principle of X-ray imaging is based on the Beer-Lambert law. The intensity of each pixel on the detector, I_{pixel}, is a function of the thickness, X, and the attenuation coefficient, μ_0, of the material placed between the source and the pixel. The intensity attenuation is given by:

$$\frac{I_{\text{pixel}}}{I_0} = \exp(-\mu_0(E)X) \tag{2.1}$$

μ_0 is dependent on the energy distribution of the X-ray source. I_0 is the intensity on the pixel without the presence of the material between the source and the detector. The polychromatic nature of the X-ray source leads to preferential absorption of low-energy radiation, known as *beam hardening* [e.g. 24]. The close packing of detector pixels compared to the distance between source and detector can cause scattering effects. In current work, for practical purposes, the non-linear aspects of attenuation (beam hardening and scattering) are lumped into a constant, C, leading to a two parameter version of the Beer-Lambert equation:

$$log(I_{\text{pixel}}) = -\mu X + C \tag{2.2}$$

where, $\mu = \mu_0 I_0$. Considering the density difference between the gas and liquid phases, absorption of the X-ray is associated with the pathlength of water phase between the source and each pixel of the detector. Thus, the pixel-wise gas fraction, averaged along the X-ray path, can be obtained by measuring the intensities with and without the gas bubbles, I_{gas} and $I_{\text{no,gas}}$, respectively,

$$\alpha_{\text{g,pixel}} = \left(\frac{X_{\text{no,gas}} - X_{\text{gas}}}{X_{\text{nogas}}}\right) = \frac{1}{(\mu \cdot X_{\text{nogas}})} \cdot \log\left(\frac{I_{\text{gas}}}{I_{\text{no,gas}}}\right) \tag{2.3}$$

2.2.2. CALIBRATION AND VALIDATION

Besides the 2D coordinate (x_d, y_d) on the detector and the pathlength through water, the no-gas pixel-wise intensity (I_{nogas}) is also dependent on the dissolved electrolytes. Both sodium and chloride ions have valence electrons, leading to a higher attenuation of the radiation than in pure water. The difference between the attenuation in water with dissolved salt and the pure water is proportional to the salt concentration, C_s.

The X-ray coefficients (μ and C) for each pixel on the detector are obtained using a 4-point calibration method. Four rectangular columns with depths: 60 mm, 90 mm, 120 mm and 150 mm, filled with water, are used to record I_{pixel}. The resultant 2D intensity resembles a cone-beam profile, which is a characteristic of the diverging X-rays from the source. A line intensity profile on the dectector, therefore, is parabolic in nature (Figure 2.4b). The cone-beam profile is fitted by a second order polynomial in each direction of the detector, as shown in Figure 2.3a. This curve is obtained for different salt concentrations and column depths. Pixel-wise data is further fitted to the simplified Beer-Lambert

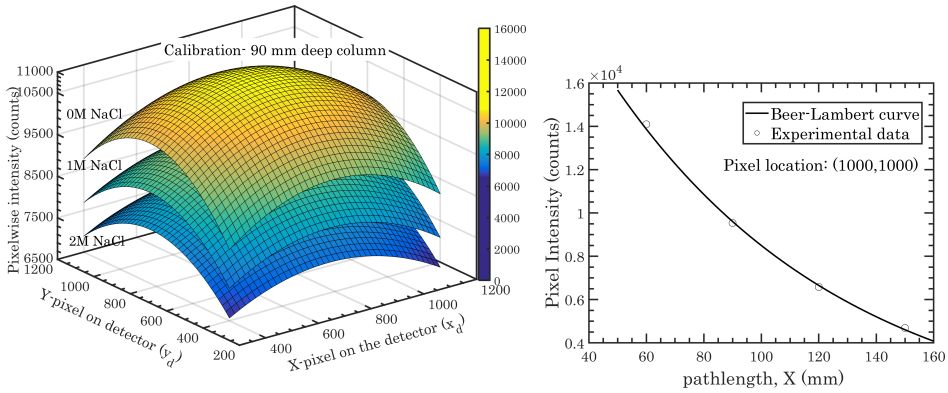

(a) **(b)**

Figure 2.3: Pixel-wise calibration of intensity: (a) cone-beam calibration profile for 90 mm deep column for different salt concentrations; (b) comparison of interpolated Beer-Lambert curve with experimental data on a random pixel (x,y) = (1000,1000) on the detector.

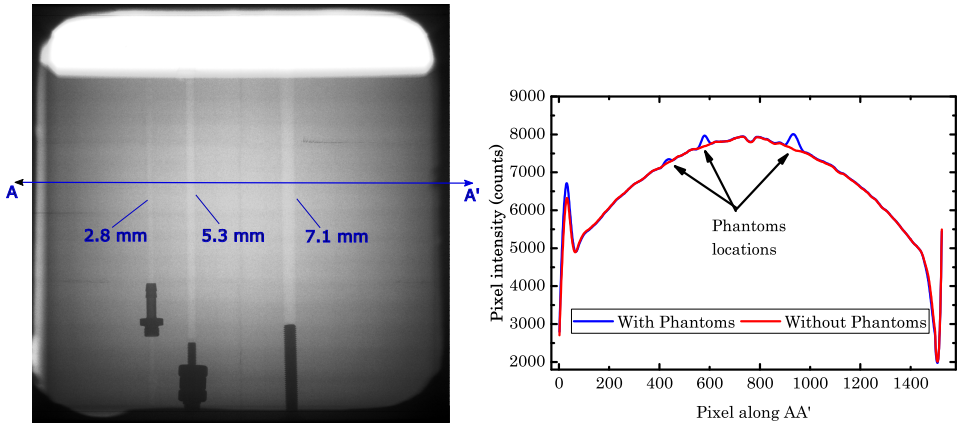

(a) **(b)**

Figure 2.4: Phantom validation of gas-fraction calibration: (a) Contrast image on the detector; (b) Horizontal line intensity profile along line AA' with and without phantom.

equation (Eqn. 2.2). The resultant curve generated is in good agreement with the raw experimental data, as seen for a random pixel in Figure 2.3b.

The reliability of the 4-point calibration method to compute the steady state gas fraction is tested using a phantom method. Three straws, made of polystyrene with internal diameters of 2.8 mm, 5.3 mm and 7.1 mm are placed in the 120mm deep column, corresponding to 2.3%, 4.4% and 5.9% void fraction, respectively. Absorption due to the wall material of the phantoms is ignored due as the attenuation coefficient of polystyrene at 120 KeV ($\mu_{poly.st}$ = 1.49) is similar to that of water (μ_{water} = 1.505). The contrast-enhanced X-ray image and resultant intensity variation are shown in Figure 2.4. The maximum deviation of the experimental value from the theoretical gas fraction, obtained from the phantom diameters, is found to be 0.45% (4.5x10^{-3}) in absolute value.

2.2.3. LOCAL AND OVERALL GAS FRACTION EVALUATION

The current X-ray system, in spite of its good pixelwise spatial resolution, has a limited temporal resolution, with an acquisition rate of 20Hz; at this low acquisition rate, the pixelwise gas fraction will contain an error induced by the blurring motion of the bubbles. As the pixel size (0.2 mm) is much smaller than the typical bubble sizes (3 mm), averaging of the pixelwise data is required, both spatially and temporally. Pixel-binning is done by considering a rising 3 mm bubble with typical velocity of 0.3 m/s. In 1/20sec, the bubble would create a vertical blur of 15 mm. In a dense bubbly flow, the flow is predominant in the vertical direction ($v_y >> v_x$), the bubble wiggle distance is taken as 1.5 times typical bubble diamter, i.e., 4 mm. This is done in order to obtain enough data points for a lateral gas fraction profile. To calculate the local gas fraction, the pixelwise gas fraction data is spatially averaged over a window size of 15 mm x 4 mm. Furthermore, the data is cumulatively averaged over 15 seconds, to reduce the fluctuations to less than 5% of the value.

In order to determine the overall gas fraction, the top surface is tracked using X-ray imaging. Note that this height does not include the foam layer at the top, as the amount of liquid in the foam is beyond the sensitivity of our X-ray measurements. As can be seen in Figures 2.13 and 2.6, the thickness of this foam layer is few millimetres. Hence, its exclusion introduces an error in the overall gas fraction smaller than 0.4% (4x10^{-3}) in absolute value.

2.2.4. HIGH SPEED IMAGING: BUBBLE SIZE MEASUREMENT AND BUBBLE IMAGE VELOCIMETRY (BIV)

Quantitative visualization is performed using a high-speed camera (PCO.dimax s4, 2016 x 2016 pixels resolution, at 1000 fps) to obtain the bubble size distribution and the bubble velocity.

Bubble size: In order to characterize the sparger, images of the bubbles, rising from an individual sparger, are captured 10 mm above the sparger surface. The field of view is 17 mm x 17 mm (118.6 pixel/mm resolution), focused at the mid-sparger depth. With a shallow focal depth (few mm, with an aperture f/1.8), in-plane bubbles are separated from the bubbles in the background. Overlapping bubbles from close-by planes are segmented using distance transform watershed method. The images are analysed using an open source image processing software FIJI, to obtain the bubble size distribution. The purpose of this measurement is two-fold: (i) to understand the influence of salt addition

on bubble size distribution in the plume originating from each sparger, (ii) to provide the average bubble size, used as an input for a simple 1D mechanistic model (described in Section 2.7).

Bubble velocity: Bubble image velocimetry (BIV) technique is used to compute bubble velocity in the disengagement zone. In BIV, similar to traditional PIV technique, the correlation between successive images is used to determine the bubble velocity. However, unlike the traditional PIV technique, BIV does not require a laser illumination [25]. Images are acquired at 1000fps in the disengagement zone with a field of view of 20 cm x 20 cm. Using a shallow focal depth (with aperture f/1.8), the *texture* of the gas-liquid interface can be captured with shadowgraphy imaging, similar to a sheet illumination. Subsequently, the images are inverted and cross-correlated using standard PIV algorithms in LaVision DaVis 8.0 software.

2.3. SALT EFFECT ON BUBBLES FORMED AT THE SPARGER

Bubble growth is dependent on the sparger type (material, pore size and spacing) [7]. The airstone type spargers used in the current study have smaller and closely packed pores, in comparison with others used in bubbly flow investigations (needle, ring-type and spyder-type). Since, bubble size in the column is dependent on the bubble size during growth, it is essential to determine the bubble size distribution (BSD) at the sparger.

Bubble sizes are measured from bubble images, acquired 10mm above the surface of an individual sparger. Images captured along the width of the sparger, give an indication of the size distribution and width of the rising plume. In the water case, the BSD is unimodal with a peak diameter around 2.3 mm (Figure 2.5a). In the salt case, however, the distribution changes to bimodal with increasing C_s, with a large fraction of micron size bubbles. This is due to the inhibition of coalescence between the bubbles during the growth stage [15]. These smaller bubbles cluster towards the core of the bubble plume, as shown in Figure 2.5b. Figure 2.5b shows the modes of the bubble size distribution along the bubble plume. Bubbles rising along the side surface of the sparger have longer contact times, leading to a higher probability of coalescence; therefore, larger bubbles are the observed towards the edges of the plume. An increase in flow rate or addition of salt increases the overall number of bubbles, thereby increasing the net bubble-bubble interactions. A direct impact is observed by the measurement of the bubble plume width, as shown in Figure 2.5c.

With the current spargers, the interaction of bubbles is much higher than in a large pore spyder-type sparger, used in the recent work of Besagni and Inzoli [16]. Consequently, the effect of the salt induced coalescence inhibition on the bubble size distribution close to the sparger is much larger, in comparison to their work.

2.4. FLOW PATTERNS

Figure 2.6 shows the effect of salt addition on flow patterns in the airlift column. In the water case, no or little bubble recirculation is observed. High speed images above the sparger plate, qualitatively show the results obtained in Figure 2.5a. Bubble of sizes in the range 2-3 mm are measured (Figure 2.7d(left)). Due to a typical low slow slip, the bubbles are dragged into the top part of the downcomer section (below the airlift separator) along with the recirculating liquid, only to be balanced by the counteracting

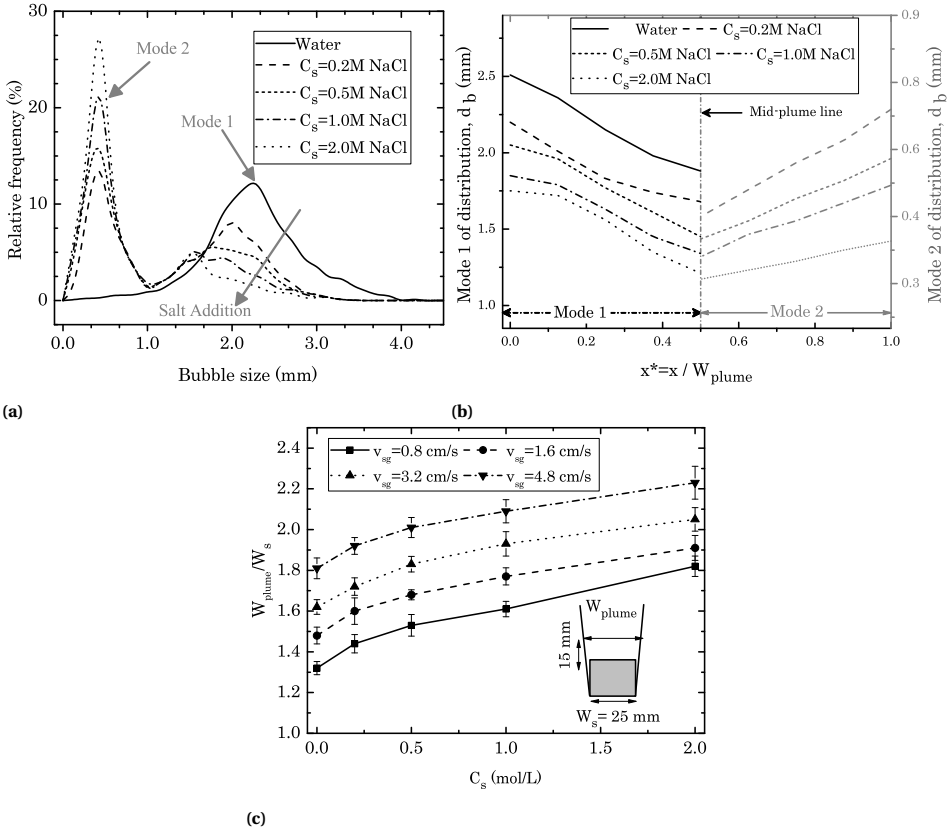

Figure 2.5: (a) Bubble size distribution in the plume above an individual sparger (measured 1 cm above the surface), v_{sg}=1.6cm/s. (b) Variation of modes of bubble size distribution as a function of lateral coordinate in the plume, v_{sg}=1.6cm/s (corresponding modes 1 & 2 of the distribution are depicted in figure 2.5a). (c) Non-dimensional plume width for different v_{sg}. Note that these single sparger measurements are performed at half the inlet gas flow rates used in airlift bubble column experiments. The superficial velocities, v_{sg} is calculated based on the cross-sectional area of the riser section (100 mm x 100 mm).

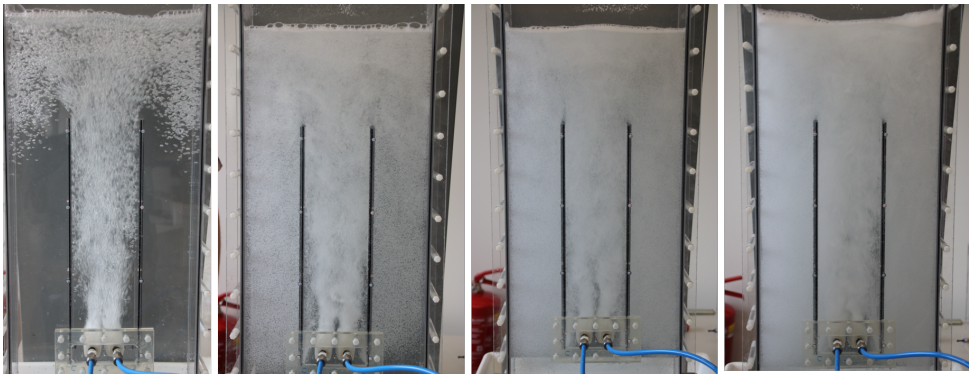

Figure 2.6: Salt effect on the flow pattern, at v_{sg}=1.6cm/s.

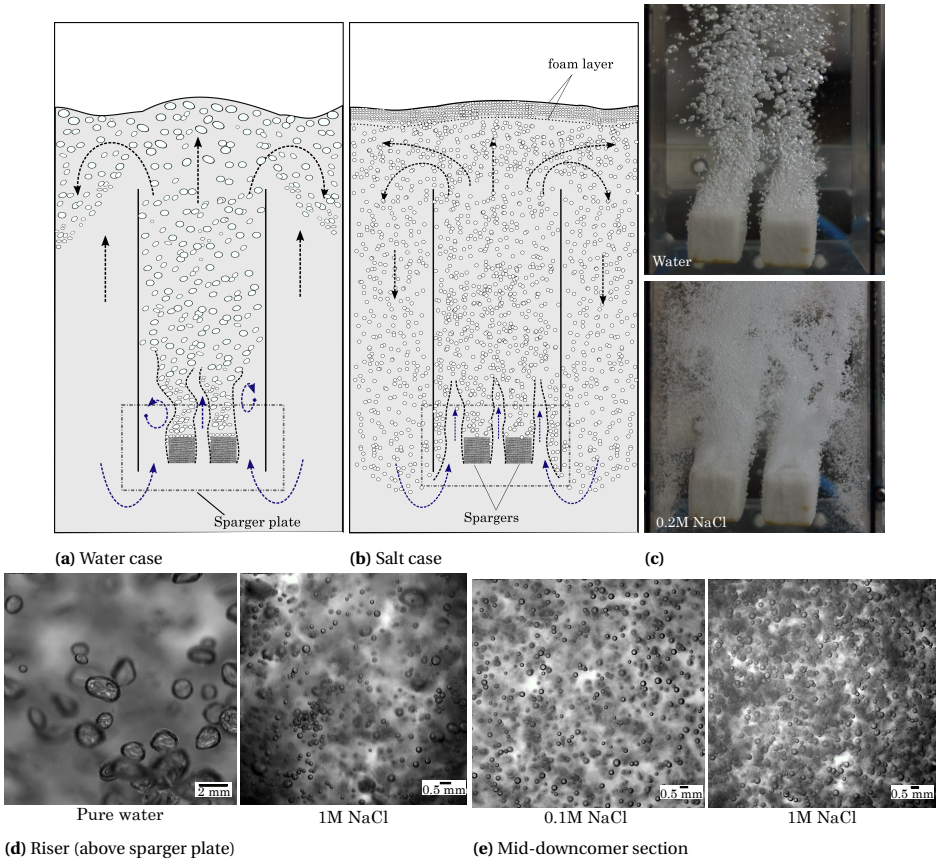

(a) Water case **(b)** Salt case **(c)**

(d) Riser (above sparger plate) **(e)** Mid-downcomer section

Figure 2.7: Schematic of flow patterns: (a) Water case (b) Salt case ; (c) Snapshots of the sparger region at v_{sg} = 1.6cm/s, top: Water, bottom: 0.2M NaCl ; (d & e) High speed images of the bubbles at v_{sg} = 1.6cm/s (field of view: 17 mm x 17 mm): (d) riser section (above the sparger plate) (e) mid-downcomer section.

buoyancy force, illustrated in Figure 2.7a. The resulting recirculation creates a oscillatory behaviour between the riser section and the two-legs of the downcomer sections. Liquid recirculation affects the bubble plume rising from the sparger, meandering the plume closer to the center of the riser section (Figure 2.7c (top)). With increasing gas superficial velocity, an increased gas carryover to the downcomer section is observed, which can be attributed to an increase in liquid circulation velocity.

With increasing NaCl concentration, C_s, Figure 2.6 shows an increase in bubble recirculation, leading to a higher degree of opaqueness of the flow. Owing to the salt-induced coalescence suppression at the sparger, bubbles as small as 150-200 μm are observed (Figure 2.7d (right)). Due to the lack of sufficient buoyancy force, these bubbles recirculate into the downcomer section. With an increasing C_s, a fractional increase in small bubbles at the sparger (Figure 2.5a), leads to a net increase in the fraction of smaller bubbles recirculating into the downcomer section (Figure 2.7e). Similarly with higher v_{sg}, micron size bubbles are predominant, due to a lower contact time between the bubbles during growth. The recirculating bubbles rise along the walls of the riser section (Figure 2.7c (bottom)) and interact with the bubble plumes above the sparger plate.

Other effect of salt addition is the formation of a finite layer of foam (typical a few mm in thickness) at the top liquid free surface. This is a result of accumulation of micron size bubbles, from coalescence inhibition at the spargers. These bubbles do not disengage from the column, as the salt concentration in the inter-foam liquid prevents it from coalescing with the continuum gas [26]. Consequently, as seen in Figure 2.6, the thickness of the foam layer increases with increasing salt concentration, C_s. Oscillation of the free surface, with and without the foam layer is relevant for the dynamics of the disengagement zone. This is discussed further in section 2.8.

2.5. LOCAL GAS FRACTION IN THE RISER SECTION

The profile of the time-averaged local gas fraction above the sparger plate, shows an expected M-shape profile (Figure 2.8a). The peaks correspond to the gas fraction at the centers of the fine-pore spargers. With increasing superficial velocity (v_{sg}), there is an increase in overall number of bubbles, and thus an increased gas fraction. However, the lateral profiles are similar in structure.

At a constant flow, with addition of salt, the bubble plume widens (Figure 2.8b). This is a result of the interaction of the bubble plumes with the recirculating bubbles. Besides this, the liquid velocity between the plume and the wall is lower than the velocity in the sparger gap, due to the dispersed bubbles. The resulting difference in entrainment leads to asymmetry and the core of the plume moving towards the wall. Similar observations were made by Freire *et al.* [27], studying plume-plume and plume-wall interactions.

The lateral gas fraction profile along the riser section for two superficial velocities (v_{sg}=0.8 cm/s and 3.2 cm/s) are shown in Figure 2.9. With an increase in v_{sg}, the profiles are structurally similar, with few differences. At a higher superficial velocity, there is larger fraction of recirculating bubbles, which is consistent with visual observation. At higher gas flow, with larger number of bubbles, there is a net higher buoyancy force in the plume. This results in a higher degree of meandering of the plume. Width of the individual plume also increases, due to a strong bubble dispersion in the longitudinal direction. Consequently, the plume merging is slightly faster (or at an earlier height) than at a lower flow rate. Beyond 25% of riser height (h= H_R/4), flattening of the radial

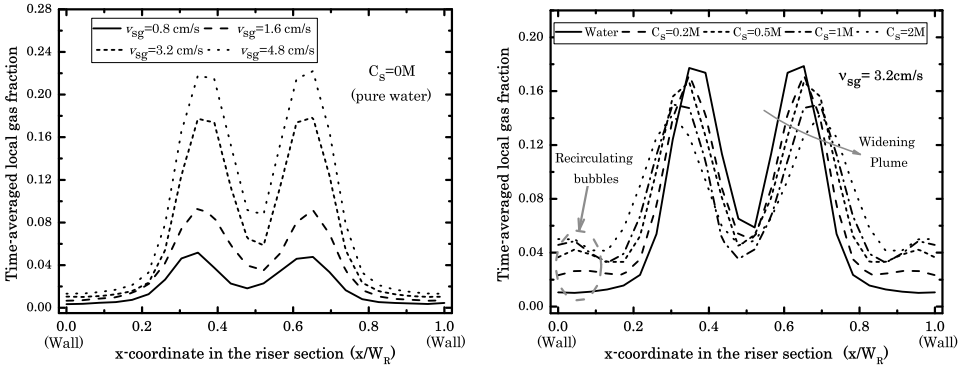

(a) **(b)**

Figure 2.8: Gas fraction profile in riser section (measured above the sparger plate, 250 mm from the bottom of the column): (a) Effect of gas flowrate without salt; (b) Effect of salt addition with gas superficial velocity, $v_{sg} = 3.2cm/s$. Same measurement locations have been used to compare pure water and salt cases.

.

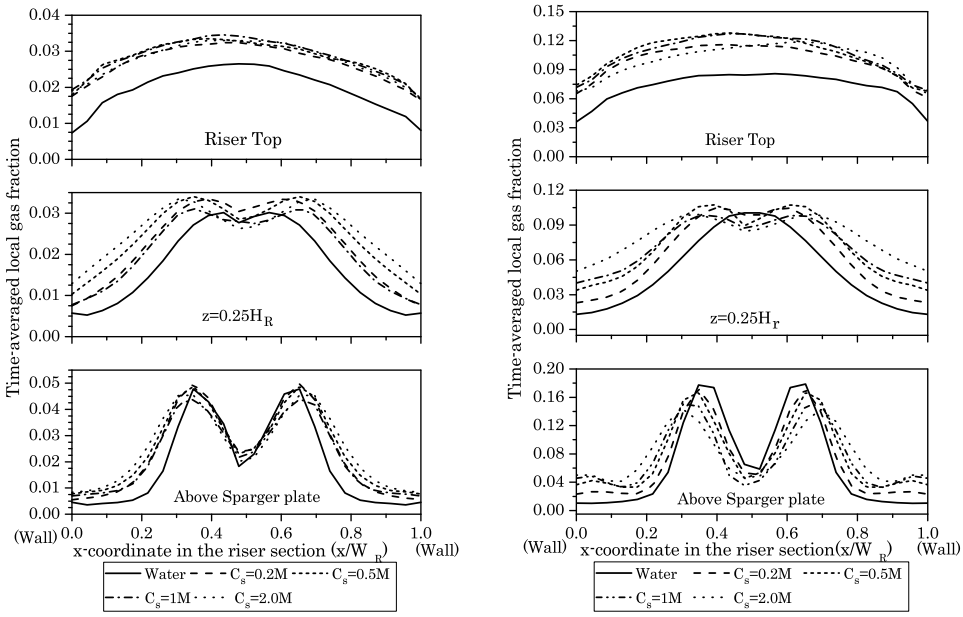

(a) $v_{sg} = 0.8cm/s$ **(b)** $v_{sg} = 3.2cm/s$

Figure 2.9: Gas fraction in the riser section for (a) v_{sg} = 0.8cm/s and (b) v_{sg} = 3.2cm/s. Measurement locations: distance from bottom of the column (z), Above sparger plate: z= 250 mm; $H_R/4$: z= 340 mm; Riser top: 580 mm.

gas fraction profile is observed. At the riser top, the flow reaches a homogeneous radial profile. There is a clear distinction between the water and the salt case, whereas the actual concentration of the salt has little effect on the local gas fraction.

2.6. OVERALL GAS FRACTION AND EFFECT OF INITIAL LIQUID HEIGHT

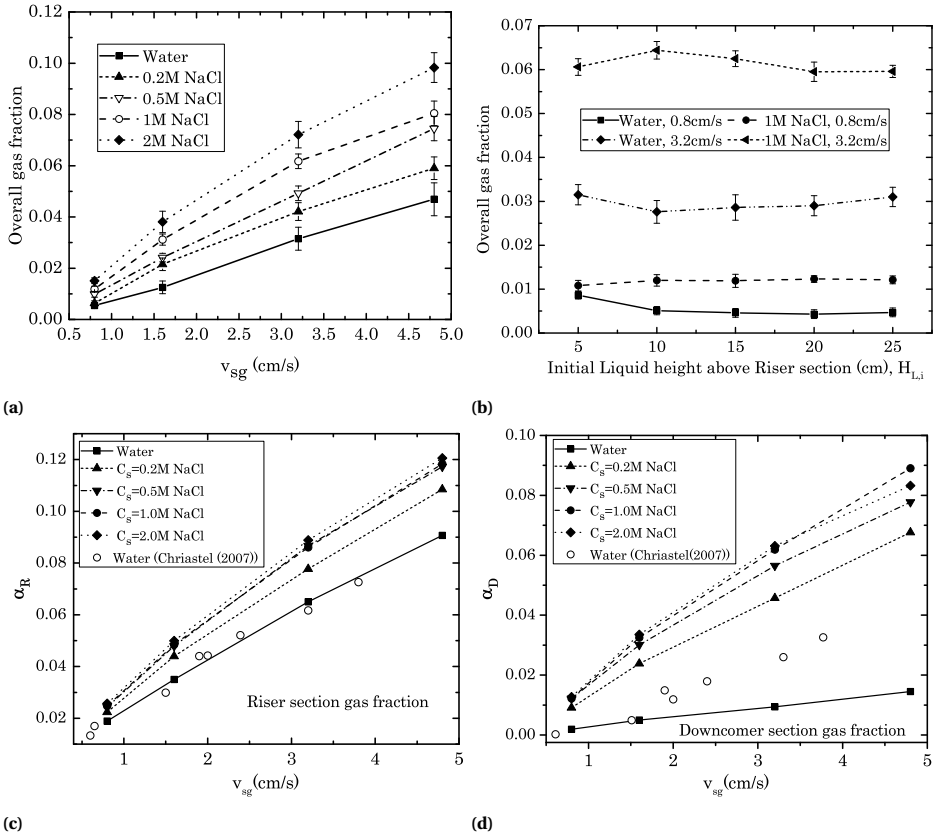

Figure 2.10: (a & b) Overall gas fraction as a function of: (a) superficial gas velocity, v_{sg}, for initial height $H_{L,i} = 15cm$; (b) Initial liquid height, $H_{L,i}$. (c & d) Section-wise averaged gas fraction (c) Riser section (data for salt concentrations, C_s=0.5M,1.0M and 2.0M are close to each other) ; (d) Downcomer section. Lines are for visual purposes and do not indicate a trend.

The overall gas fraction, measured by increase in liquid height is shown in Figure 2.10. The linear dependence of gas fraction with the superficial velocity is a characteristic of a flow in homogeneous regime. Previous studies on airlift columns with a sea water salt concentrations (0.15M), show an increase in overall gas fraction [28]. Studies in bubble columns, with a wide range of electrolyte concentrations [16, 29, 30], observed no effect or even a slight decrease in the gas fraction beyond the transition concentration ($C_{trans} \approx 0.17$M), owing to the formation of bubble clusters with rise velocities larger

than individual small bubbles. In the current study however, no bubble clusters are observed. Increased gas fraction beyond C_{trans} can be attributed to enhanced recirculation of gas bubbles (Figure 2.6) and thus increased residence times for smaller bubbles. Section-wise gas fraction, for riser and downcomer sections (Figures 2.10c and 2.10d), show a marginal change at higher salt concentrations.

The initial liquid height is an important parameter in design of airlift columns. Experiments performed with five different initial liquid heights ($H_{L,i}$) shows a non-effect on the overall holdup, within experimental error (Figure 2.10b). This is the case for both water and electrolyte situations, at different superficial gas velocities. Slight difference at $H_{L,i}$ =5 cm (liquid height above the riser section) is due to squeezing effect on the recirculating two phase flow caused by the close proximity of the free surface to the separator plate.

2.7. MECHANISTIC MODEL FOR BUBBLE SIZE EFFECTS

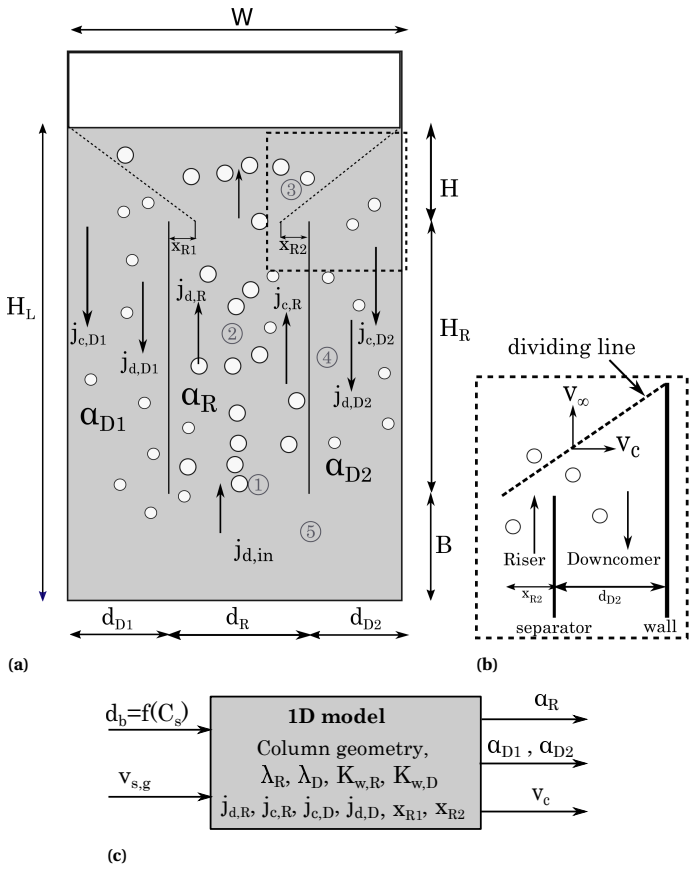

Figure 2.11: (a) Schematic of the drift flux model with different zones marked: 1-Sparger section, 2-Riser (above sparger plate), 3-disengagement zone, 4-downcomer section, 5-bottom gas recirculation (b) Modelling of gas-carryover into downcomer section (c) Variables involved in the 1D model (see appendix for equations).

In previous sections, electrolyte effects on the local and global gas fractions have been explained as a consequence of its impact on the bubble size distribution at the fine-pore spargers. We use a simple 1D-mechanistic model, based on the drift flux method [31], to understand the effect of bubble size on the hydrodynamics of the airlift column. The goal here is to see whether a consequence of variation in bubble size is consistent with the experimental observations on salt effects.

A schematic of two-phase flow in the airlift column is set up as shown in Figure 2.11a. The drift flux model is based on a steady state mechanical energy balance between the gravity forces and the frictional forces. Driving force for recirculation is the density differences between the riser and the downcomer sections (zone 2 and 4 in Figure 2.11a). The frictional effects are due to wall friction and flow reversals at the top disengagement section (zone 3) and bottom (zone 5). The model is further explained in Appendix 2.A.

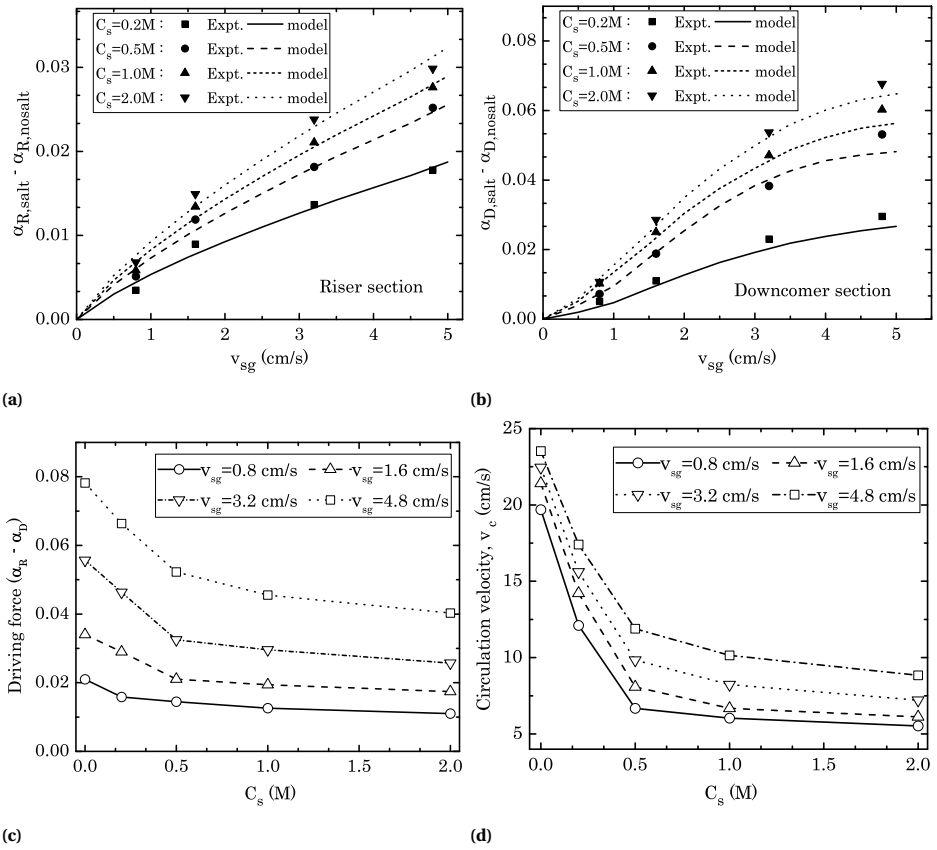

Figure 2.12: (a & b) Comparison of the experimental results with the 1D model: gas fraction increase due to salt addition in (a) riser section ($\alpha_{R,salt}$ - $\alpha_{R,nosalt}$); (b) downcomer section ($\alpha_{D,salt}$ - $\alpha_{D,nosalt}$) (c) Overall driving force for recirculation $\alpha_R - \alpha_D$ (experimental data from X-ray imaging) (d) Liquid recirculation velocity (from 1D model). The input for the model for various salt concentrations is $d_{b,avg} = f(C_s)$.

A standard implementation of the model does not consider the effect of gas recirculation on the increased riser section gas fraction; hence, requires additional experimen-

tal input via. measurement of the liquid superficial velocity in the downcomer section (usually measured with salt-tracer techniques [32]). In order to better explain the bubble size effect on recirculation, instead of the additional measurements, we consider a model for the gas-carryover into the downcomer section, as shown in Figure 2.11b. At the top disengagement section (zone 3), a zero horizontal slip velocity is assumed. This way, bubble rising out of a section of the column (defined by the dividing line), manage to escape towards free surface, while the trajectories below the dividing line, flow into the downcomer section.

Input parameters for the model are the inlet superficial gas velocity, v_{sg} and average bubble size $d_{b,avg}$, obtained from the bubble size distribution (BSD) at an individual sparger, for the corresponding salt concentration (for example, refer to Figure 2.5a for v_{sg} = 1.6 cm/s). The model is iteratively solved for gas fractions in the riser (α_R) and downcomer (α_D) sections, and liquid circulation velocity, v_c.

Increase in gas fractions, due to addition of salt, for riser ($\alpha_{R,salt}$ - $\alpha_{R,nosalt}$) and downcomer sections ($\alpha_{D,salt}$ - $\alpha_{D,nosalt}$), are compared with the average of local gas fractions (from X-ray measurements) in zones 2 and 4, respectively. Figures 2.12a and 2.12b show reasonable agreement between the experiments and the 1D model, for different salt concentrations and gas superficial velocities. The global effect of salt is a reduction in the driving force for airlift action (Figure 2.12c), as a consequence of lower rise velocities of smaller bubbles. This is also reflected through a reduction in liquid circulation velocity v_c, obtained from the model for increasing C_s (Figure 2.12d). For its simplistic nature and the assumptions, the 1D steady state drift flux model reasonably explains the effect of salt as primarily through its effect on the average bubble size at the sparger.

2.8. DISENGAGEMENT ZONE DYNAMICS

Understanding the interaction of bubbles with the liquid free surface is essential in determining the gas disengagement from the column. For the case of airlift column, free surface oscillations also have an influence on the gas-carryover to the downcomer section. Considering a 'degassing' boundary in modelling the top surface introduces a bias in the calculation of the global liquid circulation and can further lead to an underestimation in gas-carryover to the downcomer section [33].

In the previous section, behavior of the bubbles at the disengagement zone was explained using a simple mechanistic model. As seen from the flow profiles (Figure 2.6), addition of salt leads to formation of a foam layer, which can be attributed to reduction in the bubble sizes and accumulation of these sub-millimetre size bubbles at the free surface. To better understand the effect of salt and the resultant bubble size distribution on the bubble recirulation, a study of the disengagement zone dynamics is necessary. High-speed visualization and bubble image velocimetry (BIV) techniques are used to this extent. Raw and BIV processed images, along with the post-processing steps, are available in the 4TU data repository [2].

Figure 2.13a shows a snapshot and the resultant bubble velocity profile of the disengagement zone for the water case, at v_{sg} = 1.6 cm/s. The free surface forms a spout, with a width stretching till close to mid-downcomer section. A strong upward velocity is maintained in the bubble plume core until the free surface, where the no-shear stress boundary condition changes the flow orientation to horizontal direction. Bubbles to the

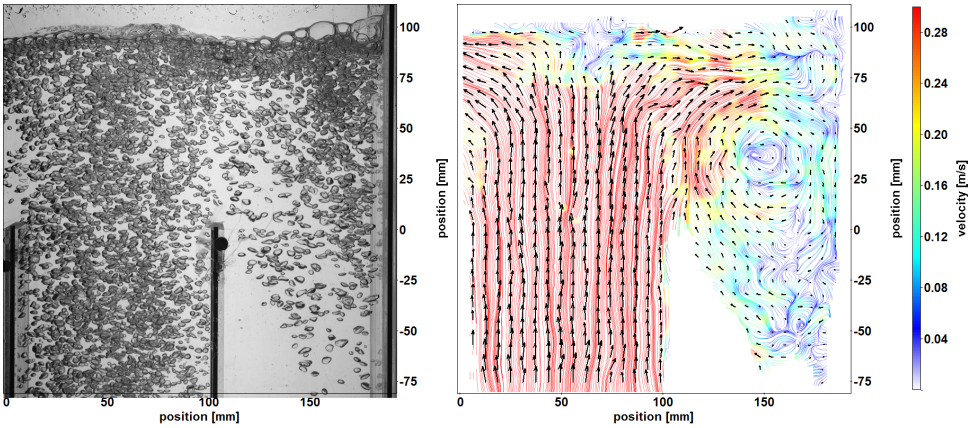

(a) Water, $v_{sg} = 1.6 cm/s$

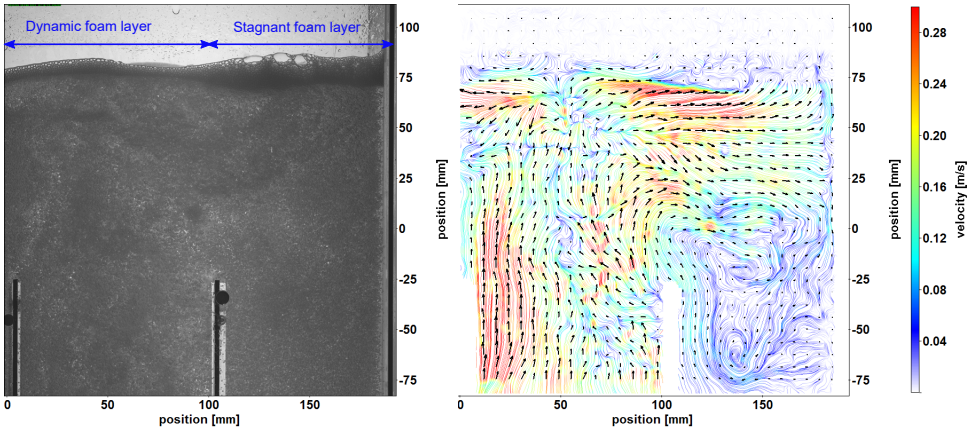

(b) 0.2M NaCl, $v_{sg} = 1.6 cm/s$

Figure 2.13: Effect of foam dynamics on flow in the disengagement zone: (left) snapshot of the flow pattern, (right) vector arrows and streamline profile from bubble image velocimetry (BIV)

edge of this plume, are pushed towards the side of the disengagement zone, forming a large vortex above the downcomer section. Close to the wall, the interface is affected by the vortex motion, caused by the recirculation of bubbles (from downcomer section), rising to the surface.

For the salt case (0.2M NaCl, v_{sg} = 1.6 cm/s), two regions of the foam layer can be observed: a stagnant part (above the downcomer section) and a dynamic part (above the riser section), as shown in Figure 2.13b (left). The dynamic foam layer grows in thickness, due to the accumulation of micron-size bubbles, until sloshed by the kinetic energy dissipation of bubble plumes from the riser section. As the bubbles sizes are much smaller, when compared to the water case, a strong upward flow is not maintained in the core of the bubble plume rising out of riser section (Figure 2.13b (right)). The foam layer acts as a stagnation boundary, making the flow strongly horizontal and thereby steadily shearing the dynamic part of the foam layer. These sheared bubbles are dragged towards the column wall and into the downcomer section, leading to additional gas carryover. Unlike the water case, there is no clear vortex in the disengagement zone. Instead, a large meandering low velocity zone is observed, well into the downcomer.

The role of salt in the dynamics of disengagement zone is reflected through its effect on the bubble sizes. At higher salt concentrations, a thicker foam layer is observed. The timescale of the foam sloshing depends on the swarm velocity in the bubble clusters, a function of the bubble size distribution and the gas superficial velocity. The simple mechanistic model based on the average bubble size, as explained in the previous section, captures the key aspect that larger bubbles from the riser section tend to rise up towards the surface and the smaller ones deviate towards the side of the disengagement zone. Further study of the free surface foam layer, as a boundary condition is essential, as it allows to accurately predict the flow in the downcomer section.

2.9. CONCLUSIONS

In this study, a detailed experimental investigation into the hydrodynamics of an airlift bubble column have been performed, for a wide range of salt concentrations (0-2M NaCl).

Our results explicate that the role of salt is primarily through the coalescence inhibition and resultant impact on the bubble size distribution (BSD) at the sparger. Salt addition creates smaller sub-millimetre sized bubbles, when compared to the pure water case. The bubble size distribution at the sparger region dictates the integral bubble plume behaviour and the local gas fraction profiles in the airlift column. A direct consequence of the reduction in bubble sizes is the large residence times of recirculating bubbles and thereby an increase in overall gas fraction, even beyond the transition salt concentration (C_{trans}). The effect of salt through the bubble size can be understood with a simple mechanistic model for the disengagement region.

Salt, through its effect on the bubble size, also leads to formation of a foam layer at the top liquid free surface, changing the dynamics of the disengagement region. Qualitative behaviour of the disengagement region is studied with a bubble image velocimetry (BIV) technique. Since this region plays an important role in modelling of gas recirculation, understanding the salt effect on bubble sizes can lead to improved models. Further modelling of the free surface should include the foam layer with relevant time scale of foam formation and sloshing. The entire set of data from the current effort can be used

to validate more sophisticated models for dense bubbly flows, for which does not exist much detailed data; the X-ray imaging proved itself to be a powerful technique to fill this gap.

ACKNOWLEDGEMENTS

The authors thank Christiaan Schinkel for help with BIV post-processing; Bert Vreman and Johan Lif for proposing the flow configuration and salt concentration range, for constructive discussions, and for feedback on the manuscript. The authors also acknowledge additional financial support from Nouryon PPC business unit.

APPENDIX

2.A. DRIFT-FLUX MODEL

Drift-flux model is used to solve two-phase flows in pipes, bubble columns, airlift columns etc., considering the mixture as a whole, rather than two separate phases. The model is based on existence of a slip velocity between the two phases, as a condition for surface motion. The superficial velocities of the dispersed gas phase (j_d) and the continuous liquid phase (j_c) are related to the gas fraction by a correlation from the work of Richardson and Zaki [34], as:

$$(1-\alpha)\frac{j_d}{v_\infty} - \alpha\frac{j_c}{v_\infty} = \alpha(1-\alpha)^n \tag{2.4}$$

Where, v_∞ is the terminal velocity of a single rising bubble in an infinite medium and the exponent, n, is a function of the Reynolds number (Re) as 4.45 for $Re \in [1;500]$ and 2.39 for $Re \geq 500$. v_∞ as a function of the bubble size, can be obtained from the emperical curve, proposed by Clift *et al.* [35, p. 172]. For the riser and the downcomer sections, separate versions of Eqn. 2.4 are set up, as the gas fractions in both sections will be different.

For flow between riser and each half of the downcomer sections (illustrated in 2.11a), a mechanical energy balance between the driving force of the gas fraction difference and the frictional resistance is defined as:

$$\underbrace{H_L \cdot g\rho_L(\alpha_R - \alpha_{D,i})}_{\text{Driving force for recirculation}} = \underbrace{\lambda_{fR}\frac{H\rho_{m,R}}{d_R}j_{c,R}^2 + \lambda_{f,D,i}\frac{H\rho_{m,R}}{d_{D,i}}j_{c,D,i}^2}_{\text{Pressure drop due to longitudinal flow}} + \underbrace{K_{w,R}\rho_L j_{c,R}^2 + K_{w,D,i}\rho_L j_{c,D,i}^2}_{\text{Pressure drop due to 90° bends}} \tag{2.5}$$

Where, i =1,2 denotes each half of the downcomer sections. Detailed derivation of equation 2.5 and correlations for the friction factors ($\lambda_{f,R}$,$\lambda_{f,D,i}$,$K_{w,R}$ and $K_{w,D,i}$) are available from the work of Chriastel *et al.* [32]:

$$\lambda_{f,R} = 0.21\frac{\sqrt{gd_R}}{j_{c,R}}\sqrt{\alpha_R}; \quad \lambda_{f,D,i} = 0.28\frac{\sqrt{gd_b}}{j_{c,D,i}}\sqrt{j_{c,D,i}}; \quad K_{w,R} = \frac{1}{(1-\alpha_R)^2}; \quad K_{w,D,i} = 2 \tag{2.6}$$

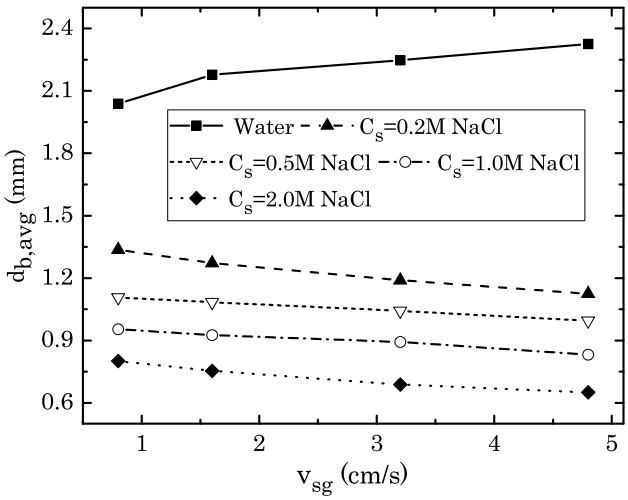

Figure 2.14: Average bubble size, $d_{b,avg}$, measured from a single sparger

where, $d_b = d_{b,avg} = f(C_s)$ is the average bubble diameter, obtained from the bubble size distribution measurements.

Figures 2.14 and 2.15 show respectively, the measured bubble size distribution and $d_{b,avg}$, for all salt concentrations (C_s) and superficial velocities (v_{sg}) used in current work. The liquid circulation velocity, v_c is obtained by a simple mass balance for the liquid phase.

$$2 v_c H = d_R j_{c,R} \tag{2.7}$$

Similarly, the gas superficial velocities are coupled as:

$$A_R j_{d,R} = A_R j_{d,in} + A_{D1} j_{d,D1} + A_{D2} j_{d,D2} \tag{2.8}$$

Where, A_R, A_{D1} and A_{D2} are respectively the cross-sectional areas of the riser and two legs of the downcomer section. $j_{d,in} = v_{sg}$ is the inlet gas superficial velocity. The gas-carryover to the downcomer section is formulated based on a dividing line (shown in Figure 2.11b). Here, $x_{R,i}$ (i=1,2) is defined as the regions close to the wall of the riser section, where the flowing bubbles are dragged into the corresponding downcomer section. The gas phase superficial velocity in the downcomers can be estimated from:

$$\begin{aligned} j_{d,D,i} = \frac{x_{R,i}}{d_R} j_{d,R} \quad \text{if} \quad x_{R,i} \le 0 \rightarrow j_{d,D,i} = 0 \\ \frac{x_{R,i} + d_{D,i}}{H} = \frac{v_c}{v_\infty} \end{aligned} \tag{2.9}$$

It is noted here that the circulation velocity v_c is defined as the actual velocity and not the superficial velocity.

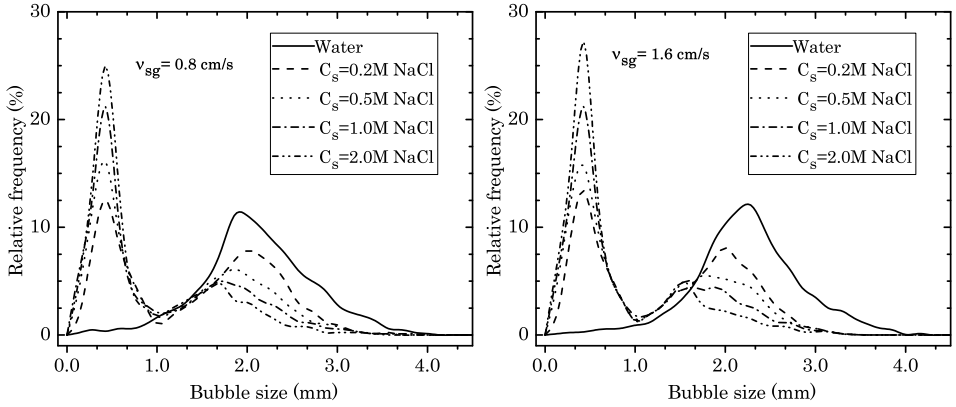

(a) $v_{sg} = 0.8 cm/s$

(b) $v_{sg} = 1.6 cm/s$

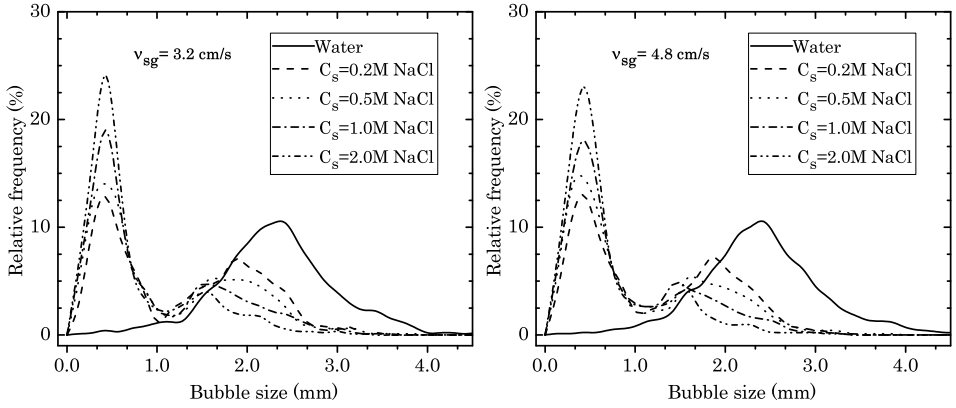

(c) $v_{sg} = 3.2 cm/s$

(d) $v_{sg} = 4.8 cm/s$

Figure 2.15: Bubble size distribution (BSD) in the plume above individual sparger for all superficial velocities

Table 2.1: Electrolyte effect on physical properties of water at $20^{\circ}C$ [36]

Salt Conc. C_s, M NaCl	Density ρ, kg/m^3	Viscosity μ, Pa.s, x10^{-3}	Surface Tension σ, mN/m
0 (water)	999	1.002	72.2
0.2	1010	1.04	72.8
0.5	1022	1.06	73.4
1.0	1042	1.104	74.8
2.0	1085	1.22	76.4

REFERENCES

[1] M. M. Mandalahalli, E. C. Wagner, L. M. Portela, and R. F. Mudde, *Electrolyte effects on recirculating dense bubbly flow: An experimental study using x-ray imaging,* AIChE Journal **66**, e16696 (2020).

[2] M. Mandalahalli, E. Wagner, L. M. Portela, and R. Mudde, *Experimental data: electrolyte effects on hydrodynamics in an airlift bubble column [dataset],* 4TU.ResearchData (2023), 10.4121/15087255.v1.

[3] W. Liu, C. Moran, and S. Vink, *A review of the effect of water quality on flotation,* Minerals Engineering **53**, 91 (2013).

[4] D. Jean and D. Lee, *Effects of salinity on expression dewatering of waste activated sludge,* Journal of colloid and interface science **215**, 443 (1999).

[5] N. Deen, R. Mudde, J. Kuipers, P. Zehner, and M. Kraume, *Bubble columns,* in *Ullmann's Encyclopedia of Industrial Chemistry* (Wiley-VCH Verlag GmbH & Co., 2010).

[6] J. Heijnen and K. V. Riet, *Mass transfer, mixing and heat transfer phenomena in low viscosity bubble column reactors,* The Chemical Engineering Journal **28**, B21 (1984).

[7] S. Sharaf, M. Zednikova, M. C. Ruzicka, and B. J. Azzopardi, *Global and local hydrodynamics of bubble columns–effect of gas distributor,* Chemical Engineering Journal **288**, 489 (2016).

[8] R. F. Mudde, W. K. Harteveld, and H. E. A. van den Akker, *Uniform flow in bubble columns,* Industrial & Engineering Chemistry Research **48**, 148 (2009).

[9] H.-P. Luo and M. H. Al-Dahhan, *Local characteristics of hydrodynamics in draft tube airlift bioreactor,* Chemical Engineering Science **63**, 3057 (2008).

[10] J. Quinn, M. Maldonado, C. Gomez, and J. Finch, *Experimental study on the shape–velocity relationship of an ellipsoidal bubble in inorganic salt solutions,* Minerals Engineering **55**, 5 (2014).

[11] R. R. Lessard and S. A. Zieminski, *Bubble coalescence and gas transfer in aqueous electrolytic solutions,* Industrial & Engineering Chemistry Fundamentals **10**, 260 (1971).

[12] M. Ruzicka, *On dimensionless numbers,* Chemical Engineering Research and Design **86**, 835 (2008).

[13] V. S. Craig, B. W. Ninham, and R. M. Pashley, *The effect of electrolytes on bubble coalescence in water,* The Journal of Physical Chemistry **97**, 10192 (1993).

[14] M. Firouzi, T. Howes, and A. V. Nguyen, *A quantitative review of the transition salt concentration for inhibiting bubble coalescence,* Advances in Colloid and Interface Science **222**, 305 (2015).

[15] S. Orvalho, M. C. Ruzicka, and J. Drahos, *Bubble column with electrolytes: gas holdup and flow regimes,* Industrial & Engineering Chemistry Research **48**, 8237 (2009).

[16] G. Besagni and F. Inzoli, *The effect of electrolyte concentration on counter-current gas–liquid bubble column fluid dynamics: Gas holdup, flow regime transition and bubble size distributions,* Chemical Engineering Research and Design **118**, 170 (2017).

[17] Y. Fu and Y. Liu, *Development of a robust image processing technique for bubbly flow measurement in a narrow rectangular channel,* International Journal of Multiphase Flow **84**, 217 (2016).

[18] C. Boyer, A.-M. Duquenne, and G. Wild, *Measuring techniques in gas–liquid and gas–liquid–solid reactors,* Chemical Engineering Science **57**, 3185 (2002).

[19] J. Gómez-Hernández, S. Sánchez-Delgado, E. Wagner, R. F. Mudde, and J. R. van Ommen, *Characterization of tio2 nanoparticles fluidization using x-ray imaging and pressure signals,* Powder Technology **316**, 446 (2017).

[20] S. Rabha, M. Schubert, M. Wagner, D. Lucas, and U. Hampel, *Bubble size and radial gas hold-up distributions in a slurry bubble column using ultrafast electron beam x-ray tomography,* AIChE journal **59**, 1709 (2013).

[21] T. A. Kingston, T. A. Geick, T. R. Robinson, and T. J. Heindel, *Characterizing 3d granular flow structures in a double screw mixer using x-ray particle tracking velocimetry,* Powder Technology **278**, 211 (2015).

[22] T. J. Heindel, *A review of x-ray flow visualization with applications to multiphase flows,* Journal of Fluids Engineering **133**, 074001 (2011).

[23] A. Kastengren and C. F. Powell, *Synchrotron x-ray techniques for fluid dynamics,* Experiments in fluids **55**, 1686 (2014).

[24] J. Alles and R. Mudde, *Beam hardening: Analytical considerations of the effective attenuation coefficient of x-ray tomography,* Medical physics **34**, 2882 (2007).

[25] Y. Ryu, K.-A. Chang, and H.-J. Lim, *Use of bubble image velocimetry for measurement of plunging wave impinging on structure and associated greenwater,* Measurement Science and Technology **16**, 1945 (2005).

[26] A. Bhakta and E. Ruckenstein, *Decay of standing foams: drainage, coalescence and collapse,* Advances in colloid and interface science **70**, 1 (1997).

[27] A. P. S. Freire, D. D. Miranda, L. M. Luz, and G. F. França, *Bubble plumes and the coanda effect,* International journal of multiphase flow **28**, 1293 (2002).

[28] A. Sánchez Mirón, F. Garcia Camacho, A. Contreras Gomez, E. M. Grima, and Y. Chisti, *Bubble-column and airlift photobioreactors for algal culture,* AIChE Journal **46**, 1872 (2000).

[29] J. H. Kluytmans, B. G. van Wachem, B. F. Kuster, and J. C. Schouten, *Gas holdup in a slurry bubble column: influence of electrolyte and carbon particles,* Industrial & engineering chemistry research **40**, 5326 (2001).

[30] C. P. Ribeiro Jr and D. Mewes, *The influence of electrolytes on gas hold-up and regime transition in bubble columns,* Chemical Engineering Science **62**, 4501 (2007).

[31] G. B. Wallis, *One Dimensional Two-Phase Flow* (New York: McGraw-Hill, 1969).

[32] L. Chriastel, Y. Kawase, and H. Znad, *Hydrodynamic modelling of internal loop air-lift reactor applying drift-flux model in bubbly flow regime,* The Canadian Journal of Chemical Engineering **85**, 226 (2007).

[33] S. Talvy, A. Cockx, and A. Line, *Modeling hydrodynamics of gas–liquid airlift reactor,* AIChE Journal **53**, 335 (2007).

[34] J. Richardson and W. Zaki, *The sedimentation of a suspension of uniform spheres under conditions of viscous flow,* Chemical Engineering Science **3**, 65 (1954).

[35] R. Clift, J. Grace, and M. Weber, *Bubbles, Drops and Particles* (New York: Academic Press, 1978).

[36] W. M. Haynes, *CRC handbook of chemistry and physics: a ready-reference book of chemical and physical data* (Boca Raton : CRC Press, 2009).

3

ELECTROLYTE AND TEMPERATURE EFFECTS IN A RISING BUBBLE

"All truths are easy to understand once they are discovered; the point is to discover them."

~ Galileo Galilei, *Dialogue Concerning the Two Chief World Systems* (1632)

In this work, the rise characteristics of a single H_2, bubble in the ellipsoidal regime, in (i) water, (ii) single electrolyte (2 M, 4.5 M NaCl) solution and (iii) various concentrations of electrolyte mixture (up to 6.4 M of 1:5 weight fraction NaCl-$NaClO_3$), have been studied, at temperatures up to 80° C. Our results show that both individual and collective effects of the temperature and the electrolyte concentration on the bubble size, the rise velocity, and the bubble shape, are purely dependent on the changes in liquid properties (density, viscosity, and surface tension); the bubble motion can be described by known non-dimensional correlations for clean bubble rise in pure fluids. .

This chapter is part of industrial collaboration work with Nouryon Pulp and Performance Chemicals and has been published as M.M. Mandalahalli, J. Lif, R.F. Mudde, and L.M. Portela, *Electrolyte and temperature effects in a rising bubble*, Chemical Engineering Science, **270**, 118276 (2023) [1].

NOMENCLATURE

Greek symbols

σ	Surface tension [mN/m]
ρ	Liquid density [kg/m^3]
μ	Liquid viscosity [Pa.s]
χ	Bubble aspect ratio [-]

Other symbols and abbreviations

Re	Reynolds number[-]
Eo	Eötvös number [-]
Mo	Morton number [-]
We	Weber number [-]
C_D	Drag Coefficient [-]
F_B	Bouyancy force[N]
F_σ	Surface tension force [N]
$\mathrm{U_b}$	Bubble rise velocity [m/s]
F_B	Bubble rise velocity [m/s]
U_T	Terminal rise velocity [m/s]
T	Liquid temperature [°C]
d_{eq}	Equivalent bubble diamter [mm]
d_N	Nozzle inner diameter [mm]

Subscripts

emp	Empirical
$expt$	Experimental

3.1. INTRODUCTION

Gas-liquid unit operations are widely used in many (bio)-chemical processes, such as electrolysis, wastewater treatment, froth-flotation, and Fischer-tropsch synthesis [e.g. 2, 3]. An essential aspect of the design and scale-up of the gas-liquid contacting equipment, such as bubble and airlift columns, is a phenomenological understanding of the interactions between the two phases. Changes in process conditions (temperature, pressure, pH, etc.) or the presence of dissolved substances (salts, surfactants, etc.) can have a strong influence on the hydrodynamic parameters (gas holdup, bubble size distribution, rise velocities) and, thereby, influence the performance of these processes. While many industrial processes are operated at non-ideal conditions of high pressure/temperature in presence of contaminants [4], current design models are mostly based on well-known bubble rise characteristics in pure fluids at ambient conditions. It is therefore of interest to better understand the micro-phenomena at industrially-relevant conditions, even for a single bubble. In the current work, we focus on the effects of the liquid temperature and dissolved electrolytes at high concentrations on the rise characteristics of a single ellipsoidal bubble.

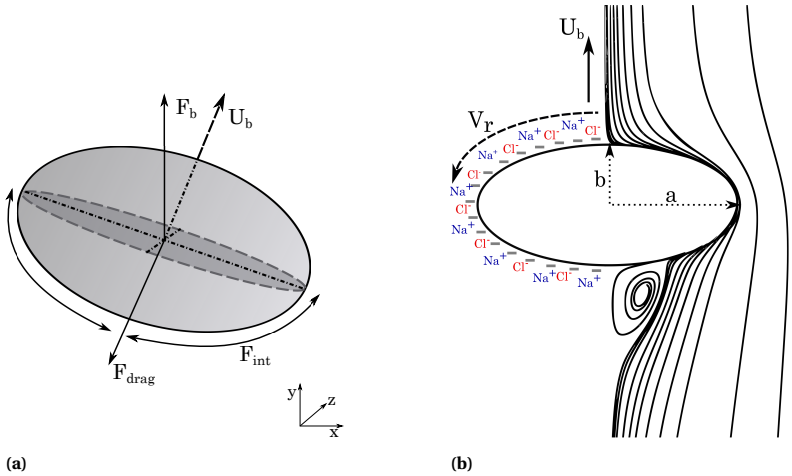

Figure 3.1: Schematic of an ellipsoidal rising bubble, with a velocity (U_r). Panel (a): forces acting on a rising bubble (F_b: buoyancy force; F_{drag}: Drag force; F_{int}: Interfacial tangential force). Panel (b) : Axisymmetric flow around an ellipsoidal bubble in an electrolyte (NaCl); the relative velocity at the interface (V_r) is strongly dependent on the interfacial rheology, therefore, it could depend on the concentration and ionic properties of Na^+ and Cl^-.

The rise characteristics of a single bubble have been extensively studied, analytically, numerically and experimentally [e.g. 5, 6]. A fundamental understanding of the bubble shapes and rise velocities is based on the counteracting buoyancy and drag forces acting on the rising bubble, as schematized in Figure 3.1a. Buoyancy is a volume force, dependent on the equivalent bubble diameter (d_{eq}) and the density difference ($\Delta\rho$). For a spherical bubble rising with a free-slip interfacial condition, the drag force is known to be dependent only on the Reynolds number ($Re = \rho U_b d_{eq}/\mu$) [7]. For a larger and deformable bubble ($Re \gtrapprox 10^2$), however, surface tension (σ) plays a strong role in dictating the shape and, thereby, the drag force acting on the bubble.

In the case of pure fluids, such as deminarilized water, the bubble rise characteristics can be expressed in terms of three independent non-dimensional numbers, those which collectively include the liquid properties (density ρ, viscosity μ, and surface tension σ), the rise velocity (U_b) and the bubble size (d_{eq}). Most commonly used in the subject are: Reynolds number ($Re = \rho U_b d_{eq}/\mu$), Eötvös (Eo=$\rho g d_{eq}^2/\sigma$), Morton (Mo=$\mu^4 g/\rho\sigma^3$) and Weber (We=$\rho U_b^2 d_{eq}/\sigma$). This is well-known from the *classical* empirical regime map from Clift *et al.* [8] and non-dimensional correlations [9, 10].

Rheological effects due to a presence of ions or surface-active molecules introduces an additional interplay between the gas-liquid interface and the surrounding flow, leading to a no-free shear interface (schematized in Figure 3.1b). These interfacial effects depend on the nature of the contaminant (salt, surfactant, etc.) and its concentration. A well-studied example is the case of a bubble rise in tap water, where a higher resistance to the bubble motion and a reduction in rise velocity is attributed to additional tangential stress caused by a non-uniform surface concentration, as adsorbed trace molecules at the interface are advected to the rear of the bubble [11]. Bubble size and generation method also influences the contaminant effect on the bubble motion; the slower the bubble generation, the higher the surfactant concentration at the interface [12].

In the case of dissolved electrolytes, ions usually are repelled from the gas-liquid interface. Resulting electrostatic repulsions and ionic mobility result in an increase in interfacial tension. Ion interactions at the interface are further explained in detail in Appendix 3.B. At low concentrations (0.1-1.0 M (moles/liter)), due to a marginal increase in surface tension, electrolytes can be considered as a weak contaminant. However, earlier investigations [13, 14] observed that low concentrations ($\mathcal{O}$(0.1 M)) is sufficient to cause a strong reduction in the rise velocity for ellipsoidal bubbles ($d_{eq} \sim 2$ mm). On the contrary, recently, Hessenkemper *et al.* [15] showed only a marginal decrease and noted that higher concentrations would be required to significantly affect the rise velocity. While, investigations differ in their conclusions, the studies are limited to a maximum concentration of 1M (mol/liter); there are no significant changes to the liquid properties in this range. At higher concentrations, a large presence of ions close to the interface can influence the dynamic surface characteristics. Meanwhile, an increase in all three liquid properties (ρ, μ, σ) can also play a significant role in the rise characteristics.

An increase in the liquid temperature from ambient conditions has a strong influence on the properties of the liquid. Whereas a lower liquid density reduces the buoyancy force, a decrease in both viscosity and surface tension can affect the drag force experienced by the bubble. There are only limited studies in the literature for the case where the gas bubble and the liquid are in thermal equilibrium [5]. For temperature up to 45 °C, Zhang *et al.* [16] and Leifer *et al.* [17], respectively, observed a non-effect and a increase in the rise velocity with an increase in the temperature. Studying bubble rise at two temperatures: 10 °C and 90 °C, Okawa *et al.* [18] showed a decrease in the rise velocity at the higher temperature. While the available literature studies are performed in deminarlized water, the experimental data does not agree with predictions for pure fluids (from Clift *et al.* [8]). A systematic understanding of the temperature effect on the rise characteristics is therefore required.

In the current work, we study the effects of liquid temperature (up to 80 °C) and strong (mixture) electrolytes (up to saturated concentrations of sodium chlorate-chloride mixtures in water), both individually and collectively, on the bubble shape and the rise

velocity. The purpose here is to determine whether a change in the rise characteristics under the conditions of high temperature and electrolyte concentrations can be explained by currently-known pure fluid correlations, based entirely on the changes in the corresponding liquid properties.

3.2. EXPERIMENTAL METHODOLOGY

3.2.1. FLUIDS USED: PHYSICAL PROPERTIES

The gas-liquid system used in the current experiments is relevant for industrial Chlor-alkali and Chlorate electrolysis processes. Electrolytes used are sodium chloride (NaCl, ACS analytical grade, ≥ 99.5% pure) and sodium chlorate ($NaClO_3$, industrial grade, ≥ 99.6% pure). Hydrogen gas is used as the gas phase. Demineralized Water, solution of sodium chloride in water (2 M, 4.5 M) and four concentrations of sodium chloride-chlorate mixture (1:5 weight fraction of NaCl:$NaClO_3$) are used as liquids. Four mixture concentrations correspond to 1.28 M (20% mix.), 2.56 M (40% mix.), 3.85 M (60% mix.), and 6.4 M (100% mix.) in ionic strength. 100% mixture is prepared by mixing 100 g/L and 500 g/L of NaCl and $NaClO_3$,respectively and further diluted to obtain 20%, 40% and 60% mixtures. Experiments are performed at four temperatures: 25, 40, 60, and 80 °C. Mixture concentration is chosen to avoid precipitation of the salts at all temperatures. Liquid properties (density, viscosity, and surface tension) for all liquids used in the current experiments are listed in Table 3.1 in Appendix 3.A . Density data is determined from weight measurements of each fluid in a 100 ml standard bottle at several temperatures. The viscosity measurements at several temperatures are done using a Ostwald viscometer. The density and viscosity data (in Table 3.1) is based on a correlation derived from a series of measurements at different temperatures, with a typical accuracy of 2 kg/m^3 and 0.05x10^{-3} Pa.s, respectively. These surface tensions of fluids are measured using axisymmetric drop shape analysis method (ADSA) [19]. The ADSA measurement technique and the results have been explained in Appendix 3.C.

3.2.2. EXPERIMENTAL SETUP

The experimental apparatus is shown in Figure 4.2. The experiments are carried out in a jacketed cylindrical column 0.750 m x 0.15 m (height x diameter). Temperature in the column is controlled using hot water flow through the jacketed part, connected to a thermostatic water bath. Temperature, measured using a wire probe, shows a maximum deviation of 0.4 °C throughout the column. Hydrogen bubble in the column is injected through a single submerged needle of internal diameter 0.13 mm. Flow through the needle is controlled using a precision dosing meter (MetroOhm Dosimat 876). The submerged gas inlet tubing ensures that the generated bubble and the liquid are at the same temperature. In order to generate bubbles at a low frequency, ensuring a slow growth of the bubble at the needle, the flow rate is set at 0.1 ml/min (≈ 1 bubble every 2.5 seconds). Electrolyte solutions are prepared separately and added to the column. For electrolyte corrosion resistance, both the needle and the needle holder are made out of titanium. Hydrogen, compared to dissolving CO_2 gas, has a low solubility in both water and brine [20, 21]; any dissolution effect during the bubble rise can be ignored. A continuous flow of hydrogen bubbles can create an explosive mixture with ambient air at the top surface of the liquid, with a flammable limit of 4% H_2 in air (v/v) [21]. To avoid this,

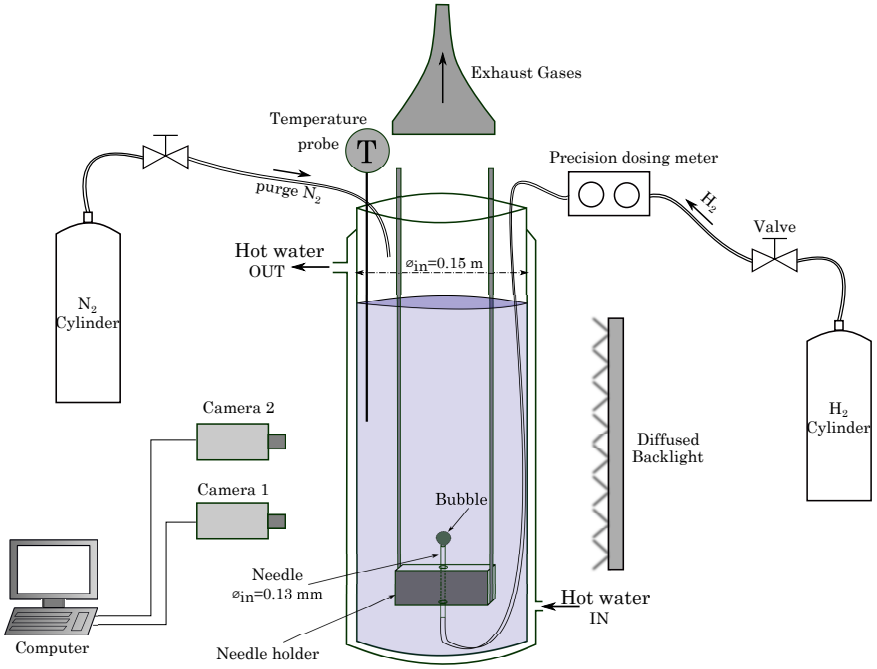

Figure 3.2: A schematic of the experimental setup. Water flow in the jacketed part of the column is connected to a thermostatic water bath (not shown in the figure).

the liquid surface is purged with a continuous flow of N_2 gas.

Images of a single bubble released from the needle are acquired using two high-speed USB cameras (Basler Aca-1920-150uc, max. resolution 1920x1200 px^2, 200 fps). Camera 1, as shown in the schematic, is used to measure the growth of the bubble, with a pixel resolution of 75.8 pixel/mm. This camera is further raised to capture images at mid-column height, in order to measure the bubble shapes at terminal conditions. Camera 2, with a resolution of 17.5 pixel/mm, is used to acquire bubble motion through the column for trajectory and velocity calculations. Bubble path is captured by overlapping field-of-views up to a height of 270 mm. Illumination of the region is provided by a white-backlight. Considering that typical lateral motion of an ellipsoidal bubble ($\approx$ 1.8 mm) is ca. 10 mm $\ll$ column diameter (150 mm), any elongation effects in bubble shapes, due to refractive index changes at the column curvature, can be ignored. Acquired images are processed with open-source software FIJI [22] to obtain bubble characteristics, as described further.

3.2.3. IMAGE ANALYSIS

A selected sequence of images is analyzed to obtain bubble geometrical and motion parameters. The sequence of the image processing steps is shown in Figure 4.3. From raw images, the bubble outlines are generated using three steps: (i) Background homogenization and subtraction (ii) binarization (iii) shape detection. The outlines are further analyzed to obtain, for each frame, centroid coordinates (x,y), the vertical and horizon-

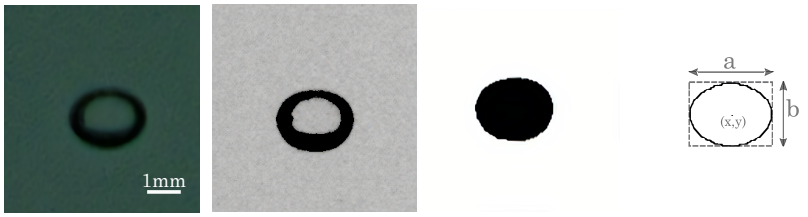

Figure 3.3: Image processing steps in FIJI software

tal diameters of the bubble, a and b respectively. The bubble equivalent diameter d_{eq} is evaluated with an assumption of a spheroidal shape, with the vertical axis as the symmetry axis. The bubble aspect ratio χ is defined as the ratio of horizontal to vertical dimensions of a bounding rectangle. The mean rise velocity is measured considering only the vertical displacement of the bubble between several frames.

$$\chi = a/b; \qquad d_{eq} = \left(a^2 b\right)^{1/3} \tag{3.1}$$

3.3. RESULTS AND DISCUSSION

3.3.1. BUBBLE SIZE AND RISE VELOCITY

Bubble diameter measured just before detachtment at the needle, for all experimental cases, is as shown in Figure 3.4a. For the water-case, there is a decrease in the bubble size with an increase in the temperature. However, with increasing electrolyte concentration a reversal in this trend is observed. This can be explained by considering the forces acting on the bubble during its growth. Nature of gas sparging has a strong influence on the growth and rise of bubbles [23]. The bubbles generated here have a low initial distortion; flow through the needle is controlled to ensure complete bubble growth before detachment. In the absence of inertia and viscous forces, bubble growth is determined by the competing buoyancy force ($F_b = \Delta\rho g V_b$) and the surface tension force ($F_\sigma = \pi d_N \sigma$). At a lower temperature, though there is an increase in the liquid density with the addition of electrolyte, a corresponding increase in surface tension retards the bubble growth. At a higher temperature, with a strong reduction in the surface tension and a relatively marginal decrease in $\Delta\rho$, buoyancy force is favoured. For high electrolyte mixtures (60% and 100% mix. mixtures), however, an increase in the bubble size with temperature is observed.

Average rise velocity (Figure 3.4b) shows generally a decrease with increase in temperature, except for higher electrolyte concentrations (60 % and 100% mixtures). While the initial bubble size and changes in fluid composition or temperature have been known to influence the rise velocity in the ellipsoidal bubble regime (1.5 mm $\leq d_{eq} \leq$4 mm) [5], an interplay between the viscous and the surface tension forces needs to be considered. For a better understanding of the relative effect of these forces, a non-dimensional analysis is required.

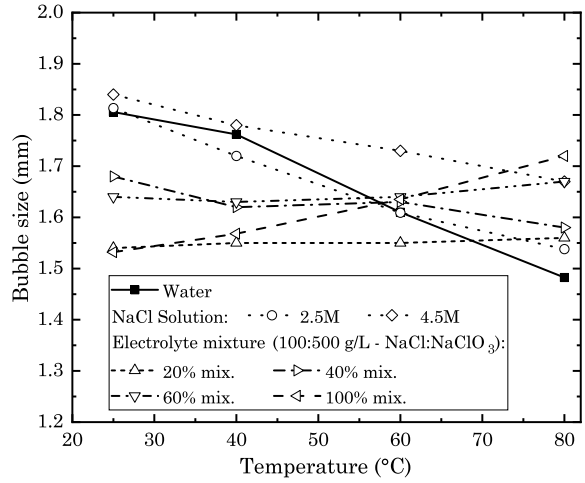

(a)

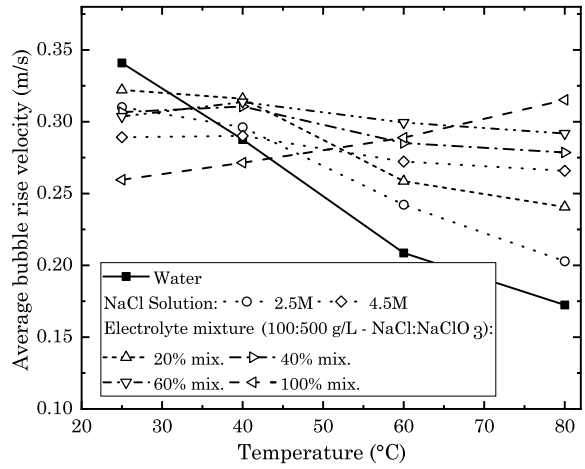

(b)

Figure 3.4: Effect of electrolyte addition and temperature on (a) Average bubble size at the needle. (b) Bubble rise velocity. Obtained from 5 measurements with a deviation of 2.5% and 5.7%, respectively for bubble size and rise velocity.

3.3.2. NON-DIMENSIONAL ANALYSIS

COMPARISON WITH CLIFT MAP

The four forces acting on the bubble (viscous, inertial, surface tension, and buoyancy) can be described in terms of three independent non-dimensional numbers. Among many those can be formed, the most common ones used in bubble physics are Reynolds (*Re*), Eötvös (*Eo*), Morton (*Mo*) and Weber (*We*) numbers. Several efforts have been made in literature studies to describe bubble shape and rise velocity in terms of these numbers [e.g. 5]. A well-known example is the classical empirical regime map (between *Re, Eo, Mo*) generated from experimental data for pure fluids and mixtures by Clift *et al.* [8].

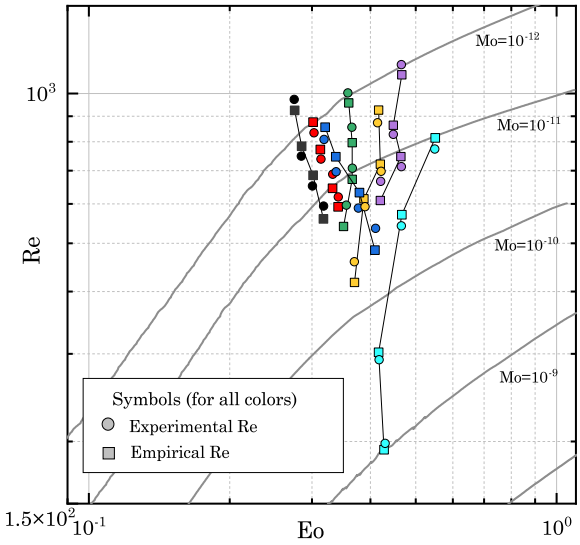
Mo=10^-12
Mo=10^-11
Mo=10^-10
Mo=10^-9
Re
Eo
10^3
1.5×10^2
10^-1
10^0
Symbols (for all colors)
Experimental Re
Empirical Re

(a)

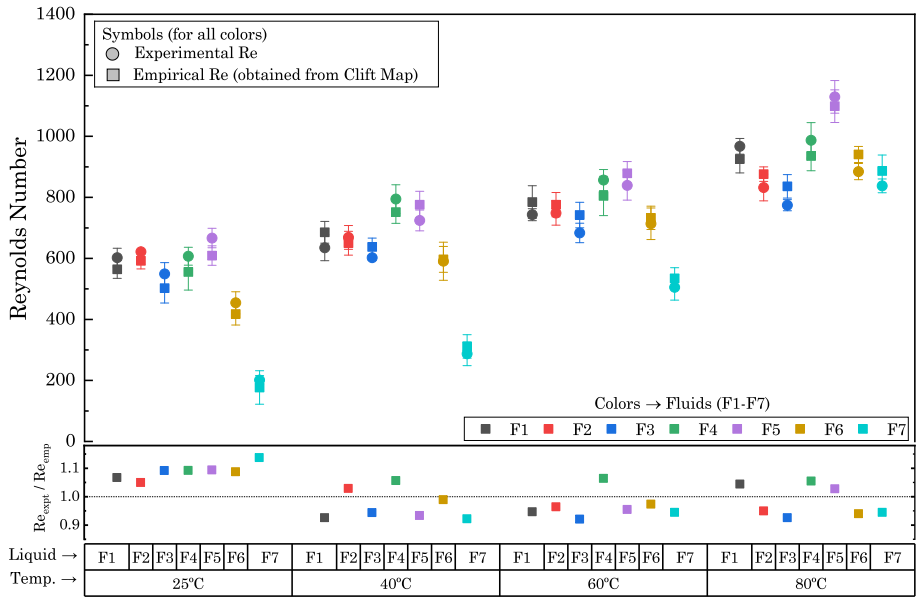
Symbols (for all colors)
Experimental Re
Empirical Re (obtained from Clift Map)
Reynolds Number
1400
1200
1000
800
600
400
200
0
Colors → Fluids (F1-F7)
F1 F2 F3 F4 F5 F6 F7
Re_expt / Re_emp
1.1
1.0
0.9
Liquid →
Temp. →
F1 F2 F3 F4 F5 F6 F7 F1 F2 F3 F4 F5 F6 F7 F1 F2 F3 F4 F5 F6 F7 F1 F2 F3 F4 F5 F6 F7
25°C
40°C
60°C
80°C

(b)

Figure 3.5: (a) Clift map [8] (zoomed-in) with overlay data from current experiments. Markers denote Reynolds number *Re* (: experimental, Re_{expt}; : empirical, Re_{emp}); colours depict individual fluids F1-F7 (defined in Table 3.1 in 3.A). Four data points for each fluid indicates temperature; *Re* increases with increasing temperature. Lines are added for visualization purpose and do not indicate any correlation. (b) Reynolds number data for all experimental cases. A comparison between Re_{expt} and Re_{emp}.

For a bubble of known size rising in a fluid with known physical properties (ρ, μ, σ), an empirical *Re* can be determined from the map. Re_{emp} is obtained from digitizing the *Eo-Re-Mo* data. Experimental Reynolds number, Re_{expt} is calculated from terminal rise velocity (U_T) and bubble size obtained at the needle. Figure 3.5a, shows an overlay plot of both *Re* on the relevant. A quantitative comparison (Figure 3.5b) gives a good agreement between them, with an average deviation of 6.1% . This indicates that the rise velocity of a bubble in strong electrolyte solutions at all temperatures can be obtained by knowledge of the bubble size and the properties of the fluids.

PARAMETERIZATION

A standard representation of the bubble motion in a liquid medium is based on the drag coefficient, C_D. When a terminal rise velocity is reached, there exists a balance between the buoyancy and drag forces, and the drag coefficient can be expressed as:

$$C_D = \frac{4 d_{eq} g}{3 U_T^2} = \frac{4}{3} \cdot \frac{Mo Re^4}{We^3} \tag{3.2}$$

Usually, the bubble rise is separated into three regimes [23]: (i) viscous force dominated regime, with small spherical bubble and $Re \lesssim 10^2$; (ii) surface tension dominated regime, with intermediate size ellipsoidal bubbles and $10^2 \lesssim Re \lesssim 10^3$. For a clean bubble in a pure liquid, if the bubbles are spherical, C_D= f(*Re*), and when the bubbles are not spherical (χ>1), C_D= f(*Re*, χ) [e.g. 10].

For spherical clean bubbles in a pure fluid, in the limit of very high *Re*, $C_D = 48/Re$, and, from Eqn 4.5, a correlation for the bubble motion can be derived as:

$$Re = 2.047 We^{3/5} Mo^{-1/5} \tag{3.3}$$

However, for spherical bubbles at low and intermediate values of *Re* ($Re \lesssim 10^3$), the theoretical expression of $C_D = 48/Re$ is not valid, as bubbles tend away from a spherical shape.

Rastello *et al.* [24] studied rising bubble in the silicon oils ($Mo \in [10^{-1}; 10^{-9}]$) and found an similar empirical correlation (the exponent of *We*, 3/5 ~ 2/3, for low *We* dependence)

$$Re = 2.05 We^{2/3} Mo^{-1/5} \tag{3.4}$$

This emprical correlation is also shown to be applicable to literature data on ultra-pure water (from [25]) for bubble size (d ∈ [0.5;1.5]). However, the agreement of experimental data with Eqn 3.4 is limited to $Re \lesssim 300$. The deviation has been attributed to the onset of bubble deformation at moderate *Re* and its influence on the drag force.

$$Re = 2.77 We^{2/3} Mo^{-1/5} \tag{3.5}$$

Current experimental data shows a good agreement with the correlation factor ($We^{2/3} Mo^{-1/5}$), as shown in Figure 3.6. While, the correlation being empirical in nature, an

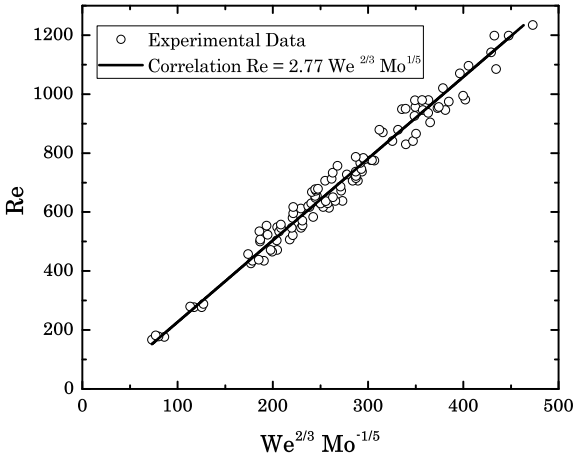

Figure 3.6: Correlation betweeen *Re*, *We*, and *Mo* for all the experiments considered in this study. The solid line shows the correlation Eq.3.5

increase in the proportionality factor for a clean bubble (from 2.05 to 2.77) can be attributed to the effects of bubble shape (discussed in the next subsection) and *Re*-regime ($\mathcal{O}(10^2 - 10^3)$). The theoretical calculations by Moore [10] are based on dissipation of the vorticity generated at the bubble surface, limited to a boundary layer ($\mathcal{O}(Re^{-1})$) and a stagnant wake ($\mathcal{O}(Re^{-1})$) regions; this assumption seems to be valid only in the viscous regime [26]. At higher *Re*, there is an increase in the aspect ratio which leads to an change in the pressure distribution along the bubble surface, ultimately contributing to an increase in drag.

It is important to note here that the *Re* correlation of Eqn. 3.5 describes the entire set of current experiments ($10^{-9} \leq Mo \leq 6x10^{-13}$, $0.74 \leq We \leq 2.94$), thereby strongly indicated the role of liquid properties in uniformly describing the rise characteristics of the bubble in strong electrolytes at varied temperatures.

BUBBLE DEFORMATION

Bubble deformation has been well-studied in terms of Weber number (*We*). Studying bubble rising in ultra-pure water ($d_{eq} < 1.8mm$), Duineveld [25] proposed a correlation for the bubble aspect ratio (χ):

$$\chi_w = \frac{1}{1 - \frac{9}{64} We} \tag{3.6}$$

For a variety of fluids, a description of the bubble deformation would require a second parameter to reflect the viscous effects, either *Re* or *Mo*. Legendre *et al.* [9], studying viscous liquids ($Mo < 10^{-3}$), proposed a dependency, based on *Mo*, for pure fluids as :

$$\chi_{pure} = \frac{1}{(1 - \frac{9}{64} We(1 + 0.2 Mo^{1/10} We)^{-1})} \tag{3.7}$$

The presence of contaminants introduces additional stresses on the interface. A resultant effect is the reduction of the bubble aspect ratio. Compiling an experimental

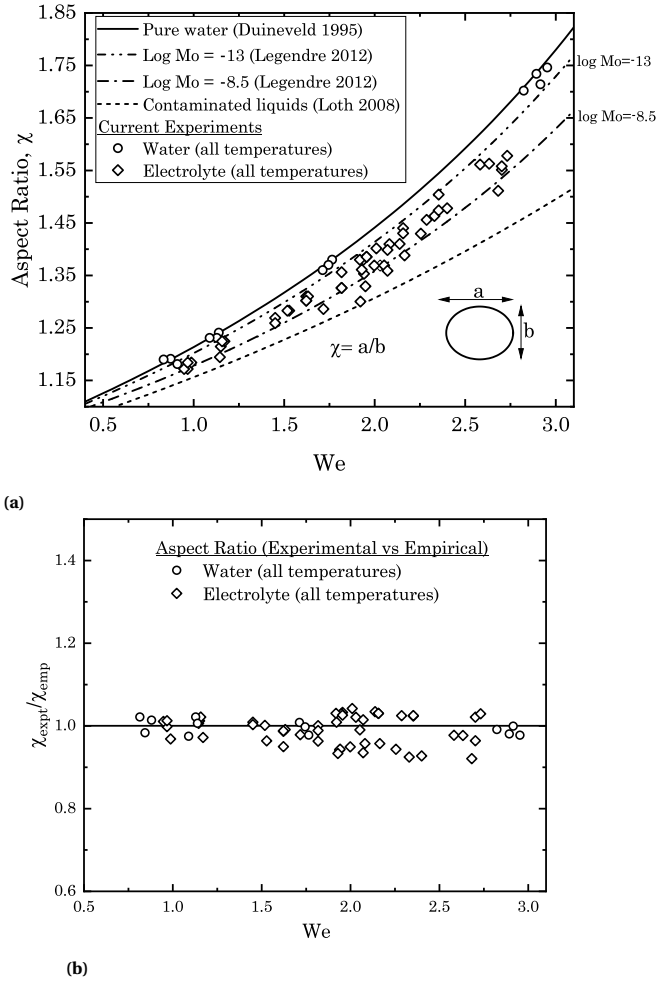

Figure 3.7: Bubble aspect ratio (χ): (a) all experimental cases ; (b) comparison with the empirical values, given by Eqn. 3.6 [25] (for water cases) and Eqn. 3.7 [9] (for electrolyte cases)

dataset of freely rising bubbles in contaminated solutions (surfactants, liquid mixtures, etc.), Loth [27] proposed an empirical correlation:

$$\chi_c = 1/(1-0.75\tanh(0.11We)) \tag{3.8}$$

In Figure 3.7, experimentally obtained aspect ratio data (χ_{expt}) is compared with the empirical correlations for pure and contaminated liquids. For a given *We*, only a marginal variation in the range of χ is observed, as expected from a $Mo^{1/10}$ dependence in low-*Mo* fluids. The current data shows a reasonable agreement with the pure liquids; a majority of data points are within the bounds defined by the range of *Mo* (-13 < log *Mo* < -8.5). Whereas a strong reduction in aspect ratio is expected for a bubble rise in contaminated solution, it is not observed in the current experiments with a strong concentration of electrolytes, at all temperatures. This might be due to a lack of surface

tension gradient along the bubble surface, as experimental studies on interfacial rheology ([28, 29]) show no dynamic behaviour at the interface due to presence of ions. This aspect is further discussed in Appendix 3.B.

DRAG COEFFICIENT

As mentioned earlier, the drag coefficient (C_D) is quite useful in understanding the bubble dynamics, especially for deforming bubbles. It is well-understood that shape effects and flow separation in the bubble wake cause an increase in C_D, leading to a deviation from a universal dependence on *Re* [e.g. 10, 27]. To describe C_D for a clean bubble in pure fluids, besides *Re*, another non-dimensional number would be required to take into account bubble deformation effects; most commonly used being *We* and *Mo*. While several empirical and theoretical correlations are available for the calculation of the drag coefficient (e.g. [5]), a majority of them are limited to lower *Re* ($Re < \mathcal{O}(10^2)$). A challenge being the accurate prediction of C_D in the ellipsoidal transition regime ($Re\,\mathcal{O}(10^2 - 10^3)$), values relevant for current work.

Rodrigue [30] proposed an empirical correlation (Eqn. 3.9) of C_D=f(*Re*,*Mo*), that shows excellent agreement with experimental data (from Haberman and Morton [31]) for a wide variety of pure liquids for the entire range of *Re*.

$$C_{D,emp} = \frac{16}{Re} \frac{\left[1 + 0.020\left(\left[\frac{3}{4} C_{D,emp} Re^2 Mo\right]^{8/9}\right)^{10/11}\right]^{10/11}}{\left[1 + 1.31\text{x}10^{-5} Mo^{11/20}\left(\left[\frac{3}{4} C_{D,emp} Re^2 Mo\right]^{8/9}\right)^{73/33}\right]^{21/176}} \tag{3.9}$$

A comparison of current experimental data ($C_{D,expt}$, calculated from Eqn. 4.5) with predictions from Eqn. 3.9, is presented in Figure 3.8, showing a good agreement, with a deviation of 7%. This indicates that the drag force acting on the bubble can be expressed based on the properties of the fluids.

For a bubble rising in contaminanted liquids, the presence of even trace quantities of surface-active molecules or ions introduces a no-slip interfacial condition at the bubble surface. Whereas specific effects of contaminants at the interface are dependent on its nature and concentration, for practical purposes, an understanding is based on an incremental increase in drag (ΔC_D^*) due to the change in the interfacial condition and a decrease in the aspect ratio. Hence, the Weber number (*We*) becomes a relevant parameter. From an experimental dataset of contaminated fluids, Loth [27] proposed a generalized equation for the drag coefficient $C_{D,c}$ (for $1 < We < 4$) as:

$$C_{D,c}(We) = C_{D,We\to 0} + \Delta C_D^* \cdot (C_{D,We\to\infty} - C_{D,We\to 0}) \tag{3.10}$$

Here, $C_{D,We\to 0}$ represents the case of a rigid sphere and $C_{D,We\to\infty}$ represents the spherical cap case at highest deformation. The corresponding equations from literature [32, 33] are:

$$C_{D,We\to 0} = \frac{24}{Re}[1 + 0.15 Re^{0.687}] \quad ; \quad C_{D,We\to\infty} = \frac{8}{3} + \frac{14.24}{Re} \tag{3.11}$$

As a function of *Re*, Eqn. 3.10 establishes a link between the two regimes: spherical and spherical cap, to predict the values of intermediate *Re*, where the deformation has a

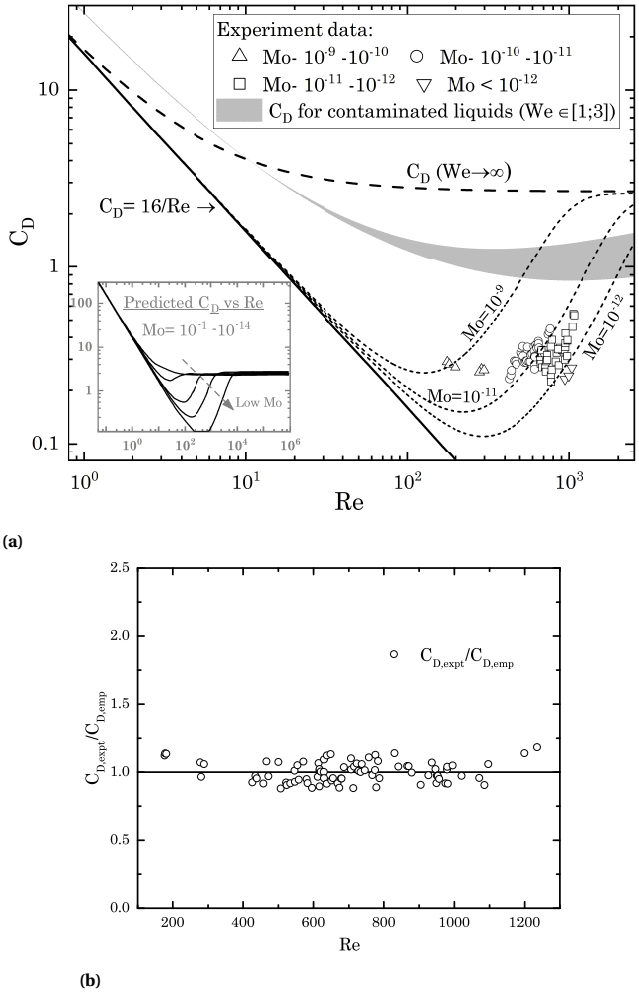

Figure 3.8: (a) C_D vs *Re* plot: symbols indicate the experimental C_D; dashed lines (- - - - - -) are empirical prediction lines for Mo= 10^{-9}, 10^{-11} and 10^{-12}; gray zone depicts the prediction for contaminated liquids as f(*Re*, *We*); inset shows predicted behaviour for the entire range of *Re*. (b) Comparison of experimental C_D with the empirical values from Eqn. 3.9 [30]

strong influence on C_D. Recently, Rastello *et al.* [34] showed that ΔC_D^* from Eqn 3.12 provided a good agreement with experimental data on tap water and contaminated silicon-oils, for $Re < 700$.

$$\Delta C_D^* = tanh(0.0055(WeRe^{0.2})^{1.6}) \tag{3.12}$$

$C_{D,c}$ for the current experimental range of $1<We<3$ (gray region in Figure 3.8) shows a clear dependence on We in the intermediate Re regime. However, the corresponding values for contaminated fluids are higher than the experimentally obtained C_D. Hence, the fluids used in the current study cannot be classified as contaminated.

A simpler drag coefficient equation can be obtained from the agreement of the experimental data with the empirical correlations (Eqns. 3.4 and 3.5). Considering a generalized equation:

$$Re = XWe^{2/3}Mo^{-1/5} \tag{3.13}$$

Where, X is 2.77 for the current data, in the intermediate Re regime, and 2.05 for the lower Re regime [9, 24]. In combination with Eqn. 4.5, C_D = f(Re, Mo) can be expressed as:

$$C_D = \frac{4}{3}X^{9/2}Mo^{1/10}Re^{-1/2} \tag{3.14}$$

This equation is valid for a wide range of Re ($10^{-1}< Re <10^3$) and for bubbles with limited deformation (1<We<4). At $We \gg 1$, the drag coefficent tends towards a constant value, consistent with a spherical cap shape [27]. For a pure fluid (given Mo), in the viscous dominated regime ($Re \lesssim 10^2$), Eqn. 3.14 describes the departure from an uniform drag behaviour for a spherical bubble. With a dependence of $Mo^{1/10}$, for a higher value of Mo the departure occurs at a higher C_D and at a lower Re. In the intermediate Re regime, a higher value of the prefactor (X) accounts for an increase in the deformation effects on C_D. Here, X can be considered as a function of We and Re; in the limited range of We, X is dependent only on Re regime. While derived from empirical correlations, from a practical perspective, a simple correlation (Eqn. 3.14) is useful in understanding the bubble behaviour for a variety of pure fluids, for $Re <10^3$.

3.4. CONCLUSIONS

In the present study, the rise characteristics of a H_2 bubble at different temperatures, in water, NaCl solution, and various concentrations of a mixture electrolytes, has been studied. Our results strongly suggest that for high electrolyte concentrations, both collective and individual effects of the electrolyte concentration and temperature on the bubble rise velocity, the drag coefficient, and the bubble shape can be explained by their effect on the liquid properties (density, viscosity, and surface tension); experimental data agrees with known correlations for clean bubbles in pure liquids. Furthermore, similar to the existing knowledge on pure liquids, the bubble rise can be fully described non-dimensionally with the knowledge of the Mo and We numbers.

The current conclusions for high concentrations should not be extended to low concentrations (0.1-1M); due to contradictory results [14, 15], it is not clear if the presence of electrolytes in this concentration range significantly affects the bubble rise velocity. At low concentration range, the change in the *static* surface tension and in the bulk properties of the liquid (viscosity and density) is relatively small, therefore, a significant effect on the rise characteristics of the bubble would have to be associated with the effects of

the electrolytes on the interfacial rheology. These effects are dependent on the interaction close the gas-liquid interface (detailed in 3.B) and a better understanding would be required to explain them and to clarify whether they can have a significant effect on the rise characteristics of the bubble. At higher concentrations, however, there is a relatively large change in the *static* surface tnesion and in the bulk properties of the liquid, which, just by itself, can change significantly the rise characteristics of an ellipsoidal bubble. This change in the properties (ρ, μ, and σ) is the dominant effect and the bubble rise can be explained by currently-known clean-bubble pure-fluid correlations based entirely on the *static* surface tension and in the bulk properties of the liquid (viscosity and density).

ACKNOWLEDGEMENTS

The authors thank Bert Vreman for constructive discussions and comments on the manuscript. The authors also acknowledge additional financial support from the Nouryon PPC business unit and the industrial traineeship for MMM at Bohus, Sweden.

APPENDICES

3.A. PROPERTIES OF LIQUIDS

Table 3.1: Physical properties of the liquids used in the current study.

Fluid (F#)	T T, °C	ρ kg/m^3	μ Pa.s, x10^{-3}	σ mN/m	Mo $\mu^4 g/\rho\sigma^3$
F1	25	996	0.89	71.5	1.76 x 10^{-11}
	40	992	0.65	70.1	5.21 x 10^{-12}
Water	60	983	0.46	66.6	1.59 x 10^{-12}
	80	972	0.36	61.5	6.82 x 10^{-13}
F2	25	1085	1.13	75.9	3.48 x 10^{-11}
	40	1076	0.83	73.7	1.08 x 10^{-11}
2 M NaCl	60	1064	0.59	70.5	3.21 x 10^{-12}
	80	1053	0.45	66.5	1.36 x 10^{-12}
F3	25	1229	1.55	86.2	7.24 x 10^{-11}
	40	1220	1.13	82.3	2.38 x 10^{-11}
4.5 M NaCl	60	1209	0.81	77.2	7.55 x 10^{-12}
	80	1196	0.62	72.1	3.32 x 10^{-12}
F4	25	1091	1.21	85.0	3.17 x 10^{-11}
20% mix.	40	1082	0.91	81.2	1.16 x 10^{-11}
(0.94 M $NaClO_3$	60	1071	0.77	76.1	7.32 x 10^{-12}
+ 0.34 M NaCl)	80	1063	0.46	70.9	1.16 x 10^{-12}
F5	25	1157	1.36	87.2	4.44 x 10^{-11}
40% mix.	40	1148	1.09	83.3	2.08 x 10^{-11}
(1.88 M $NaClO_3$	60	1136	0.81	78.2	7.76 x 10^{-12}
+ 0.68 M NaCl)	80	1125	0.59	73.1	2.71 x 10^{-12}
F6	25	1192	1.56	92.1	6.32 x 10^{-11}
60% mix.	40	1166	1.21	87.4	2.69 x 10^{-11}
(2.81 M $NaClO_3$	60	1148	0.92	81.2	1.14 x 10^{-11}
+ 1.02 M NaCl)	80	1135	0.67	75.1	4.11 x 10^{-12}
F7	25	1367	3.46	101.1	1.01 x 10^{-9}
100% mix.	40	1358	2.27	94.3	2.28 x 10^{-10}

(4.69 M $NaClO_3$ + 1.71 M NaCl)	60 80	1346 1304	1.46 0.96	85.5 78.6	5.15×10^{-11} 1.31×10^{-11}

Symbols: T - Temperature, ρ - Density, μ- Viscosity, σ- Surface tension, *Mo* - Morton number.

3.B. ION EFFECTS AND RHEOLOGY OF THE GAS-LIQUID INTERFACE

The presence of surface active ions/molecules at a gas-liquid interface can introduce additional rheological behaviour at the interface, affecting the interfacial tension gradient, and the viscous and elastic nature of the interface. The resultant effect on the interfacial rheology is dependent on the chemical nature and concentration of the species, their surface distribution and their transport kinetics between the interface and the bulk liquid. For the case of electrolytes, this appendix is intended to provide a literature understanding of the ion behaviour at the interface, its possible implications for the interfacial rheology, and, therby, on the motion of a freely rising bubble.

INTERFACIAL ION MOBILITY AND STATIC SURFACE TENSION

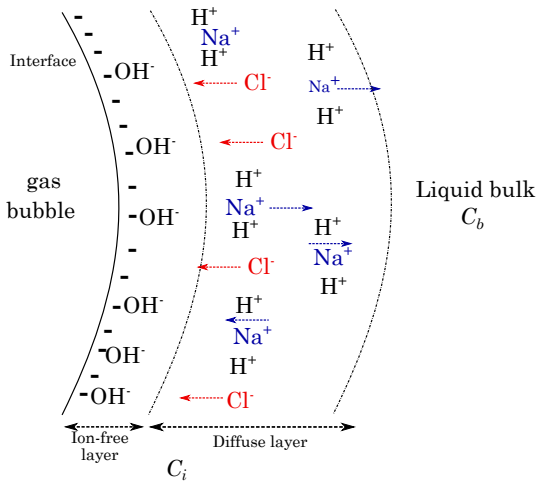

Figure 3.9: Schematic of ion distribution around gas-liquid interface in NaCl solution. Interfacial depths are in the range of 10-100 Å.

The gas-liquid interface in pure water has a slight negative charge, as the OH^- ions are attracted to the surface, forming a dielectric layer [35]. In electrolyte solutions, the behaviour of individual ions, including H^+ and OH^-, is dependent on its ionic size and charge. Electrostatic forces between the ions ultimately dictate the ion mobility and their distribution along the interface.

In an electrical double layer model, the distribution of charged species is known to occur within two layers close to the interface: ion-free layer and diffuse layer [36]. For

the case of NaCl solution, both Na^+ and Cl^- ions would prefer to stay away from the interface; their interaction with H^+ and OH^- ions in the bulk are energetically more favorable [37]. H^+ and OH^- are small ions and interfere with the transport process of other ions. Na^+ ions are small in size and hydrated by the water molecules surrounding it, as ion-dipole interaction is stronger than ion-ion one. Larger Cl^- ions are slightly polarizable and move towards the interface, however, face a strong repulsive force from the negatively charged interface, leading to an ion-free layer close to the interface. The potential at the interface, also called zeta potential, is dependent on the bulk ion concentration C_b. At bulk ion concentrations $C_b > \mathcal{O}(0.1M)$, increasing Na^+ ions can no longer be hydrated by H^+, leading them to move towards the interface. The net result is a reduction in the zeta potential [38].

The electrolyte ions are distributed in the diffuse layer, their interactions leads to a force imbalance between the bulk and the interface. A resultant change in the surface tension (σ) can be described, based on Gibbs adsorption isotherm, as:

$$d\sigma = -\Gamma_+ d\mu_+ - \Gamma_- d\mu_- \quad ; \quad \Gamma_\pm = -\frac{1}{RT}\left(\frac{\partial\sigma}{\partial ln C_b}\right)_T \tag{3.15}$$

Here, $\mu_\pm$ (not to be confused with the liquid viscosity) are the chemical potentials of the cations and anions, and $\Gamma_\pm$ are the excess corresponding ions, per unit area of the interface, at a given temperature T. For both NaCl and $NaClO_3$, similar to most well-known electrolytes, there is an increase in the surface tension when compared to pure water; this increase varies linearly with the bulk concentration [39]. A higher $d\sigma/dc$ for NaCl (=1.76 mN m^{-1} M^{-1}), when compared to $NaClO_3$ (=0.72 mN m^{-1} M^{-1}), can be attributed to a higher polarizability of a larger chlorate ion, and as a consequence, a lower electrostatic repulsion. In the electrolyte mixture, besides the ion-specific effects, chloride-chlorate ion-interaction would also play a role in determining the net ion distribution at the interfacial sublayers.

ION EFFECTS ON INTERFACIAL RHEOLOGY

A general understanding for all contaminants (salt, surfactants, mineral acids, etc.) is based on the Marangoni effect: due to non-uniform distribution of contaminants at the interface and adsorption/desorption transport processes occurring between the interface and bulk, the tangential stress along the bubble surface retards the bubble motion [40]. A possible consequence of contaminant addition is a change in the hydrodynamic boundary condition at the gas-liquid interface: from mobile to immobile. Depending on the contaminant concentration and bulk-interface transport kinetics, surface visco-elasticity and shear viscosity can be influenced [41].

While Marangoni and other rheological effects are well-known for surfactant solutions, the same mechanism may not be applicable for electrolyte solutions. At low concentrations (up to 0.2M), a change in hydrodynamic condition was not observed for smaller bubbles (< 1 mm): the terminal rise velocity was found to be agree with the mobile case [42]. Using surface visco-elasticity measurements, Safouane and Langevin [28] ruled out a change in the slip-condition at the interface up to 5M electrolyte concentration. Similarly, no influence on the dynamic surface tension of the gas-liquid interface was observed due to electrolyte addition up to 5.5M concentration, according to Hauner *et al.* [29], who mention the rapid timescale of ion-mobility (< 1 ms) as a possi-

ble explanation. Fast kinetics, indeed, minimizes the interfacial tension gradient along the gas-liquid interface [43]. These literature studies suggest that electrolytes have no significant on interfacial rheology.

It is important to note that other widely studied application cases with electrolytes draw a different conclusion. Increased surface viscosity and, thereby, reduced surface mobility at higher ion concentrations has been cited as a reason for: slow drainage of saline thin films and inhibition of bubble coalescence [44], and stabilization of surfactant-laden foam films due to electrolyte addition [e.g. 45, 46]. However, such a conclusion cannot be extrapolated for the case of a freely rising bubble, as confinement effects in thin films ($\mathcal{O}$(100 nm)) and the presence of surfactant molecules can have a strong influence on the electrolyte ion distribution and mobility.

While an increasing electrolyte addition has an impact on the ion interaction and mobility close to the interface, current literature suggests that this merely leads to an increase in the *static* interfacial tension and has no/limited influence on the dynamic rheological properties of the interface.

3.C. SURFACE TENSION MEASUREMENT

While there are many ways to measure the surface tension measurement of liquids (e.g. bubble pressure method, Wilhelmy plate), at higher temperatures there are strong limitations to these traditional methods. As the liquid needs to be heated and maintained at a higher temperature, any gradient can strongly influence the accuracy. Hence, an imaging-based technique is used for the current study. In a pendant bubble method, as shown in Figure 3.10a, a hydrogen bubble is generated and stabilized at the tip of a J-shape needle (0.45 mm inner diameter), surrounded by the liquid of interest in an elongated cuvette (LxDxH = 10 mm x 100 mm x 50 mm). Bubble images are captured using a high-speed camera (Basler Aca-1920-150uc) attached with 75 mm macro-lens. The bubble shape is the result reflective of the competing gravity and capillary forces. These images are inverted and subsequently analysed with Pendant drop analysis plugin [47], in FIJI software. Temperature is controlled using a laboratory electric heater. Temperature gradient is observed to be small ($\leq 0.5^{\circ}$C), as the cuvette is relatively small in size.

Results from the measurements (Figure 3.10b) show an expected surface tension decrease with temperature and an increase with the addition of electrolyte. The imaging technique is quite reliable, with a maximum deviation of 0.5 mN/m, and the results for water and 2M NaCl agree with known literature data [21, 48].

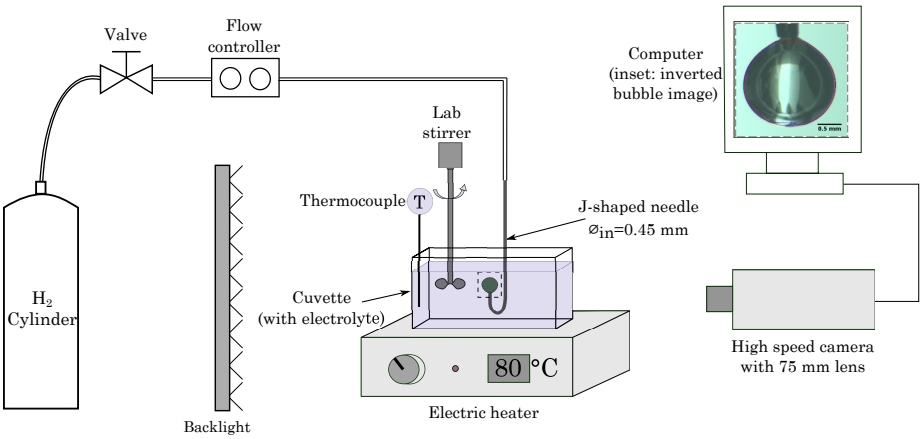

(a)

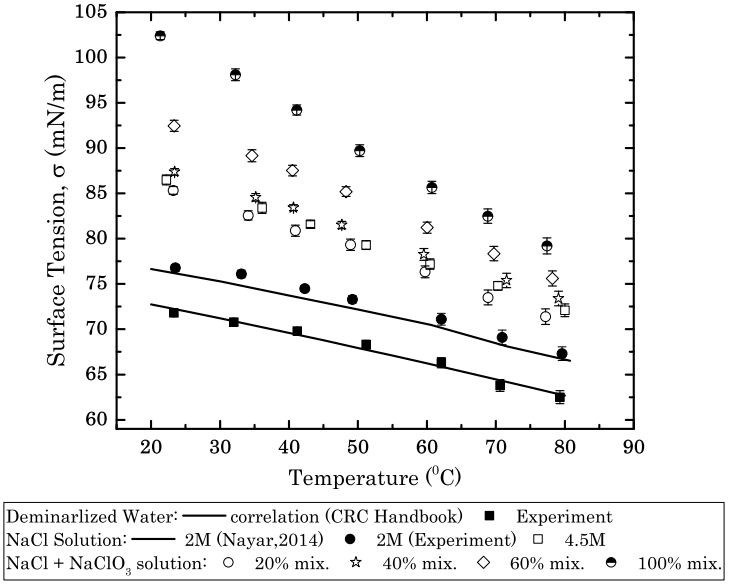

(b)

Figure 3.10: Measurement of liquid surface tension: (a) schematic of the setup with (inset) typical image of the bubble (inverted); (b) results for all liquids used in the current study.

REFERENCES

[1] M. M. Mandalahalli, J. Lif, R. F. Mudde, and L. M. Portela, *Electrolyte and temperature effects in a rising bubble,* Chemical Engineering Science **270**, 118276 (2023).

[2] W. Liu, C. Moran, and S. Vink, *A review of the effect of water quality on flotation,* Minerals Engineering **53**, 91 (2013).

[3] D. Jean and D. Lee, *Effects of salinity on expression dewatering of waste activated*

sludge, Journal of colloid and interface science **215**, 443 (1999).

[4] P. Rollbusch, M. Bothe, M. Becker, M. Ludwig, M. Grünewald, M. Schlüter, and R. Franke, *Bubble columns operated under industrially relevant conditions – current understanding of design parameters,* Chemical Engineering Science **126**, 660 (2015).

[5] A. A. Kulkarni and J. B. Joshi, *Bubble formation and bubble rise velocity in gas- liquid systems: a review,* Industrial & Engineering Chemistry Research **44**, 5873 (2005).

[6] M. K. Tripathi, K. C. Sahu, and R. Govindarajan, *Dynamics of an initially spherical bubble rising in quiescent liquid,* Nature Communications **6**, 6268 (2015).

[7] D. Moore, *The boundary layer on a spherical gas bubble,* Journal of Fluid Mechanics **16**, 161 (1963).

[8] R. Clift, J. Grace, and M. Weber, *Bubbles, Drops and Particles* (New York: Academic Press, 1978).

[9] D. Legendre, R. Zenit, and J. R. Velez-Cordero, *On the deformation of gas bubbles in liquids,* Physics of Fluids **24**, 043303 (2012).

[10] D. W. Moore, *The velocity of rise of distorted gas bubbles in a liquid of small viscosity,* Journal of Fluid Mechanics **23**, 749 (1965).

[11] R. B. Fdhila and P. C. Duineveld, *The effect of surfactant on the rise of a spherical bubble at high reynolds and peclet numbers,* Physics of Fluids **8**, 310 (1996).

[12] F. Peters and C. Els, *An experimental study on slow and fast bubbles in tap water,* Chemical Engineering Science **82**, 194 (2012).

[13] W. Kracht and J. Finch, *Effect of frother on initial bubble shape and velocity,* International Journal of Mineral Processing **94**, 115 (2010).

[14] J. Quinn, M. Maldonado, C. Gomez, and J. Finch, *Experimental study on the shape-velocity relationship of an ellipsoidal bubble in inorganic salt solutions,* Minerals Engineering **55**, 5 (2014).

[15] H. Hessenkemper, T. Ziegenhein, and D. Lucas, *Contamination effects on the lift force of ellipsoidal air bubbles rising in saline water solutions,* Chemical Engineering Journal **386**, 121589 (2020).

[16] Y. Zhang, A. Sam, and J. Finch, *Temperature effect on single bubble velocity profile in water and surfactant solution,* Colloids and Surfaces A: Physicochemical and Engineering Aspects **223**, 45 (2003).

[17] I. Leifer, R. K. Patro, and P. Bowyer, *A study on the temperature variation of rise velocity for large clean bubbles,* Journal of Atmospheric and Oceanic Technology **17**, 1392 (2000).

[18] T. Okawa, T. Tanaka, I. Kataoka, and M. Mori, *Temperature effect on single bubble rise characteristics in stagnant distilled water,* International Journal of Heat and Mass Transfer **46**, 903 (2003).

[19] S. M. Saad and A. W. Neumann, *Axisymmetric drop shape analysis (ADSA): An outline,* Advances in Colloid and Interface Science **238**, 62 (2016).

[20] R. Cygan, *The solubility of gases in NaCl brine and a critical evaluation of available data* (Sandia National Laboratories Albuquerque, 1991).

[21] W. M. Haynes, *CRC handbook of chemistry and physics: a ready-reference book of chemical and physical data* (Boca Raton : CRC Press, 2009).

[22] J. Schindelin, I. Arganda-Carreras, E. Frise, V. Kaynig, M. Longair, T. Pietzsch, S. Preibisch, C. Rueden, S. Saalfeld, B. Schmid, J.-Y. Tinevez, D. J. White, V. Hartenstein, K. Eliceiri, P. Tomancak, and A. Cardona, *Fiji: an open-source platform for biological-image analysis,* Nature Methods **9**, 676 (2012).

[23] A. Tomiyama, G. Celata, S. Hosokawa, and S. Yoshida, *Terminal velocity of single bubbles in surface tension force dominant regime,* International Journal of Multiphase Flow **28**, 1497 (2002).

[24] M. Rastello, J.-L. Marie, and M. Lance, *Drag and lift forces on clean spherical and ellipsoidal bubbles in a solid-body rotating flow,* Journal of Fluid Mechanics **682**, 434459 (2011).

[25] P. C. Duineveld, *The rise velocity and shape of bubbles in pure water at high reynolds number,* Journal of Fluid Mechanics **292**, 325 (1995).

[26] I. S. Kang and L. G. Leal, *The drag coefficient for a spherical bubble in a uniform streaming flow,* The Physics of Fluids **31**, 233 (1988).

[27] E. Loth, *Quasi-steady shape and drag of deformable bubbles and drops,* International Journal of Multiphase Flow **34**, 523 (2008).

[28] M. Safouane and D. Langevin, *Surface viscoelasticity of concentrated salt solutions: Specific ion effects,* ChemPhysChem **10**, 222 (2009).

[29] I. M. Hauner, A. Deblais, J. K. Beattie, H. Kellay, and D. Bonn, *The dynamic surface tension of water,* The Journal of Physical Chemistry Letters **8**, 1599 (2017).

[30] D. Rodrigue, *A general correlation for the rise velocity of single gas bubbles,* The Canadian Journal of Chemical Engineering **82** (2004), 10.1002/cjce.5450820219.

[31] W. L. Haberman and R. Morton, *An experimental investigation of the drag and shape of air bubbles rising in various liquids* (David Taylor Model Basin Washington DC, 1953).

[32] L. Schiller, *Über die grundlegenden berechnungen bei der schwerkraftaufbereitung,* Z. Vereines Deutscher Inge. **77**, 318 (1933).

[33] D. D. Joseph, *Rise velocity of a spherical cap bubble,* Journal of Fluid Mechanics **488**, 213 (2003).

[34] M. Rastello, J.-L. Marié, and M. Lance, *Clean versus contaminated bubbles in a solid-body rotating flow,* Journal of Fluid Mechanics **831**, 592 (2017).

[35] M. Chaplin, *Theory vs experiment: What is the surface charge of water?* Water **1** (2009), 10.1.1.475.2221.

[36] P. Leroy, D. Jougnot, A. Revil, A. Lassin, and M. Azaroual, *A double layer model of the gas bubble/water interface,* Journal of Colloid and Interface Science **388**, 243 (2012).

[37] P. Jungwirth and D. J. Tobias, *Specific ion effects at the air/water interface,* Chemical Reviews **106**, 1259 (2006).

[38] C. Yang, T. Dabros, D. Li, J. Czarnecki, and J. H. Masliyah, *Measurement of the zeta potential of gas bubbles in aqueous solutions by microelectrophoresis method,* Journal of Colloid and Interface Science **243**, 128 (2001).

[39] C. L. Henry, C. N. Dalton, L. Scruton, and V. S. J. Craig, *Ion-specific coalescence of bubbles in mixed electrolyte solutions,* The Journal of Physical Chemistry C **111**, 1015 (2007).

[40] M. Ruzicka, *On dimensionless numbers,* Chemical Engineering Research and Design **86**, 835 (2008).

[41] D. Langevin, *Rheology of adsorbed surfactant monolayers at fluid surfaces,* Annual Review of Fluid Mechanics **46**, 47 (2014).

[42] C. L. Henry, L. Parkinson, J. R. Ralston, and V. S. J. Craig, *A mobile gas water interface in electrolyte solutions,* The Journal of Physical Chemistry C **112**, 15094 (2008).

[43] D. A. Edwards, H. Brenner, and D. T. Wasan, *Interfacial Transport Processes and Rheology* (Butterworth-Heinemann, 1991).

[44] P. T. Nguyen, *Stability and coalescence of bubbles in salt solutions in a bubble column and thin liquid films,* phdthesis, School of Chemical Engineering, The University of Queensland (2017).

[45] E. Jarek, P. Warszynski, and M. Krzan, *Influence of different electrolytes on bubble motion in ionic surfactants solutions,* Colloids and Surfaces A: Physicochemical and Engineering Aspects **505**, 171 (2016).

[46] Q. Xu, M. Nakajima, S. Ichikawa, N. Nakamura, P. Roy, H. Okadome, and T. Shiina, *Effects of surfactant and electrolyte concentrations on bubble formation and stabilization,* Journal of Colloid and Interface Science **332**, 208 (2009).

[47] A. Daerr and A. Mogne, *Pendent_drop: An ImageJ plugin to measure the surface tension from an image of a pendent drop,* Journal of Open Research Software **4** (2016), 10.5334/jors.97.

[48] K. G. Nayar, D. Panchanathan, G. H. McKinley, and J. H. Lienhard, *Surface tension of seawater,* Journal of Physical and Chemical Reference Data **43**, 043103 (2014).

4

DYNAMICS AND MASS TRANSFER OF A RISING BUBBLE

"All causation as we have defined it is correlation, but the converse is not necessarily true, i.e. where we find correlation we cannot always predict causation."

~ Karl Pearson, *The Grammar of Science* (1900) [1]

In this work, the rise characteristics of shrinking CO_2 and non-shrinking N_2 bubbles in demineralized water for a wide range of bubble sizes in the ellipsoidal and wobbly regime (equivalent diameter, d_{eq}, between 1.5 mm and 6.5 mm), have been investigated. For these bubbles, their size, trajectory, and rise velocity have been measured using a moving camera system, while the dissolved CO_2 is studied using a Planar Laser-induced fluorescence (P-LIF) technique. We explore the interplay between hydrodynamics and mass transfer using well-studied regimes in bubble behaviour. Our results show that the interrelation between mass transfer and bubble rise dynamics is quasi-steady in nature, and strongly dependent on wake-induced effects: shape and path oscillations. Based on the interrelation between two phenomena, we conclude that the behaviour of smaller bubbles (d_{eq} <2 mm) as immobile spheres from a mass transfer perspective is not related to the mobility of the interface, but to a lack of surface renewal of dissolved gas at the interface. Based on an analogy between momentum and mass transfer, we propose a mechanistic correlation for calculating the mass transfer coefficient k_L, in the ellipsoidal and wobbly regime, using the knowledge of the drag coefficient.

This chapter has been published as M.M. Mandalahalli, J.C.L.M. Hermans, V.O. Oppeneer, and L.M. Portela, *An experimental study of the dynamics and mass transfer of a rising bubble*, International Journal of Multiphase flow (2024) (In Press) [1].

[1] Paraphrasing the philosophy of *causation* from Scottish Empiricist David Hume's work in *A Treatise of Human Nature*(1739), towards the field of Science.

NOMENCLATURE

Greek symbols

σ	Surface tension [mN/m]
ρ_L	Liquid density [kg/m^3]
μ	Liquid viscosity [Pa.s]
χ	Bubble aspect ratio [-]
δ_{path}	path amplitude in bubble oscillation [mm]
λ	bubble size to column depth ratio [-]

Other symbols and abbreviations

Re	Reynolds number[-]
Eo	Eötvös number [-]
Mo	Morton number [-]
Sh	Sherwood number [-]
Pe	Peclet number [-]
Sc	Schmidt number [-]
St_m	Stanton number for mass transfer [-]
C_D	Drag coefficient [-]
$C_{D,osc}$	Drag Coefficient at the beginning of path oscillations [-]
$C_{D,max}$	Max. C_D, beginning of spherical-cap regime = 1.41 [-]
C_D^*	$\frac{C_D}{C_{D,osc}}$ [-]
ΔC_D^*	Normalized drag coefficient = 1- $\frac{(C_{D,\max} - C_D)}{(C_{D,\max} - C_{D,\mathrm{osc}})}$ [-]
k_L	Mass transfer coefficient [m/s]
h_u	Momentum transfer coefficient [m/s]
d_{eq}	Equivalent bubble diamter [mm]
D_L	Gas diffusivity in liquid [m^2/s]
u_b	Bubble rise velocity [m/s]
$a_{s,b}$	Surface area of the bubble [mm^2]
He	Henry constant for CO_2 in water = 1.6x10^5 [kPa]
$V_b(t)$	Volume of bubble at time at t [mm^3]
R	Universal gas constant = 8.314 [J/mol/K]
V_r	Relative liquid velocity at interface [m/s]

Subscripts

$mobile, immobile$	Nature of gas-liquid surface
I_{sheet}, I_{back}	LIF intensity with and without laser sheet
I_{calib}	Calibration image
emp	Empirical
$expt$	Experimental

4.1. INTRODUCTION

The rise of shrinking bubbles is widely found in many natural and industrial processes, such as subsea blowouts, electrolysis, fermentation, and several technologies aimed at carbon capture, utilization and sequestration (CCUS) [e.g. 2–4]. Designing gas-liquid unit operations for these processes requires a good understanding of the interactions between the two phases. This includes both hydrodynamic (bubble size and shapes, gas fraction, rise velocities) and mass transfer (coefficient k_L, concentration profiles) characteristics, and the interplay between hydrodynamics and mass transfer . While the dynamics of rising bubbles have been extensively studied, both at single bubble level [e.g. 5, 6] and in dense bubbly flow industrial cases [7], a majority of the studies are based on an air-water system. Correlations and design models derived from these studies may not be applicable, as the effects of shrinkage on the bubble hydrodynamics are not considered. A phenomenological understanding of the interplay between hydrodynamics and mass transfer, even for a single shrinking bubble, is, therefore, relevant and can aid in developing efficient design models for bubbly flow processes. In the design of bubbly flow processes, a common practice is to investigate the behaviour of a single bubble and then to apply case-dependent correction factors to account for the effect of bubble-bubble interactions [8].

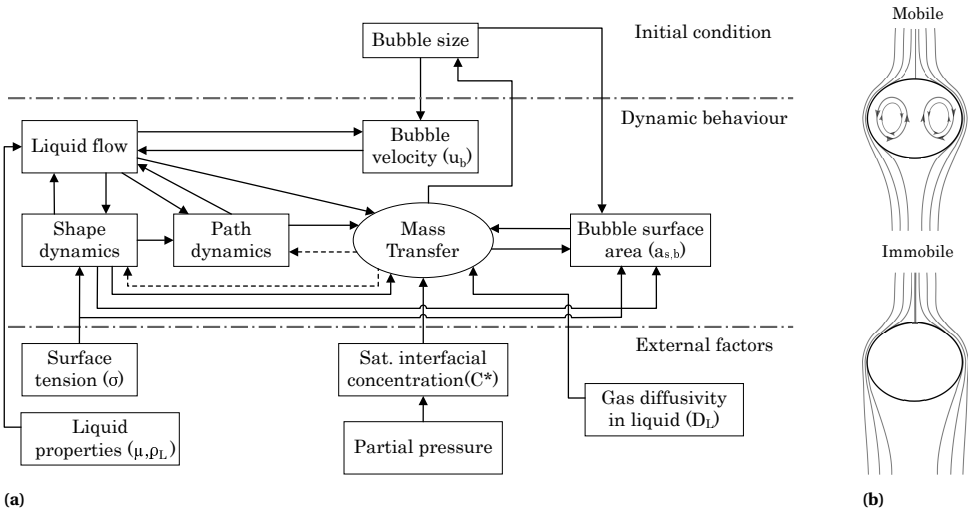

Figure 4.1: (a) Interrelations between parameters involved in gas-liquid mass transfer from a single bubble rising in a pure liquid. A dashed line (- - - - - -) indicates a weaker influence. (b) Schematic of flow around (top) mobile and (bottom) immobile interface.

Mass transfer of a rising bubble is a complex process with an interplay involving several parameters, as shown in Figure 4.1a. Bubble size playing a key role, together with the surface tension σ, and the liquid properties (density, ρ_L, and viscosity, μ), can be used to describe the rise characteristics of a non-shrinking bubble: the shape, the path, the surface area, and the rise velocity. For a variety of pure liquids, the hydrodynamic parameters have been well studied [9]. The size and shape of the bubble (spherical, ellipsoidal, wobbly, or spherical cap) dictate the surface area available for interfacial mass trans-

fer. Mass transfer, depending on the nature of the gas (diffusivity in the liquid, D_L and saturated interfacial concentration, C^*), results in a smaller bubble size, and, thereby, plays an important role in the dynamics of the bubble [10]. Changing shape and path dynamics of the bubble then affect the mass transfer, essentially, establishing a feedback loop.

In classical models, the single bubble mass transfer coefficient (k_L) has been described based on the interfacial mobility and its influence of the liquid flow around the bubble. For pure liquids, such as distilled water, with a *mobile* surface, without path and shape oscillations the flow around the bubble follows the bubble shape (Figure 4.1b(top)). Higbie's film penetration theory [11] predicts k_L based on a constant interfacial exposure time, t_e. Calderbank and Lochiel [12] suggested that this exposure time depends on the relationship between the bubble size and the slip velocity (rise velocity, u_b in the case of a stagnant liquid), with a simple expression given by:

$$k_{L,mobile} = 2\sqrt{\frac{D_L}{\pi \cdot t_e}} \quad ; \quad t_e = \frac{d_{eq}}{u_b} \tag{4.1}$$

In a contaminated liquid, even for tap water, the presence of contaminants creates a no-slip condition at the interface; the bubble behaves more like a rigid sphere (Figure 4.1b(bottom)). It is well-studied that this leads to a strong reduction in the rise velocity of the bubble [9, Figure 7.3]. Frössling [13] suggested that the effect of an *immobile* interface can be accounted for in k_L by including the kinematic viscosity of the liquid, ν, as:

$$k_{L,immobile} = 0.6\sqrt{\frac{u_b}{d_{eq}}} D_L^{2/3} \nu^{-1/6} \tag{4.2}$$

Several other well-known k_L correlations [e.g. 14, 15] have been aimed at predicting the relationship between the bubble hydrodynamics, in pure and contaminated liquids, and the mass transfer. However, a majority of these studies are limited to either small bubbles ($d_{eq} \leq 3$ mm) or large spherical cap bubbles ($d_{eq} \geq 8$ mm). With a simple Lagrangian model, Solsvik [16] showed that most known correlations do not predict the experimental mass transfer rates for a free rising CO_2 bubble in water.

A comparison with the above theoretical equations has led to a framework of classifying liquids in experimental studies as pure or contaminated. For the simple case of a shrinking CO_2 bubble rising in water, it has been observed that at smaller bubble sizes ($d_{eq} \leq 2$ mm) k_L agrees with immobile correlation and for slightly larger bubbles (2-3 mm), k_L falls within the bounds of $k_{L,mobile}$ and $k_{L,immobile}$ [17, 18]. This has been attributed to the presence of a small quantity of contaminant, even in clean water, which differentially influences smaller and bigger bubbles; observed shape oscillations in larger bubbles repel the contamination layer making them mobile. However, the classical models, used for comparing experimental results, do not include the shape and wake aspects of rising bubbles. While the concepts of path and shape oscillations are well-studied in hydrodynamics of bubbles, their implications on gas-liquid mass transfer have been poorly understood[e.g. 19, 20]. A better understanding of the hydrodynamics - mass transfer interplay is therefore of interest in describing the underlying mechanism in the rise of shrinking bubbles.

Experimentally, mass transfer of a rising bubble can be characterized both by monitoring the gas phase and/or the liquid phase: (i) tracking the rate of shrinkage of the bub-

ble; (ii) measuring the dissolved concentration field in the liquid. For measuring bubble shrinkage, two experimental approaches have been used: (i) free rising bubble in liquid [21]; (ii) bubble balanced in a counter-current downflow of liquid [17, 22]. The latter being useful for cases with slow mass transfer rates. From the liquid side, dissolved CO_2 concentration has been studied with the laser-induced fluorescence (LIF) technique, using a pH-sensitive dye [23, 24]; dissolution of CO_2 makes the liquid slightly acidic. While there are challenges to quantify the mass transfer using LIF, the technique is useful in the visualization of instantaneous mass transfer in the wake of a bubble.

In the current work, we study the rise of shrinking CO_2 bubbles and non-shrinking N_2 bubbles for a wide range of bubble sizes (equivalent diameter, d_{eq}, between 1.5 mm and 6.5 mm). A moving camera system and a planar-LIF technique have been used to study rise characteristics and gas dissolution in the bubble wake, respectively; these techniques are described in detail in a further section. This investigation is motivated towards answering key questions: (i) Does a shrinking CO_2 bubble behave hydrodynamically similarly to a non-shrinking N_2 bubble with a smaller size?; (ii) what is the role of bubble shape and wake effects on the mass transfer characteristics of ellipsoidal and wobbly bubbles ($d_{eq} > 3$ mm)?

4.2. EXPERIMENTAL METHODOLOGY

4.2.1. MOVING CAMERA SETUP TO STUDY BUBBLE DYNAMICS

The experimental apparatus is shown in Figure 1. Experiments are performed in a rectangular bubble column (W x D x H= 240 mm x 40 mm x 1000 mm), filled with demineralized water. All experiments are performed at room temperature (T=298K). The column is equipped with a needle sparger system with 98 orifices (for N_2 gas) and an isolated needle (for injection of a single N_2/CO_2 bubble). The two gases used: CO_2 ($\geq$ 99.7 vol%, grade 2.7, Linde) and N_2 ($\geq$ 99.9 vol%, grade 3.0, Linde), are supplied from separate cylinders. The flow through the needle sparger and the isolated needle is controlled independently, using two different thermal mass flow controllers (Bronkhorst B.V.), with maximum flow rates of 20 l/min and 90 ml/hr, respectively. Image acquisition is done with two USB 3.0 high-speed cameras (Basler Aca-1920 150uc), with a maximum resolution of 1920 pixel x 1200 pixel, at 112 frames/second (fps). A higher temporal resolution can be obtained by cropping the images. The first camera, attached with a 25 mm lens, is placed on a motion traverse (iselautomation) to capture the motion of a moving bubble, at 200 fps and with a 32 pixel/mm resolution. The second camera, equipped with a 75 mm lens and a 20 mm extender, is focused on the needle to capture the growth of the bubble at the needle, at 324 fps and with a 76.2 pixel/mm resolution. A white-light LED panel is placed behind the column, to provide additional light for acquisition.

To generate bubbles of different sizes from the isolated needle, six 316-stainless steel needles (I-VI) are used, with the following inner diameters: 0.2 mm, 0.7 mm, 1.0 mm, 2.2 mm, 4.0 m, and 4.5 mm. Wall effects on the bubble rise are considered negligible, as they are found to be significant for a bubble size to depth ratio ($\lambda = d_{eq}/D$) greater than 0.2 [25]; for all bubble sizes λ is found to be smaller than 0.16. For the different bubble sizes, the field-of-view of the first camera and the speed of the traverse motion are adjusted, to keep the bubble in-view, throughout its motion; bubbles of different sizes have different rise velocities. Spatial calibration is performed by taking images of a ruler

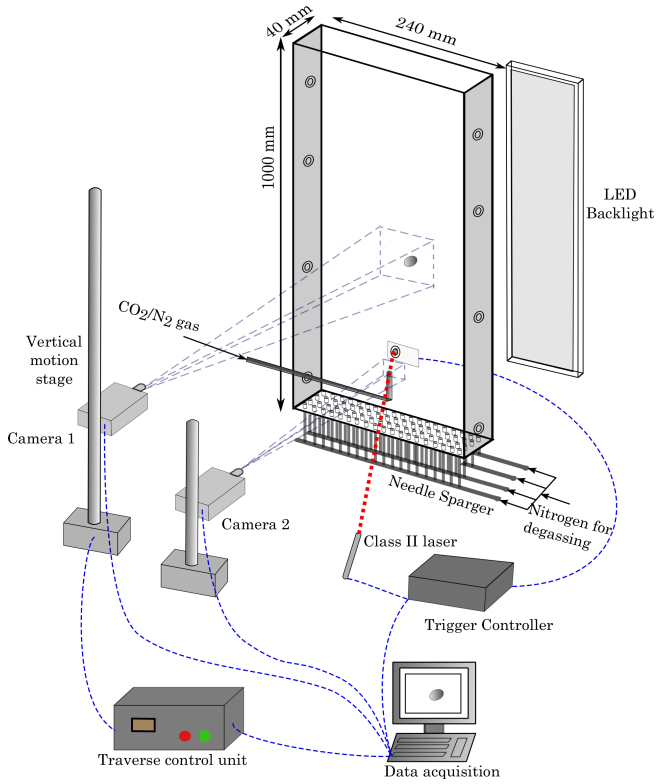

Figure 4.2: Schematic of the moving camera setup

placed in the field-of-view. The speed of the camera motion (v_{cam}) is calculated by detecting the apparent motion of markers on the ruler, using optical character recognition (OCR) in Matlab's Computer Vision Toolbox^{TM}.

Operation: Gas flow through the single needle is set at a low flow rate (10 ml/hr) to generate a single CO_2 / N_2 bubble. The second camera is used to capture the bubble during its growth at the needle, to determine its initial size when released from the needle. A laser (class II) - diode system is used to detect the bubble (based on light scattering), in order to trigger the traverse motion and the image acquisition from the first camera. The trigger system, the traverse motion, and the image acquisition are controlled using an in-house Labview code. The motion of the bubble is tracked for a height of approximately 75 cm. After each experiment with a CO_2 bubble, the column is sparged with N_2 gas for approximately 10 min, using the 98-orfice needle sparger system to remove all the dissolved CO_2. N_2 is also flushed through the single needle to avoid any residual dissolved CO_2 caused by liquid backflow. The acquired images are processed using an open-source image processing software, FIJI [26], as described below.

IMAGE ANALYSIS

Images obtained from camera 1 are analyzed to obtain bubble geometrical and motion parameters. The sequence of the image processing steps is shown in Figure 4.3. From

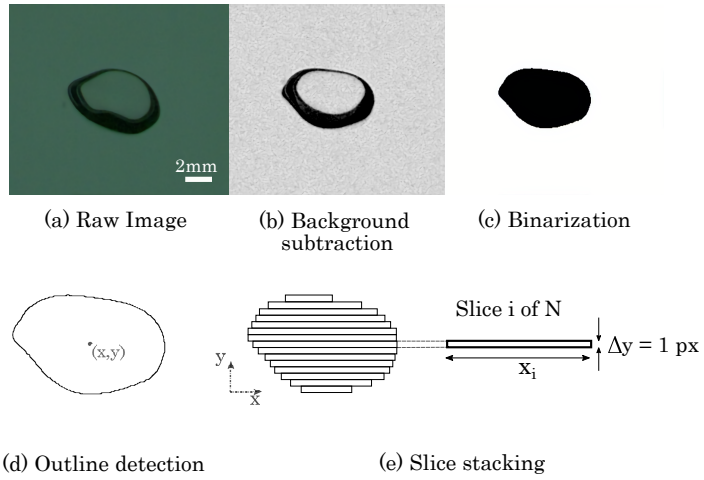

Figure 4.3: Image processing steps in FIJI software

raw images, the bubble outlines are generated using three steps: (i) background homogenization and subtraction (ii) binarization (iii) outline detection. The threshold of binarization is determined based on a method that minimizes the measures of fuzziness of the homogenized image [27]. Centroid coordinates (x,y) of the bubble, for each frame, are obtained from the outline. Considering that the bubble shapes range from ellipsoidal to wobbly, an ellipse fitting method to obtain the bubble equivalent diameter can be erroneous; a slice stacking method is therefore used. The bubble volume, V_b, the equivalent diameter, d_{eq}, and interfacial area, $a_{s,b}$, are evaluated assuming a rotational symmetry, for each slice of 1 px height, along out-of-plane axis. The mean rise velocity, u_b, is determined considering only the vertical displacement of the bubble centroid position, Δh, during the time interval, Δt, between two frames, and the velocity of the camera, v_{cam}. The corresponding equations for bubbly hydrodynamics are:

$$d_{eq} = \sqrt[3]{\frac{6V_b}{\pi}} = \left(\frac{6}{\pi} \cdot \sum_{n=1}^{N} \frac{\pi}{4} x_i^2 \Delta y\right)^{1/3}; \qquad a_{s,b} = \sum_{n=1}^{N} \pi x_i \Delta y \quad ; \qquad u_b = \frac{\Delta h}{\Delta t} + v_{cam} \tag{4.3}$$

The liquid side mass transfer coefficent, k_L, is defined using the total volume change, $V_b(t_1)$ - $V_b(t_2)$, between the two time instances, t_1 and t_2. Assuming Henry's law, an ideal gas, and a process at constant temperature T, k_L is given by:

$$k_L = \frac{1}{a_{s,b}(t)} \cdot \frac{[V_b(t_1) - V_b(t_2)] \cdot P(t)}{(t_2 - t_1) \cdot C^*(t) \cdot RT}; \qquad C^*(t) = \frac{(P(t) - P_{sat})}{He} \cdot C_v \tag{4.4}$$

Here, a reference time of $t = (t_1 + t_2)/2$ is used to calculate other time dependent parameters in the above equation. Here, $a_{s,b}(t)$ is the surface are of the bubble at t; $P(t)$ is the static pressure, given by ($P(t) = P_{\text{atm}} + \rho_L g(H_L - y(t))$, with H_L being the total height of the liquid in the column and $y(t)$ being the vertical position of the bubble at t, with respect to bottom of the column. $C^*(t)$ is the saturation concentration at the interface, determined by saturation pressure, P_{sat} (for water at T = 298K, P_{sat} = 3.171 kPa), Henry

constant, *He* (for CO_2 in water, *He* = 1.6x10^5 kPa [28]), and molar concentration of water, C_v (= 55.5 kmol/m^3). *R* is the universal gas constant (*R* = 8.314 J/mol/K).

Bubbles obtained from camera 2 are intended to calculate the initial bubble size. For each case, the last frame of the sequence with the bubble attached to the needle is chosen for postprocessing. The projection of the needle is removed by subtracting the image with a no-bubble image. Further steps to detect the bubble shape and size are similar to the ones outlined above for camera 1.

4.2.2. PLANAR LIF IMAGING OF THE BUBBLE WAKE

Planar Laser-induced-fluorescence (P-LIF) technique is used to study the dissolved CO_2 concentration in the wake of a rising bubble. The experimental setup is shown in Figure 4.4a. The setup consists of a tank, equipped with a needle holder and a sparger (used for supplying degassing N_2 gas). Single CO_2 bubbles are generated through a needle connected to the holder and controlled using a thermal mass flow controller (Bronkhorst B.V., maximum flow rate 90 ml/hr). The flow rate is maintained at 10 ml/hr. In order to produce CO_2 bubbles of different sizes, five different needles are used (needles I-V), with inner diameters: 0.2 mm, 0.7 mm, 1.0 mm, 2.2 mm, and 4.0 mm, respectively. An incident laser is generated using a high-speed laser (Litron LDY 304, 60 mJ energy/pulse with pulse width 150ns) with a peak wavelength at 527 nm. Using sheet optics (laser guiding arm and 10 mm lens), a thin laser-sheet of 1-2 mm width is focused on the column at a plane above the needle. Image acquisition is done using a high-speed camera (LaVision Imager Pro HS 4M, resolution 2016x2016 px^2at a 1278 Hz frequency) equipped with a 100 mm lens (Nikon). A high wavelength pass filter (λ_m = 540 ± 10 nm) is attached to the lens, to filter out the laser light. Images are captured with a field-of-view of 120 mm x 45 mm (resolution: 0.011 mm/pixel) and a focal depth of 60 mm ($f_\#$ = 8), in order to keep the bubble in focus during its path oscillations.

Dissolution of CO_2 in water reduces the pH, from 7.0 to approximately 3.7 (at saturation), making the solution acidic. A water-soluble dye, Sodium Flourescein (CAS number: 518-47-8), is uniformly dissolved in demineralized water. The dye is known to be light-sensitive in this pH range, emitting lower light with increasing dissolved gas concentration [29]. While other sulfo-rhodamine based dyes, such as C-SNARF (used by Kong *et al.* [30]), are more sensitive in this wavelength range, considering the cost of such tailor-made dyes and the nature of the current investigation being semi-quantitative, the choice of the dye is deemed sufficient. The concentration of Sodium Fluorescein (35 mg/L) is chosen such that the dynamic range of the camera (up to 4000 counts) is fully utilized. In order to monitor the pH in the liquid, a pH meter (MetrOhm 913 with Pt1000 electrode, sensitivity ± 0.01) is placed in the column above the field of view.

Operation: The column is maintained at a base pH of 7, by sparging N_2 gas. For planar-LIF, the following sets of images are acquired: (i) background images, I_{back} (without laser sheet and CO_2), (ii) sheet images, I_{sheet} (with laser sheet and no CO_2), (iii) experimental images during the rise of the bubble, I_{expt}, (iv) calibration images, I_{calib} = f(pH) (with laser on). Laser sheet and camera acquisition are manually triggered as the bubble is generated at the needle. Following each experiment, the column is sparged with N_2 till the base pH is reached again. Camera and laser systems are synchronized and controlled using DaVis 8.0 software (LaVision GmbH). Calibration and postprocessing of acquired images are performed in MATLAB; these steps are detailed in Appendix

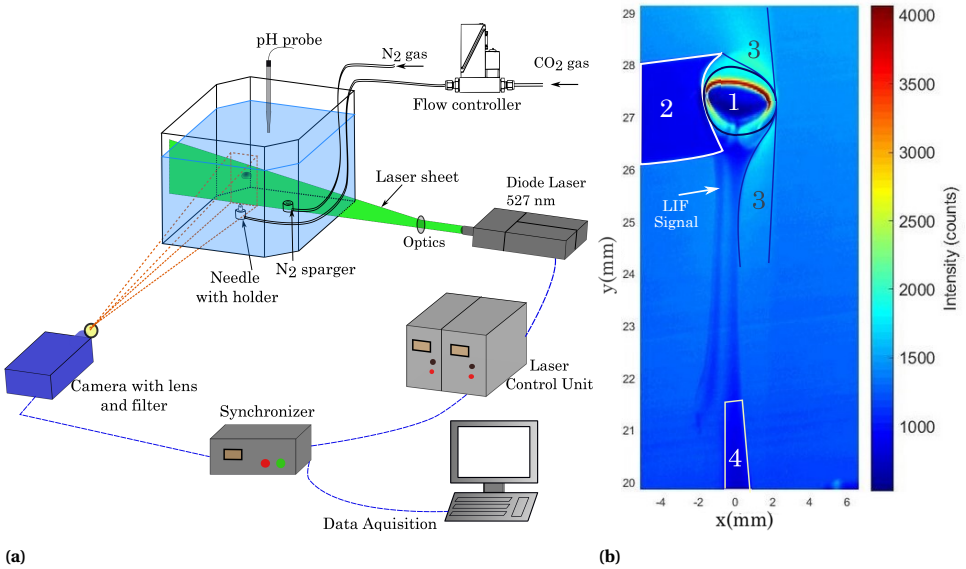

Figure 4.4: (a) Schematic of the Planar LIF setup. (b) Raw image from LIF acquisition with regions for interpretation: 1. bubble region, 2. shadow created by the bubble, 3. light cone (reflections of laser light hitting the bubble surface) and 4. region close to the needle, darker due to an accummulation of dissolved CO_2 during bubble generation.

4.A.

Experimental raw image (colour graded), as shown in Figure 4.4b, strongly reflects the challenges associated with the planar-LIF technique. Interactions of the laser sheet with the gas-liquid interface cause a shadow (region 2), light cone (region 3), and multiple reflections on the bubble surface (region 1). These phenomena strongly interfere with the quantitative calculation of concentration around the surface and of the bubble. Similar challenges have been observed in earlier LIF investigations [30, 31]. However, as the gas concentration in the wake region is distinguishable, for the current purposes, a qualitative result is considered sufficient.

4.3. RESULTS AND DISCUSSION

4.3.1. BUBBLE HYDRODYNAMICS AND MASS TRANSFER

Bubble shapes for N_2 bubbles generated through six different needles are shown in Figure 4.5a. These bubbles can be classified in three known regimes: (i) spherical to ellipsoidal (needles I & II), (ii) slightly wobbly (needles III & IV), (iii) fully wobbly (needles V & VI). Bubble shapes can be non-dimensionally described, using a shape regime map based on three non-dimensional numbers. A *classical* shape map is the one from Clift *et al.* [9], which correlates: Reynolds number ($Re = d_{eq} u_b \rho_L / \mu$), Eotvos number ($Eo = \Delta\rho g d_{eq}^2 / \sigma$) and Morton number ($Mo = g\mu^4 / (\rho_L \sigma^3)$). A shown in Figure 4.5b, the shapes from the current experiments qualitatively agree with the shapes predicted by the Clift map for water ($Mo = 2\text{x}10^{-11}$).

For all cases, it is observed that the average initial bubble size for CO_2 is slightly

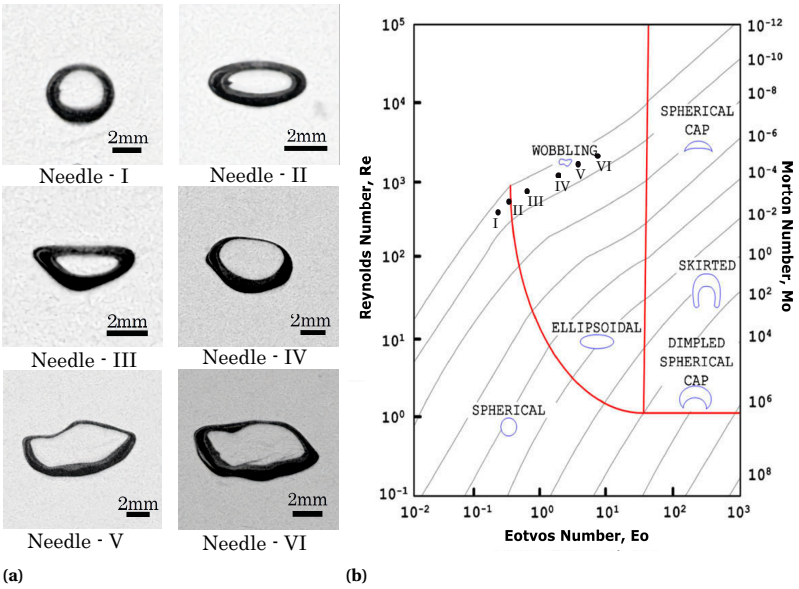

Figure 4.5: (a) Typical shapes of N_2 bubbles produced from needles I-VI. (b) Non-dimenisonal shape regime map with data from Clift *et al.* [9] (Background image reproduced from Amaya-Bower and Lee [32])

Table 4.1: Needle specifications and initial bubble size (d_i)

Needle No.	Needle inner diameter (mm)	Bubble size(mm)	
		N_2	CO_2
I	0.2	2.54	2.31
II	0.7	3.12	2.85
III	1.0	3.45	3.21
IV	2.2	4.16	3.97
V	4	5.39	5.14
VI	4.5	6.58	6.29

smaller than the corresponding N_2 bubble (Table 4.1). The initial bubble equivalent diameters from five mesaurements shows a maximum deviation of 0.05 mm. During its generation, with gas-liquid contact, a CO_2 bubble sheds mass to the surrounding liquid, leading to a different dynamics of bubble release and, consequently, a smaller bubble size. An accumulation of dissolved CO_2 is also observed in P-LIF experiments, as indicated by region 4 in Figure 4.4b. Figure 4.6 shows the evolution of the bubble equivalent diameter as a function of time. For N_2 bubbles, the equivalent diameter is found to oscillate around a constant value. This fluctuation is a consequence of the shape oscillations during the bubble rise and the method adopted for determining the bubble volume; the volume calculated from a 2D projection can lead to over/under-estimation. As the wobbly-ness of the bubble increases with size, the fluctuations also increase. CO_2 bubbles generated from needle I (Figure 4.6a) initially are ellipsoidal in shape and tends towards a spherical shape during their rise. The relative reduction in the size is larger for CO_2 bubbles in the ellipsoidal regime (Figure 4.6b, 4.6c), when compared to spherical or

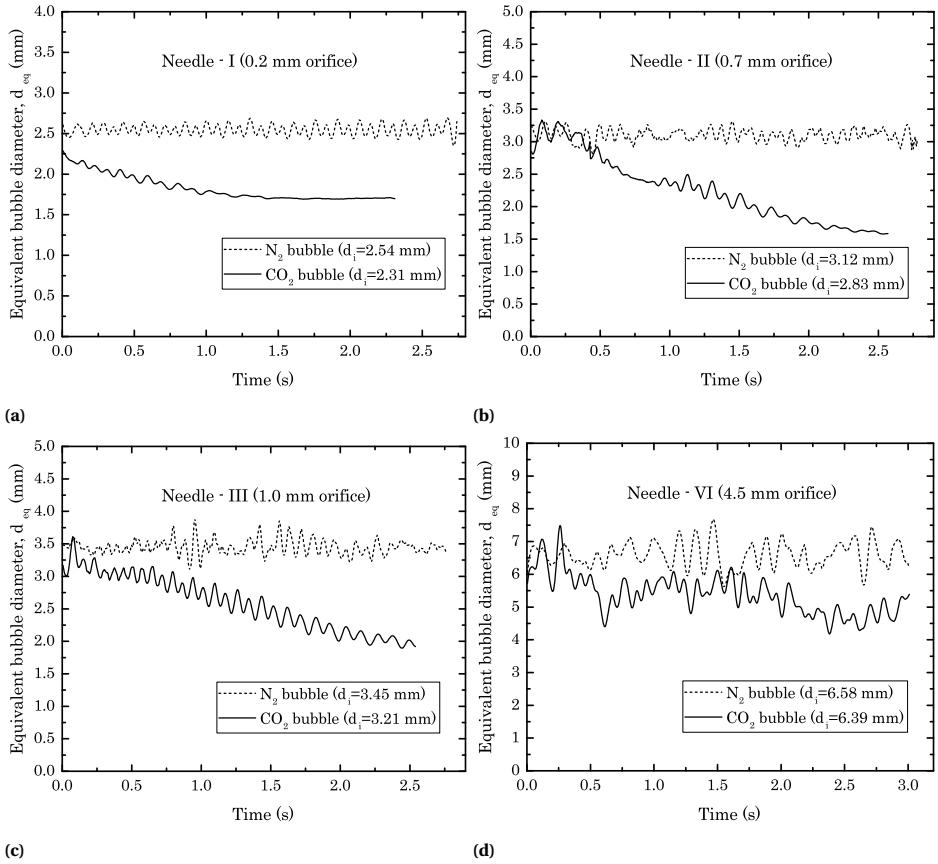

Figure 4.6: Time evolution of the bubble equivalent diameters of N_2 and CO_2 bubbles for four different needle cases: (a) Needle I (b) Needle II (c) Needle III (d) Needle IV. d_i is the intial bubble size obtained from processing images from camera 2

larger wobbly bubbles (Figure 4.6d). Bubble shape and path oscillations play a role here, as discussed further in Section 4.3.2.

The overall mass transfer coefficient, k_L, is calculated using Eqn. 4.4, with $t_1 = 0$ being the time of release from the needle and t_2 being the final time captured during the bubble trajectory. The initial and the final bubble volumes are obtained from a (non-linear) least-square fit of the time evolution of the equivalent diameter of the CO_2 bubbles. While fluctuations in size measurements have influence in determination of instantaneous bubble size and shape, this has limited effect on the overall mass transfer coefficient, as the overall shrinkage during the bubble rise is considered for the calculation.

The bubble rise velocity as a function of the equivalent diameter, both averaged over time, is compared with the empirical pure and contaminated water data from Clift *et al.* [9], as shown in Figure 4.7. N_2 and CO_2 bubbles, for all diameters studied, agree with the pure water correlation, with a CO_2 bubble behaving as a N_2 bubble with a smaller size.

This is expected, as the liquid used is dimineralized water and dissolution of a single CO_2 bubble does not change the bulk liquid properties (ρ_L, μ, σ).

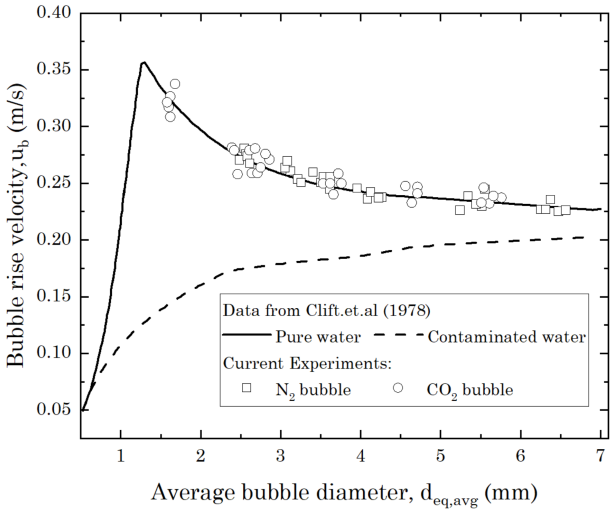

Figure 4.7: Average bubble rise velocity, u_b from current experiments, compared to the empirical data from Clift *et al.* [9, Figure 7.3] for pure and contaminated water.

The effect of shrinkage on the local bubble velocity is shown in Figure 4.8. While the velocities for N_2 bubbles have periodic fluctuations around a constant value, for the shrinking bubbles fluctuations are dampened. A CO_2 bubble speeds up during its rise. This phenomenon occurs for all experimental cases and is consistent with the findings of Clift *et al.* [9] that all smaller bubbles in the 1.5-7 mm range rise faster than the larger ones in this range.

The overall mass transfer coefficient k_L, calculated from Eqn. 4.4, for all CO_2 bubbles is shown in Figure 4.9a. The current results agree with the data from Nock *et al.* [17], who used a similar moving camera technique to study bubble rising in stagnant water. The range of data has been extended to $d_{eq}\sim$ 6 mm to include larger wobbly bubbles. Two regimes are observed in the k_L data: (i) an initial increase, as the bubble goes from a spherical regime to an ellipsoidal regime, (ii) a further relatively constant k_L, for larger bubbles in the wobbly regime. As a function of bubble size, k_L shows a different trend when compared to predictions from two well-known correlations based on interfacial mobility: Higbie (Eqn. 4.1) and Frössling (Eqn.4.2). Whereas the smaller bubbles (d_{eq} < 2 mm) agree with the prediction for an immobile surface (Eqn.4.2), larger bubbles show a deviation from both correlations.

The two correlations are based on an assumption of a constant gas-liquid exposure time (t_e) for an axisymmetric flow around a spherical bubble, coupling the bubble size and its motion to the gas-liquid interfacial area available for mass transfer (e.g. [12]). An immobile bubble leads to a flow separation at the rear of the bubble (schematized in Fig 4.1b) and, therefore, a lower relevant area for interfacial transport. For a non-spherical bubble, as is the case for larger bubbles in this study, there is a change in the velocity around the bubble, which influences the mass transfer. Besides, an increase in the

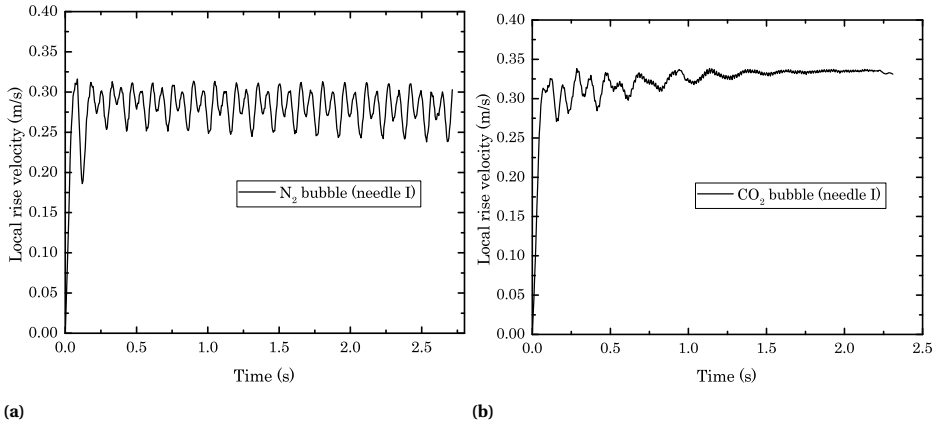

Figure 4.8: Time evolution of the local bubble rise velocity of (a) N_2 and (b) CO_2 bubbles generated from a 0.2 mm orifice (Needle I). Due to a higher velocity of the CO_2 bubble, it can be tracked for a shorter time than the N_2 one. Local fluctuations in velocity due to pixel-error in the detection of the bubble centroid is 0.003 m/s (± 1%).

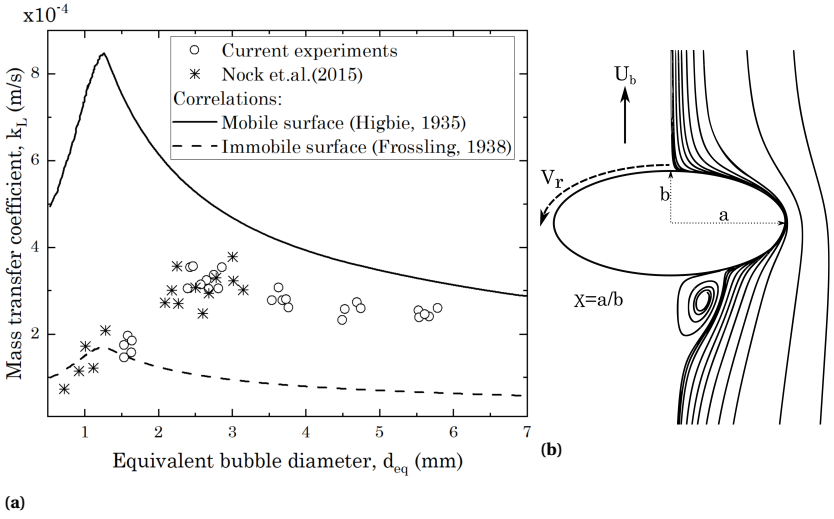

Figure 4.9: (a) Overall mass transfer coefficient (k_L) as a function of the average bubble diameter, $d_{eq,avg}$. (b) Schematic of axisymmetric flow around a mobile ellipsoidal bubble.

aspect ratio ($\chi = a/b$) increases the wake behind the bubble and the flow in this recirculation zone (schematized in Figure 4.9b) has an influence on the overall mass transfer. Studying numerical simulations of flow over fixed spheroidal bubbles ($1 \leq \chi \leq 3$), Figueroa-Espinoza and Legendre [15] showed that a change in bubble curvature leads to an increase in the vorticity generated at the bubble surface and an reduction in relative velocity (V_r) along a curved interface, when compared to Higbie's potential flow predictions. A reduced interface-bound flow and, consequently, a lower mass flux at the interface explains a theoretical overprediction of k_L by Higbie correlation for a mobile

surface. Without a good understanding of the velocity field around the bubble, the two correlations can only be considered as bounding limits for predicting k_L in the ellipsoidal regime.

Behaviour of smaller bubbles (d_{eq} < 2 mm) as *immobile* from a mass transfer perspective is particularly interesting. Previous experimental investigations [17, 18] have attributed this to a possible presence of small quantities of contaminants in the water; an oscillatory motion of larger bubbles would repel these impurities from the bubble surface, making the interface mobile. However, such an explanation is not valid in this case, as first-order hydrodynamics shows a pure-water like behaviour for all the bubbles studied (Figure 4.7); a presence of contaminants would lead to a strong reduction in the average rise velocities, which is not observed.

In order to better explain the interplay between hydrodynamics and mass transfer and the two regimes in k_L as a function of the bubble size, it is important to consider the unsteady effects (wake structure and path oscillations) of the bubble motion on the surrounding flow and its influence on mass transfer.

4.3.2. HYDRODYNAMICS - MASS TRANSFER INTERPLAY

Besides the bubble shape (as discussed in the previous section), the two k_L regimes and the deviation of experimental k_L from the theoretical predictions (Figure 4.9a) can be explained by unsteady effects during the bubble rise: wake structure and the path oscillations.

Wake effects are understood as the underlying mechanism for unsteady effects during the bubble rise, such as shape and path oscillations [33]. A transition from no-recirculation to an axisymmetric structure, and to a 3D unsteady wake, as a function of Reynolds number (Re) and bubble aspect ratio (χ), have been well-documented in phase diagrams by several numerical studies (e.g. [34, Figure 7], [15, Figure 4]).

For different CO_2 bubble sizes, instantaneous pH profiles, obtained from P-LIF measurements, are shown in Figure 4.10. Note that the CO_2 goes with 10^{-pH}, therefore, a small decrease in pH results in a large increase in dissolved concentration. The wake structure qualitatively agrees with the P-LIF results from Stöhr *et al.* [31] and Saito and Toriu [35], for bubble sizes <2 mm and 3-4 mm, respectively. Similar to bubble shapes (Figure 4.5), the bubble wake can be classified into three regimes: (i) No-recirculation structure for needles I & II, where the bubble has a thin closed-wake behind it, (ii) A non-axisymmetric wake in the case of needles III & IV generating ellipsoidal bubbles, the bubble has von Karman vortex streets in the wake, and (iii) An axisymmetric wake for large wobbly bubble from needle V; the wake has bigger swirls with much more dissolved CO_2 in them. The bubble motion in the case of a large wobbly bubble can classified as *chaotic*, as observed to be the case for bubbles in the range of large Re ($> \mathcal{O}(10^3)$) with low Mo ($< \mathcal{O}(10^{-10})$), such as water [36]. The behavior in the wake region is closely associated with the bubble shape; at larger χ, i.e., the oblateness of the bubble, an increase in curvature would induce a movement of the flow separation point closer to the bubble equator (Figure 4.9b). Large localized vorticity generated at the edge of the bubble is advected downstream accumulating in a large eddy [34]. The consequence is that most of the transfer is done on the front side of the bubble.

The unsteady nature of the wake, in the case of ellipsoidal bubbles, influence the mass transfer. Horseshoe-like vortices are indicative of a stronger liquid motion close to

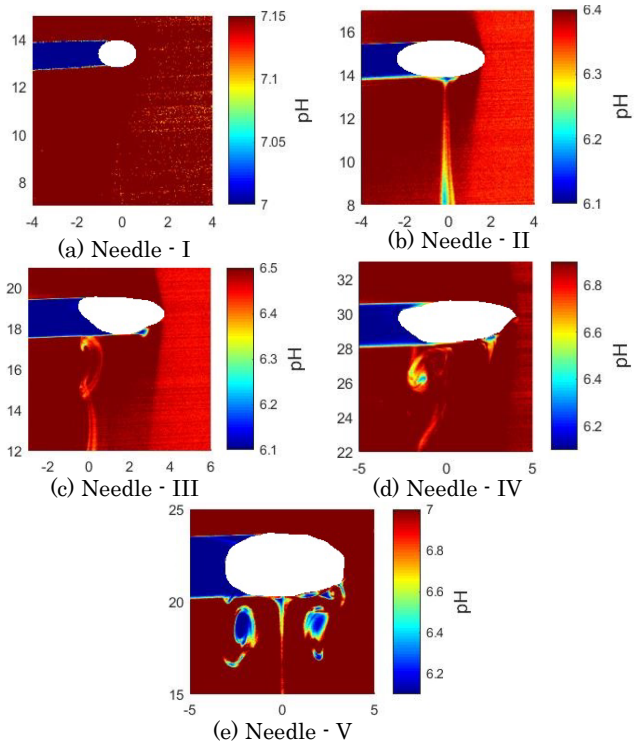

Figure 4.10: P-LIF results (a-e): pH profiles showing the CO_2 distribution in wake of bubbles generated from different needles I-V. Spatial units are in mm and the colour corresponds to the pH value. The bubble location is approximately four bubble equivalent diameters from the tip of the needle (0,0). The location of the bubble is cut out (may not be exact size), to not distract the reader by illogical values obtained due to reflections (Figure 4.4b).

the interface; convective flow enhances the transport of dissolved species away from the interface. Besides the vortex shedding, path oscillations in a zigzag regime of the bubble cause detachment of wake from the bubble, as shown in Figure 4.11. As the vortices start to grow and shed the bubble approaches a inversion point in its zig-zag path (Figure 4.11(a-d)). As bubble changes its orientation, it tends to accelerate due to a pressure differences between the two lateral extremities of the bubble [37]. This is observed in the periodic fluctuations in the bubble rise velocity (Figure 4.8a). Consequently, the vortex sheds and detaches from surface of the bubble (Figure 4.11(e-f)). Surface renewal, as a consequence of both wake shedding and detachment, enhances mass transfer, as the concentration gradient between the interface and bulk is re-established [35].

As a function of the bubble equivalent diameter, the two k_L regimes (observed in Figure 4.9a), can be explained as a difference in wake instability with increasing bubble size. Due to absence of eddies, mass transfer within the wake of a smaller bubble ($d_{eq} < 2$ mm) is dominated by diffusion and a further exchange with the surrounding liquid. An *immobile* behavior in this regime, from a mass transfer perspective (Figure 4.9a), can, therefore, be attributed to a diffusion dominated mass transfer process and a lack of surface renewal. For larger ellipsoidal bubbles ($d_{eq} > 2$ mm), two counteractive

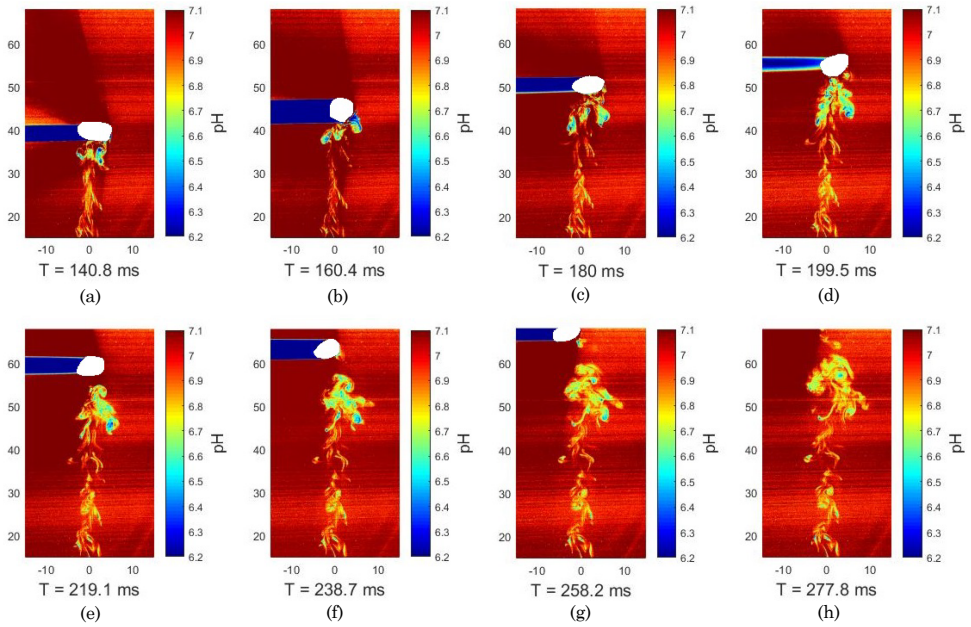

Figure 4.11: (a-h) Time evolution of the wake behind a bubble in the zig-zag regime, generated by a needle IV (with inner diameter = 2.2 mm), corresponding to a bubble size, $d_{eq} \sim 3.7$ mm. The time indicated begins at detachment of the bubble at the needle.

mechanisms are prevalent: (i) bubble shape deviating from spherical, a reduced interfacial bound flow and thereby a reduced mass transfer; (ii) wake instability and path oscillations, leading to surface renewal and enhanced mass transfer. A net effect, as can be speculated, is a deviation from both predictions, where a completely mobile or an immobile are the extreme cases. While, a difference in wake and onset of path instability explains a sharp increase in k_L (Figure 4.9a) as the shape tends to ellipsoidal, a further constant or slightly decreasing trend of k_L is a consequence of higher aspect ratio of the bubble, and, thereby, a reduced tangential flow around the bubble surface (as explained in previous section); due to a flow separation at the bubble equator, the wake region would have a limited influence on mass transfer.

Influence of mass transfer on the bubble dynamics can be understanding by the a comparison of the bubble trajectories of the shrinking and the non-shrinking bubbles. Rise trajectories (Figure 4.12) correspond to bubbles from three different needles, these indicate the path behaviour for three bubble shape regimes observed (Figure 4.5a). The x-coordinates are normalized by their corresponding equivalent diameter, to make a more accurate comparison between the path amplitudes of CO_2 and N_2 bubbles. For the smallest CO_2 bubble case (top section in Figure 4.12a (a)), there is a dampening of the oscillatory motion. This is associated with the shrinking bubble approaching the spherical shape regime from the ellipsoidal shape regime; paths are known to tend towards rectilinear as the bubble curvature tends to spherical [38]. In the ellipsoidal regime (Figure 4.12a & 4.12b), bubbles have a small rectilinear path at the beginning of their rise, followed by a zigzag regime that eventually leads to a helical motion. The path amplitude

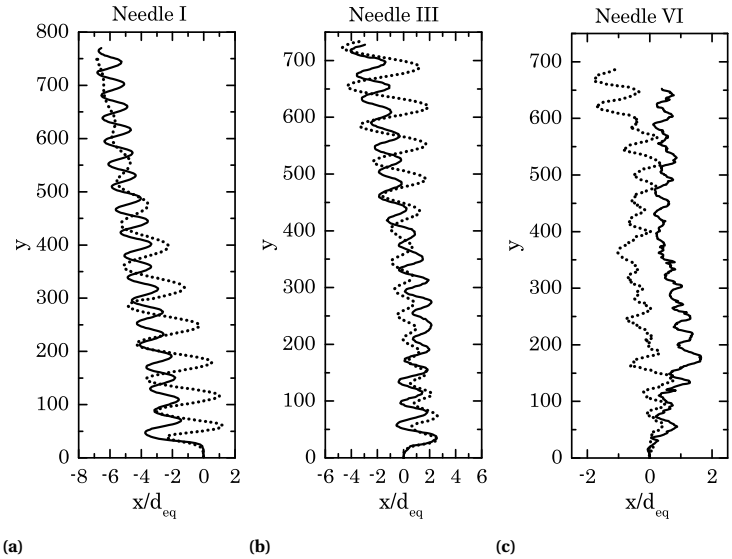

Figure 4.12: Bubble trajectories for N_2 (———) and CO_2 (·····) bubbles generated with three different needle sizes: (a) 0.2 mm Needle I (b) 1.0 mm Needle III, and (c) 4.5 mm Needle VI. Three cases chosen here are indicative of three regimes of bubble shapes. Note the relative sizing of the x- and y-axes.

is approximately 3-5 times the bubble diameter (d_{eq}). Larger wobbly bubbles (Figure 4.12c) show a chaotic path with a smaller amplitude in horizontal bubble displacement ($x/d_{eq} < 1$) compared to ellipsoidal bubbles. The transition from a zig-zag, to a flatted spiral to chaotic bubble path with increasing bubble size has been reported in earlier experimental investigations [37, 39]. An explanation for the chaotic behavior is the onset of shape oscillations [37]. Due to an increase in aspect ratio, the bubble tends to behave as a mobile bluff body; the irregular path oscillations has been explained as a consequence of coupling between bubble shape oscillations and surrounding flow [36]. Comparing the two gases, CO_2 bubbles generally show a larger path amplitude than the N_2 bubbles, specially in the ellipsoidal regime. This is a consequence of their smaller size.

A better quantitative picture can be drawn by comparing the local bubble behaviour to its local mass transfer to a corresponding bubble size, at various times during their rise. Here we define d^*_{eq}, u^*_b as the local bubble equivalent diameter and the local rise velocity, averaged over two path oscillations (schematized in Figure 4.13b), and $\delta_{\text{path}}/d^*_{eq}$ as the averaged non-dimensional path amplitude ($\delta_{\text{path}}/d^*_{eq}$). Similarly, a local mass transfer coefficient (k^*_L) is calculated based on Eqn. 4.4, accounting for the volume change over the two path amplitudes.

A function of the local bubble equivalent diameter, the path amplitude, in Figure 4.13a exhibits three regimes, characterized by the onset of path and shape oscillations. A change in bubble shape from spherical towards an ellipsoidal one, at bubble size $\approx$ 1.6 mm, coupled with a loss of axisymmetry in the wake structure, induces path instability, and is coupled with a strong horizontal motion of the bubble. Onset of shape oscillations, at $d_{eq} \sim$ 2.8 mm, through the variation in vorticity produced at bubble surface, leads to a reduction in the path amplitude. Current data, for both CO_2 and N_2 bubbles,

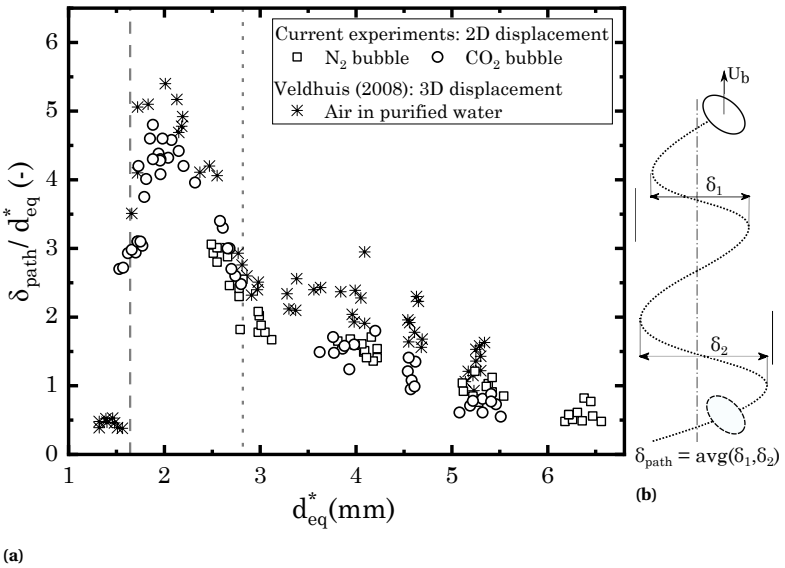

Figure 4.13: (a) Non-dimensional displacement in bubble path (δ_{path}/d^*_{eq}) for N_2 and CO_2 bubbles in helical regime. The two vertical lines indicate the onset of path (left: - - - - - -) and shape oscillations (right: ·····). Note that the data from Veldhuis [40], based on 3D visualization, is the maximum horizontal displacement obtained from the reconstructed top-view. (b) Schematic of the bubble path.

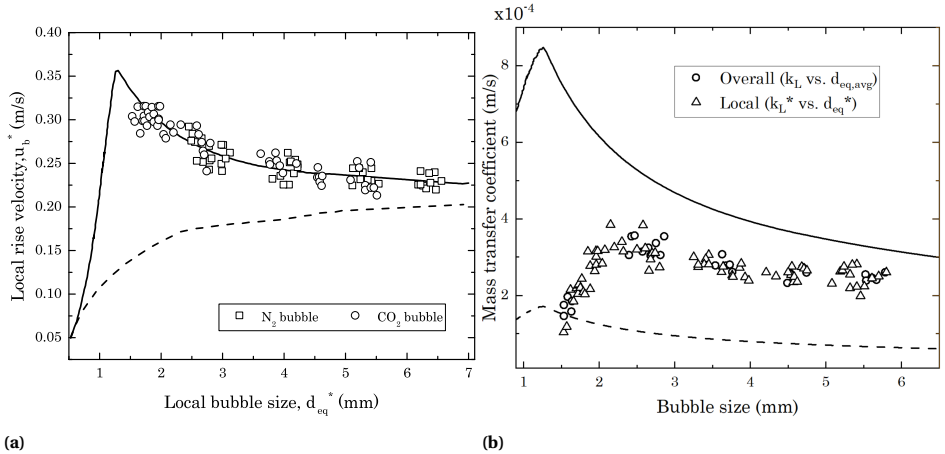

Figure 4.14: Local bubble data: (a) Local rise velocity of N_2 and CO_2 bubbles. Lines (solid and dotted) denote the empirical data from Clift *et al.* [9, Figure 7.3], similar to Figure 4.7. (b) Comparison of local (k_L) and overall mass transfer coefficients (k_L*). Lines (solid and dotted) denote the theoretical k_L predictions. Note here that the local data is an average of measurements over two oscillatory periods of bubble during its rise, as shown in the trajectory data

agrees with the literature data from Veldhuis [40]. A consistent under-prediction can be attributed to a difference in the acquisition method of bubble trajectory data; path displacement data from 2D projection (current experiments) can only be smaller or equal

to the 3D displacement of the bubble (used by Veldhuis [40]).

Local rise velocities of all bubbles, as a function of bubble size, show an expected agreement with the pure-water empirical data (Figure 4.14a), similar to the observation with average rise velocity (Figure 4.7). A comparison of the local and overall mass transfer coefficients (Figure 4.14b) clearly shows a presence of two k_L regimes, as explained earlier. A similarity in behaviour of equally-sized shrinking CO_2 and non-shrinking N_2 bubbles, in their rise velocities and bubble trajectory, shows an intrinsic dependence of their local behaviour to the bubble shape and the corresponding regime as a function of the bubble size. This strongly indicates a quasi-steady influence of mass transfer on the hydrodynamics of the bubbles; irrespective of the history effects during the bubble rise, the local bubble motion is dependent only on the bubble shape and the bubble size.

4.4. ANALOGY - HYDRODYNAMICS AND MASS TRANSFER

The mechanism of gas-liquid mass transfer is a combination of molecular diffusion within a thin film at the interface and convective transport by the surrounding flow [41]. Correlations describing the interplay between mass transfer and bubble hydrodynamics are frequently represented using non-dimensional numbers: Sherwood ($Sh = k_L d_{eq}/D_L$) and Peclet number ($Pe = Re \cdot Sc$); here Reynolds ($Re = \rho_L U_b d_{eq}/\mu$) is indicative of the liquid flow conditions and Schmidt ($Sc = \mu/\rho_L D_L$) represents the ratio of thicknesses of the flow boundary layer to the concentration boundary layer.

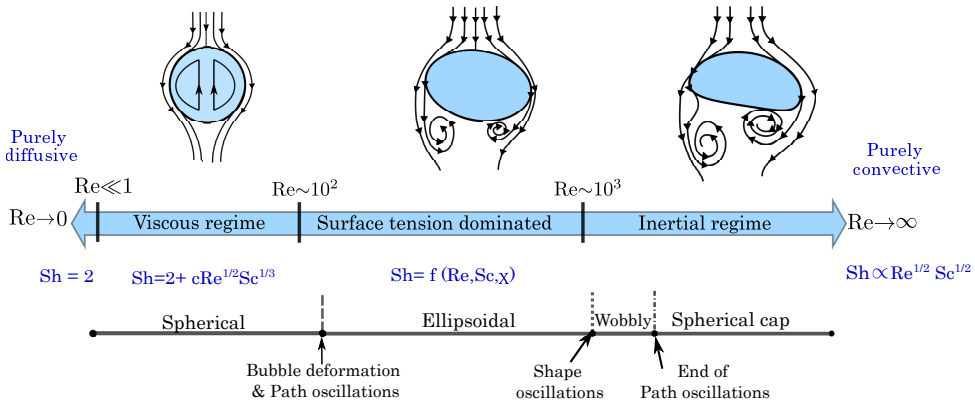

Figure 4.15: Different regimes in rise of single bubbles with Reynolds number (*Re*). Correlations for Sherwood number, *Sh*, are ones commonly used depending on the bubble regime.

For a single rising bubble in a quiescent liquid, the hydrodynamics (shape, trajectory, and rise velocity) vary with the bubble size regime; correspondingly, the influence on mass transfer characteristics should be considered in different regimes. Figure 4.15 depicts various three generalized regimes in bubble behaviours, as a function of Reynolds number (Re) [42]: (i) Viscous force dominate regime, with spherical bubbles ($Re \lesssim 10^2$); (ii) Surface tension dominated regime, with intermediate ellipsoidal bubbles ($10^2 \lesssim Re \lesssim 10^3$); (iii) Inertial force dominated regime, with large spherical cap bubbles and $Re \gtrsim 10^3$. At a lower limiting condition of a *creeping flow*, $Re \ll 1$, mass transfer is *purely* diffusive. Here, Sherwood number *Sh* approaches a constant. Further, up to finite Reynolds

number ($Re \lesssim \mathcal{O}(10^2)$), Frössling [13] proposed a scaling, based on behaviour of solid particles: $Sh \sim Re^{1/2}\ Sc^{1/3}$. This is found be valid for a steady-flow around a spherical bubble, in a regime dominated by viscosity of the fluid [12].

At the other limiting condition, $Re \to \infty$, the transport of mass and momentum can be considered as *purely* convective. At the limit of both large *Re* and *Pe*, while a concentration boundary layer exists, mass transfer is dominated by the convective transport flow over the bubble. Higbie's penetration theory [11] postulates a constant slip velocity at the interface, that determines a contact time for fluid elements exchanging transferred species between the boundary layer and the bulk liquid; here a scaling factor $Sh \propto Pe^{1/2}$ was proposed, based on existence of a boundary layer [43]. However, penetration theory correlation, is based on an inviscid flow assumption around a spherical bubble; in inertial regime bubbles tend to have strong surface tension effects deviating from a spherical shape leading to unsteady vortex shedding [2]. A further improvement to the penetration model was a surface-renewal model [44], where Dankwerts proposed a periodic surface renewal occuring at the interface, where fresh fluid elements replace the old ones.

For the intermediate surface tension dominated regime, a majority of the available correlations on mass transfer are empirical or semi-empirical derivatives of classical models derived from Higbie's penetration [11] and Frossling's rigid particle Frössling [13] theories. For a mobile interface within the low Reynolds number viscous regime ($Re \lesssim 10^2$), detailed numerical and experimental investigations [8, 45, 46] have proposed an additional *Re* influence, *Sh*=*f*(*Re*,*Pe*), in order to account for finite flow separation effects. For practical case of ellipsoidal bubbles rising in pure water, Re ($\gtrsim 10^2$) and Sc (>100), i.e., large *Pe*, extension to penetration theory have been developed for both single and dense bubbly flows, incorporating a shape factor (χ) in ellipsoidal bubble regime [47, 48], *Sh*=*f*(*Re*,*Pe*, χ). It is noteworthy that an assumption is made that total transfer is controlled by molecular diffusion over *only* front part of the bubble; any effect of due to the bubble wake is not explicitly taken into account.

A challenge in using the classical models is that they do not stress the non-uniform flow effects around a bubble. Experimental studies with LIF imaging (Saito and Toriu [35], Bork *et al.* [49] and earlier part of the current study) have shown that wake shedding and path oscillations in ellipsoidal regime plays a strong role in mass transfer. Further more in the case of large *Pe*, as is the case for ellipsoidal bubbles rising in pure water, Figueroa-Espinoza and Legendre [15] showed that the diffusion boundary layer ($\delta_D / d_{eq} \approx Pe^{-1/2}$) is insignificant compared to the hydrodynamic boundary layer. Here, a convective mechanism of mass transfer would be more relevant compared to a diffusive-dominated process. Using a combination of *Sh* and *Pe*, coupling mass transfer to a thin-film molecular diffusion might no longer reflect the underlying mass transfer mechanism. Based on this, a simpler non-dimensional parametrization is proposed further in this section, to elucidate the inherent correlation between convective aspects of bubble hydrodynamics and mass transfer.

All experimental cases in the current study correspond to a convection-dominated mass transfer regime. The range of non-dimensional parameters are: $Sh \in$ [75;750], $Re \in$ [450;1400], $Pe \in$ [2.3x10^5;6.2x10^5] and Sc is constant (CO_2-water system) at 457.

[2] Correlation based Higbie's penetration theory ($Sh \propto Re^{1/2} Sc^{1/2}$) is a theoretical consideration and not hitherto been found applicable for systems of gas bubbles, yet has been widely used as the basis of empirical and semi-empirical correlations for practical systems.

4.4.1. DRAG COEFFICIENT

Firstly, for hydrodynamics, drag coefficient C_D is a valuable parameter in order to describe the shape-size-velocity interrelation. Under a steady state terminal rise conditions the drag coefficient, as a balance between the buoyancy and drag forces is defined as:

$$C_{D,\text{expt}} = \frac{4}{3}\frac{d_{eq}g}{u_b^2} \tag{4.5}$$

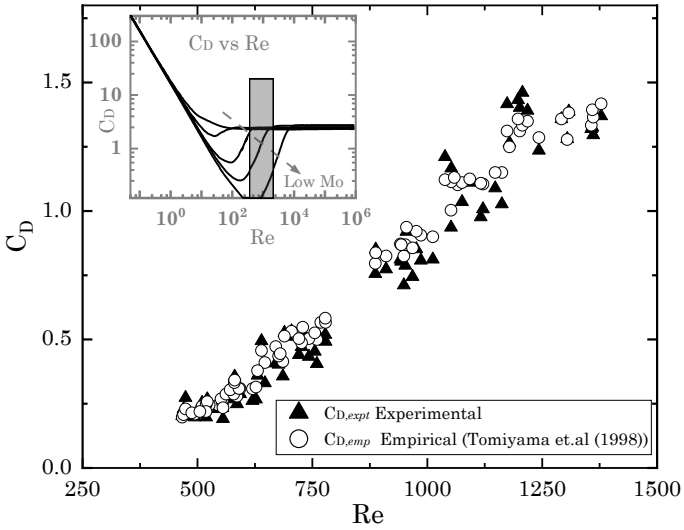

Figure 4.16: Drag coefficient C_D vs Reynolds number *Re* plot: comparison of current experimental data ($C_{D,\text{expt}}$) to predictions ($C_{D,\text{emp}}$) by Tomiyama *et al.* [50] for pure liquids. (Inset) predicted behaviour for a variety of pure liquids in the entire range of *Re*, plotted based on empirical correlation from Rodrigue [51]; gray zone depicts the range of *Re* in the current experiments. Morton number $Mo = \mu^4 g/\rho_L \sigma^3$ characterizes individual fluids; $Mo_{\text{water}} = 2\text{x}10^{-11}$

C_D can be described in terms of *Re* and one other dimensionless number. For a variety of pure fluids, characterized by Morton number ($Mo = \mu^4 g/\rho_L \sigma^3$), Rodrigue [51] derived empirical correlations, as shown in inset of Figure 4.16. For low-*Mo* fluids such as water, at moderate *Re* ($\gtrsim 10^2$), bubble shape deformation dictates deviation of C_D from its universal dependence in *Re* [52]. Further an increase in surface tension force shows an increases in the drag force on the bubble, and thereby on C_D [42], as observed for current experimental data (Figure 4.16) in the range of $Re \in [450;1400]$. For larger wobbly bubbles, C_D approaches a constant $C_{D,\max}$ for spherical-cap bubbles. A comparison with correlation for pure liquids (for all *Re* regimes) from Tomiyama *et al.* [50] (Eqn. 4.6) shows a good agreement; this is considering that the Tomiyama's correlations is based on a simple *Eo* ($Eo=\rho_L g d_{eq}^2/\sigma$) dependence for bubbles in ellipsoidal and wobbly regime.

$$C_{D,emp} = \max\left[\min\left[\frac{16}{Re}(1+0.15Re^{0.687}), \frac{48}{Re}\right], \frac{8}{3}\frac{Eo}{Eo+4}\right] \tag{4.6}$$

For different *Mo*, the transition from a $16/Re$ profile at low *Re* to a $48/Re$ at higher *Re*, passes through a similar linear C_D regime in the intermediate *Re* regime; for higher Mo values, this surface tension dependent regime is smaller.

Similar to a mass transfer coefficient, k_L, an analogous momentum transfer coefficient, h_u, can be defined, based on the drag force acting on a volume-equivalent spherical bubble, as:

$$h_u = \frac{\text{Drag force}}{\text{Area x } u_b} = C_D \cdot u_b \tag{4.7}$$

The bubble area in Eqn. 4.7 is defined based on the total surface area, based on the bubble diameter or on the cross-sectional area of the bubble. While, the drag force acts on the bubble cross-section, in order to maintain the consistency with definitions of k_L and C_D [3], the area based on sphere-equivalent bubble diameter is considered in defining h_u.

4.4.2. STANTON NUMBER

For a convection dominated mass transfer, Sherwood number *Sh*, a ratio of convective mass transfer to rate of diffusive transport, would not be a suitable parameter for non-dimensional representation of k_L. From a mass-heat transfer analogy [53], the convective interplay can be described using a Stanton number (St_m).

$$St_m = \frac{Sh}{Re \cdot Sc} = \frac{k_L}{u_b} \tag{4.8}$$

A concentration boundary layer at the bubble surface, while expected to be relative small ($(\delta_D/<d_{eq}>) \approx Pe^{-0.5} \approx 0.005$), would still influence the mass transfer flux. Schmidt number *Sc* is a constant for current work, its role needs to be verified by investigating fluids with different viscosities and diffusivities. Based on similarity of C_D profile for various fluid properties (represented by *Mo*) in Figure 4.16 (inset), it can speculated that an understanding of the interplay would also be applicable for other fluids, albeit for a different range of *Re*.

Stanton number, St_m, is plotted against C_D and d^*_{eq} in Figure 4.17; similarity in plots is anticipated, as the drag coefficient shows a linear profile with increasing bubble size in this regime. Both plots show a clear presence of two regimes in mass transfer - bubble dynamics interplay, with a transition point around $C_D = 0.34$, corresponding to a bubble size of 2.2 mm. Deviation from a linear behaviour is indicative of significant transition in drag effects on mass transfer over a short bubble size variation, whereby further deformation of bubble has negligible influence on the overall mass transfer flux across the bubble surface.

A ratio of mass to momentum transfer coefficients k_L/h_u (=St_m/C_D), as a function of drag coefficient, is plotted in Figure 4.18. Here, St_m and C_D are normalized with the respective values ($St_{m,\text{osc}}$ and $C_{D,\text{osc}}$) at the beginning of path oscillations; first data points in current study correspond to the onset of path oscillations (Figure 4.13a). The values are compared to a normalized drag coefficient ΔC^*_D (Eqn. 4.10), defined based on the $C_{D,\text{osc}}$ and the maximum value at the onset of spherical cap regime, $C_{D,\text{max}}$ =1.42. Here, the two mass transfer regimes is observed at a ΔC^*_D =0.09. An empirical correlation can be derived based on piecewise linear and exponential fit of the experimental data:

[3] It is a common practice to describe bubble characteristics: rise velocity, mass transfer coefficient and drag coefficient, in terms of bubble diameter and fluid properties, and correspondingly use the sphere-equivalent area, whilst in studies on bluff bodies, it is common to use a projected area to the flow.

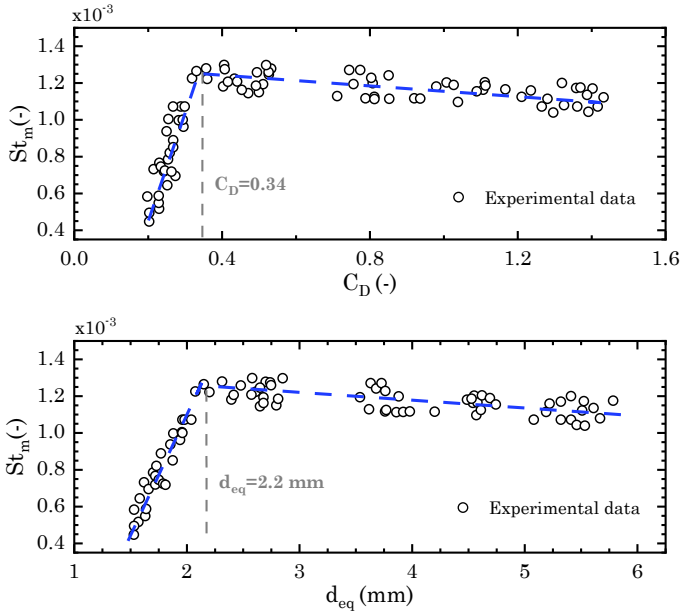

Figure 4.17: St_m as a function of the drag coefficient C_D and bubble equivalent diameter (d_{eq}). Blue lines (- - - - -) aadded to indicate different regimes (do not reflect a correlation) with transition points at C_D =0.34, corresponding to a bubble size, d_{eq} = 2.2 mm.

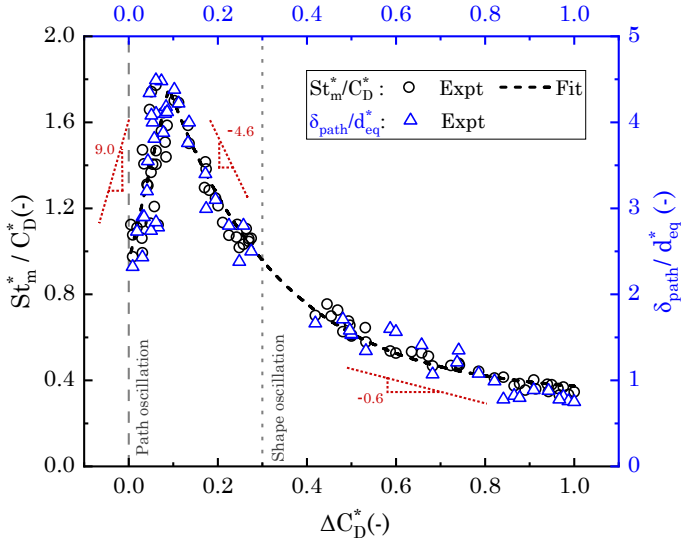

Figure 4.18: Ratio of mass transfer- momentum coefficients, k_L/h_u (represented as St_m/C_D) and Non-dimensional bubble path (δ_{path}/d_{eq}) as a function of measured drag coefficient (C_D) for CO_2 bubbles. Different measurement points correspond to local bubble data, as described earlier in Figure 4.13a.

$$\frac{St_m^*}{C_D^*} = \begin{cases} 0.95 + 9\Delta C_D^* & \text{if } \Delta C_D^* \leq 0.09 \\ 0.33 + 2.03 \cdot \exp(-\Delta C_D^*/0.25) & \text{if } 0.09 < \Delta C_D^* < 1 \end{cases} \tag{4.9}$$

Here the normalized parameters are defined as,

$$St_m^* = \frac{St_m}{St_{m,\text{osc}}} \quad ; \quad C_D^* = \frac{C_D}{C_{D,osc}} \quad ; \quad \Delta C_D^* = 1 - \frac{(C_{D,\max} - C_D)}{(C_{D,\max} - C_{D,\text{osc}})} \tag{4.10}$$

The plot of St_m^*/C_D^* shows a *strikingly* similar profile to the non-dimensional path (δ_{path}/d_{eq}^*); indicating that the mass transfer behaviour is inherently linked to the bubble path and shape dynamics. The peak of species transport efficiency (at C_D^* = 0.09 or C_D=0.34) seems to correspond with a highest path amplitude in bubble motion. A further distinction can be made between ellipsoidal and shape-oscillating wobbly bubbles due to a change in slope at $C_D^* \sim 0.3$, corresponding to the onset of shape oscillations. As shape oscillations become predominant and the shape becomes more wobbly, the profile tends towards a *plateau*. The link between bubble-wake effects and mass transfer has been discussed in the next section.

4

4.4.3. DISCUSSION: BUBBLE BEHAVIOUR AND MASS TRANSFER

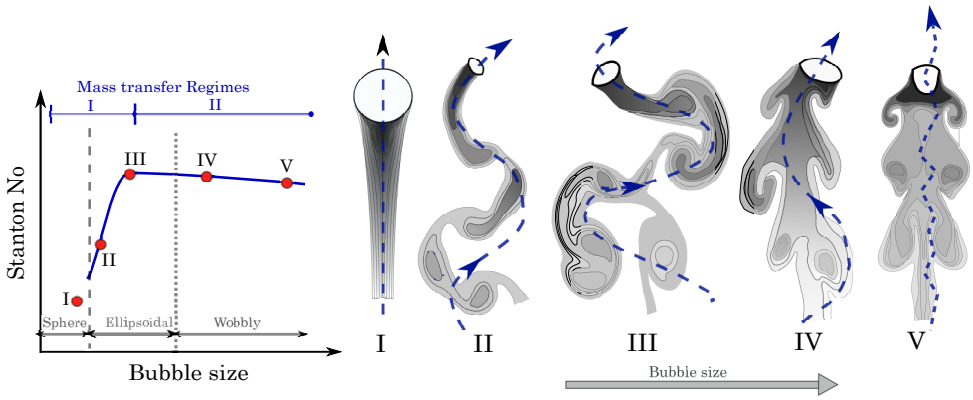

Figure 4.19: An artistic impression of the mass transfer behaviour vs bubble size and concentration distribution around bubbles for bubbles in spherical (I), ellipsoidal (II & III), slightly wobbly (IV) and fully-wobbly regime (V); Not to scale; darker region in the wake of the bubble represents higher dissolved concentration. Based on current LIF study and earlier investigations [54, 55]. Blue dashed line on I-V (- - - - -) represents the bubble trajectory. The two vertical lines on k_L - d_{eq} plot indicate the onset of path (left: - - - - -) and shape oscillations (right: ·····), as predicted by Veldhuis [40]. Spherical and spherical cap bubbles (beyond wobbly) are not investigated in current study.

An impression of the interplay, with various regimes in bubble hydrodynamics and mass transfer, is depicted in Figure 4.19. These regimes correspond to surface-tension dominated and partly into inertial regime (Figure 4.15), where bubble-wake effects play a strong role in the rise characteristics. The bubble hydrodynamics, correlating bubble rise characteristics, shapes, paths and wakes, is well described in literature [e.g. 40, 55]. The path dynamics is dependent on the bubble shape regime and inherently on the bubble size, a complex phenomenon well-studied as *Leonardo's paradox* [56]. In the entire range of bubbles: spherical to ellipsoidal to wobbly, a lower slip velocity is observed, as a consequence of an increase in the drag force on the bubble.

A slight deviation in bubble shape from spherical is sufficient to introduce an asymmetry in the wake, leading to a strong path oscillations (Bubble I to II in Figure 4.19) [34].

A higher deformation of the bubble introduces a higher path displacement in the bubble (Bubble II & III). While the net increase in drag coefficient C_D is small, the influence on mass transport is high. As the bubble follows a helical path, it undergoes acceleration at the inflection points of the trajectory [56]. An enhancement in mass transfer in this regime ($1.5 \lesssim d_{eq} \lesssim 2.5$ mm) can be attributed to this periodic change in slip conditions at the interface coupled with the interaction of vortices in the wake (with higher concentration of CO_2) with rear of the bubble. Measuring 3D-concentration profiles in the wake of 2-3mm bubbles, Saito and Toriu [35] showed an increase in local concentration, correlating to an enhanced surface renewal.

Further, a net decrease in the mass transfer within the ellipsoidal regime (Bubble III to Bubble IV) corresponds to a decrease in the path amplitude of the bubble. A reduced oscillatory behaviour could explain the extent of surface renewal at the interface, while corresponding net effect on the bubble drag is minimal. The mechanism here is the onset of the secondary effect of shape oscillations counteracting the oscillatory path. For pure water case, using Schlieren imaging technique, Veldhuis *et al.* [37] observed that the wake shedding and path oscillation frequency strongly reduced as the shape oscillations increased in the bubble size range, $d_{eq} \in$ [2.5 mm;5.3 mm]. Similarly, precise measurements of velocity field around a bubble in water (in Re range 10^2 - 10^3), reported by Dueñas *et al.* [57], showed an increase in the form-drag component of the drag coefficient, associated with wake effects, around $Re \sim 600$; this is consistent with transition point in C_D observed in current experiments. While a bubble path based local enhancement in mass transfer is observed in the wobbly regime (Figure 4.11 for $\sim$ 3.7 mm bubble), a reduced periodic acceleration could lead to a net reduced effect on mass transfer as bubble tends towards a chaotic wobbly bubble. Further transition to wobbly regime (Bubble IV & Bubble V) is associated with strong shape oscillations. Despite a net increase in the drag coefficient, the net effect on mass transfer is minimal; both St^*_m/C^*_D (and k_L as observed in Figure 4.14b) and the path amplitude reaches a *plateau*, as the bubble tends to a chaotic regime. A similar reduction in k_L was observed for wobbly CO_2 bubbles in vertical pipe flows, by Hori *et al.* [58].

In the interplay between hydrodynamics and mass transfer for ellipsoidal and wobbly bubbles, it is evident that flow effects over the bubble plays a strong role. Correspondingly, convective aspect of mass transfer needs to be considered in order to elucidate the different mechanisms within the surface tension dominated regime (ellipsoidal and wobbly bubbles). Here, we propose a mechanistic perspective towards the interplay between bubble behaviour and mass transfer, not considered in the classical mass transfer theories. While the purpose of current investigation is not to develop generalized correlation, a simplified expression (Eqn. 4.9) shows a significance of well-studied hydrodynamic parameter, C_D, in the describing mass transfer. Such correlations are valuable in extending the current knowledge on spherical bubbles towards larger ellipsoidal and wobbly bubbly, as many industrial processes operate in this regime. For a variety of pure fluids and working conditions (pressure & temperature), empirical models [51, 59, 60] are available to determine drag coefficients. While only pure water was studied in current study, based on a similarity of different pure fluids in terms of drag behaviour (as seen in inset of Figure 4.16), it can be speculated that a similar analogy based correlation is applicable for interplay between hydrodynamics and mass transfer for fluids with different viscosities.

4.5. CONCLUSIONS

In the present study, mass transfer of shrinking bubbles CO_2 and non-shrinking N_2 bubbles, for a range of equivalent diameters, d_{eq} = 1.5 mm to 6.5 mm, has been studied. For shapes of bubbles ranging from ellipsoidal, to slightly wobbly, and to strongly wobbly, it is evident that the interplay between mass transfer and hydrodynamics is strongly dependent on the bubble shape, wake-effects, and ultimately on the bubble size. A consequence of the differences in time scales between the two phenomena, the influence of bubble shrinkage on the bubble hydrodynamics can be characterized as *quasi-steady* in nature; behaviour of equally-sized CO_2 and N_2 bubbles is found to be similar, dependent only on the bubble shape.

The overall mass transfer coefficient, k_L, as a function of bubble size, shows a strong deviation from the classical models based on interfacial mobility. Based on further understanding of the interplay, we show that this deviation can be attributed to the flow separation along the bubble surface and its influence on the surface-renewal at the gas-liquid interface, and not on a possible *contaminant* effect on interfacial rigidity, as reported by earlier literature [17, 18]; for all experimental cases in the current study, the bubble rise shows a well-known *pure-water* behaviour.

For bubbles ranging from smaller spherical bubbles to larger spherical cap ones, different bubble rise characteristics lead to different mechanisms in mass transfer. For the ellipsoidal and wobbly regimes studied in this work, wake-effects: path and shape oscillations play a strong role. By analogy with hydrodynamics, we observe an inherent link between bubble path amplitude and ratio of mass & momentum transfer coefficients ($k_L/h_u = St_m^*/C_D$). Further, a mechanistic correlation is proposed, for calculating k_L with the knowledge of drag coefficient C_D. Using analogies can aid in pragmatically extending the vast knowledge in bubble hydrodynamics towards mass transfer.

ACKNOWLEDGEMENTS

The authors thank Evert Wagner and Christiaan Schinkel for their support with the experimental techniques.

APPENDIX

4.A. PLANAR LIF: CALIBRATION AND POSTPROCESSING

Calibration images (I_{calib}) are generated by maintaining the pH, at various values between 5 and 7, in the column. To remove light sheet inhomogeneity, each calibration image is pixel-wise normalized, dividing each pixel-value by the corresponding pixel-value from the sheet image (I_{sheet}), leading to a relative intensity image ($I_r = I_{calib}/I_{sheet}$). Each relative intensity image is spatially averaged and the average values are plotted against the corresponding pH values in a calibration plot, as shown in Figure 4.20. The calibration fitting equation is used in post-processing the experimental images.

The steps from raw image to concentration image are displayed in Figure 4.21. The relative intensity image (Figure 4.21(b)) is converted to a pH image using the calibration fitting function. The conversion from a pH image to a CO_2 concentration image (Figure 4.21(c)) is based on the equilibrium equation governing CO_2 dissolution in water (Eqn. A.1). Solving the equilibrium equations with the corresponding rate constants (obtained

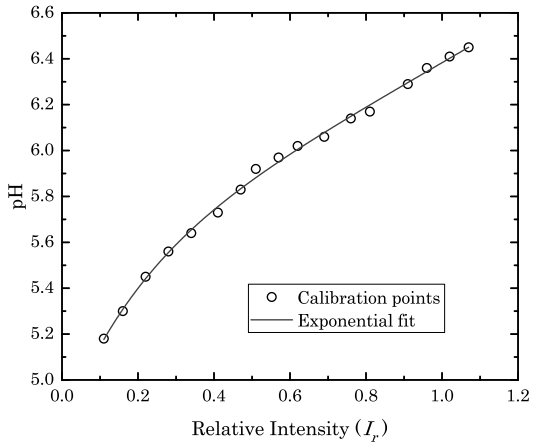

Figure 4.20: pH calibration plot: pH vs average relative intensity, I_r. The fitting function is: pH = a exp(b I_r)+ c exp(d I_r). a,b,c and d are fit constants.

from [61]), the conversion between pH and CO_2 concentration can be obtained from Eqn. A.2.

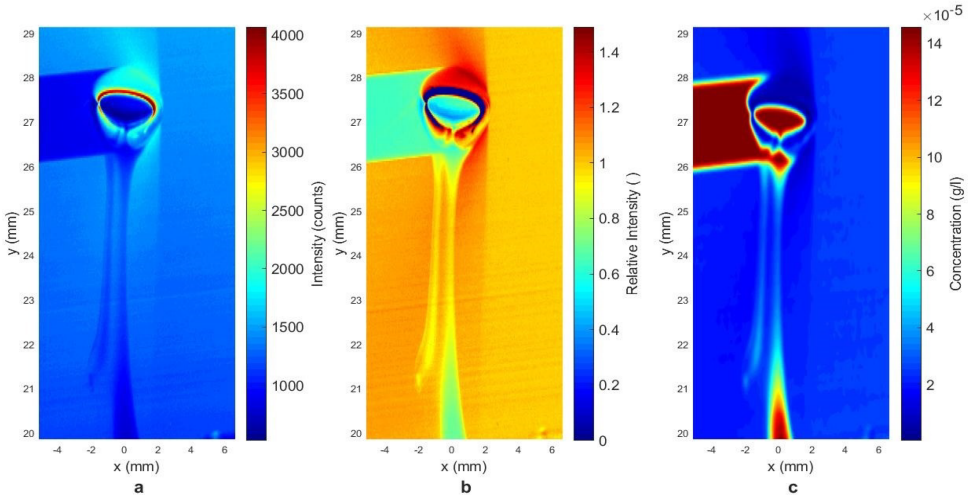

Figure 4.21: LIF processing steps: (a) Raw Image (b) Relative intensity image (c) CO_2 concentration image. Note that there is an extra step between (b) and (c), going from relative intensity to pH.

$$
\begin{aligned}
CO_2(g) &\overset{k_H}{\rightleftharpoons} CO_2(aq); \qquad k_H = 8.3\text{x}10^{-1} \\
CO_2 + H_2O &\overset{K_h}{\rightleftharpoons} H_2CO_3; \qquad K_h = 1.2\text{x}10^{-3} \\
H_2CO_3 &\overset{K_a}{\rightleftharpoons} HCO_3^- + H^+; \qquad K_a = 2.5\text{x}10^{-4} \\
K_W &= [OH^-][H^+] = 10^{-14}
\end{aligned}
\tag{4.11}
$$

$$
[CO_2] = \frac{[H^+] - K_W}{K_h K_a}; \qquad pH = -log_{10}[H^+] \tag{4.12}
$$

As seen from Figure 4.21, the conversion to a CO_2 concentration image, with a log scale, shows a small loss of detail in the wake. Hence, for current qualitative purposes, the LIF results are displayed using pH image. Note that a pH image is a H^+ concentration image, with a log scale, and that the CO_2 concentration varies linearly with the H^+ concentration.

4

REFERENCES

[1] M. M. Mandalahalli, J. C. Hermans, V. O. Oppeneer, and L. M. Portela, *An experimental study of the dynamics and mass transfer of a rising bubble,* International Journal of Multiphase Flow , 104809 (2024).

[2] H.-P. Mattila and R. Zevenhoven, *Design of a continuous process setup for precipitated calcium carbonate production from steel converter slag,* ChemSusChem **7**, 903 (2014).

[3] Y. Y. Choi, A. K. Patel, M. E. Hong, W. S. Chang, and S. J. Sim, *Microalgae bioenergy with carbon capture and storage (BECCS): An emerging sustainable bioprocess for reduced CO_2 emission and biofuel production,* Bioresource Technology Reports **7**, 100270 (2019).

[4] T. Kajishima, T. Saito, R. Nagaosa, and S. Kosugi, *GLAD: A gas-lift method for CO_2 disposal into the ocean,* Energy **22**, 257 (1997).

[5] A. A. Kulkarni and J. B. Joshi, *Bubble formation and bubble rise velocity in gas- liquid systems: a review,* Industrial & Engineering Chemistry Research **44**, 5873 (2005).

[6] M. K. Tripathi, K. C. Sahu, and R. Govindarajan, *Dynamics of an initially spherical bubble rising in quiescent liquid,* Nature Communications **6** (2015), 10.1038/ncomms7268.

[7] P. Rollbusch, M. Bothe, M. Becker, M. Ludwig, M. Grünewald, M. Schlüter, and R. Franke, *Bubble columns operated under industrially relevant conditions – current understanding of design parameters,* Chemical Engineering Science **126**, 660 (2015).

[8] A. Weiner, J. Timmermann, C. Pesci, J. Grewe, M. Hoffmann, M. Schlüter, and D. Bothe, *Experimental and numerical investigation of reactive species transport around a small rising bubble,* Chemical Engineering Science: X **1**, 100007 (2019).

[9] R. Clift, J. Grace, and M. Weber, *Bubbles, Drops and Particles* (New York: Academic Press, 1978).

[10] M. Martín, M. A. Galán, R. L. Cerro, and F. J. Montes, *Shape oscillating bubbles: hydrodynamics and mass transfer - a review,* Bubble Science, Engineering & Technology **3**, 48 (2011).

[11] R. Higbe, *The rate of absorption of a pure gas into a still liquid during short period of exposure,* Trans. Amer. Inst. Chem. Eng **31**, 365 (1935).

[12] P. Calderbank and A. Lochiel, *Mass transfer coefficients, velocities and shapes of carbon dioxide bubbles in free rise through distilled water,* Chemical Engineering Science **19**, 485 (1964).

[13] N. Frössling, *Über die verdunstung fallender tropfen (on the evaporation of falling drops),* Gerlands Beitr Geophys. **52**, 170 (1938).

[14] P. Calderbank and M. Moo-Young, *The continuous phase heat and mass-transfer properties of dispersions,* Chemical Engineering Science **16**, 39 (1961).

[15] B. Figueroa-Espinoza and D. Legendre, *Mass or heat transfer from spheroidal gas bubbles rising through a stationary liquid,* Chemical Engineering Science **65**, 6296 (2010).

[16] J. Solsvik, *Lagrangian modeling of mass transfer from a single bubble rising in stagnant liquid,* Chemical Engineering Science **190**, 370 (2018).

[17] W. Nock, S. Heaven, and C. Banks, *Mass transfer and gas–liquid interface properties of single CO_2 bubbles rising in tap water,* Chemical Engineering Science **140**, 171 (2016).

[18] J. E. Olsen, D. Dunnebier, E. Davies, P. Skjetne, and J. Morud, *Mass transfer between bubbles and seawater,* Chemical Engineering Science **161**, 308 (2017).

[19] S.-L. Yan, X.-q. Wang, L.-T. Zhu, X.-B. Zhang, and Z.-H. Luo, *Mechanisms and modeling of bubble dynamic behaviors and mass transfer under gravity: A review,* Chemical Engineering Science **277**, 118854 (2023).

[20] M. Baltussen, *How fundamental knowledge on mass transfer in bubbly flows will help process intensification,* Chemical Engineering and Processing - Process Intensification **187**, 109344 (2023).

[21] D. Legendre and R. Zevenhoven, *Detailed experimental study on the dissolution of CO_2 and air bubbles rising in water,* Chemical Engineering Science **158**, 552 (2017).

[22] S. Alves, S. Orvalho, and J. Vasconcelos, *Effect of bubble contamination on rise velocity and mass transfer,* Chemical Engineering Science **60**, 1 (2005).

[23] J. Huang and T. Saito, *Influence of bubble-surface contamination on instantaneous mass transfer,* Chemical Engineering & Technology **38**, 1947 (2015).

[24] P. Valiorgue, N. Souzy, M. E. Hajem, H. B. Hadid, and S. Simoëns, *Concentration measurement in the wake of a free rising bubble using planar laser-induced fluorescence (PLIF) with a calibration taking into account fluorescence extinction variations,* Experiments in Fluids **54** (2013), 10.1007/s00348-013-1501-y.

[25] S. Hosoda, S. Abe, S. Hosokawa, and A. Tomiyama, *Mass transfer from a bubble in a vertical pipe,* International Journal of Heat and Mass Transfer **69**, 215 (2014).

[26] J. Schindelin *et al.*, *Fiji: An open-source platform for biological-image analysis,* Nature Methods **9**, 676 (2012).

[27] L.-K. Huang and M.-J. J. Wang, *Image thresholding by minimizing the measures of fuzziness,* Pattern recognition **28**, 41 (1995).

[28] W. M. Haynes, *CRC handbook of chemistry and physics: a ready-reference book of chemical and physical data* (Boca Raton : CRC Press, 2009).

[29] M. J. Doughty, *ph dependent spectral properties of sodium fluorescein ophthalmic solutions revisited,* Ophthalmic and Physiological Optics **30**, 167 (2010).

[30] G. Kong, K. Buist, E. Peters, and J. Kuipers, *Dual emission LIF technique for pH and concentration field measurement around a rising bubble,* Experimental Thermal and Fluid Science **93**, 186 (2018).

[31] M. Stöhr, J. Schanze, and A. Khalili, *Visualization of gas–liquid mass transfer and wake structure of rising bubbles using pH-sensitive PLIF,* Experiments in Fluids **47**, 135 (2009).

[32] L. Amaya-Bower and T. Lee, *Single bubble rising dynamics for moderate reynolds number using lattice boltzmann method,* Computers & Fluids **39**, 1191 (2010).

[33] G. Mougin and J. Magnaudet, *Path instability of a rising bubble,* Phys. Rev. Lett. **88**, 014502 (2001).

[34] J. Magnaudet and G. Mougin, *Wake instability of a fixed spheroidal bubble,* Journal of Fluid Mechanics **572**, 311337 (2007).

[35] T. Saito and M. Toriu, *Effects of a bubble and the surrounding liquid motions on the instantaneous mass transfer across the gas–liquid interface,* Chemical Engineering Journal **265**, 164 (2015).

[36] J. C. Cano-Lozano, C. Martínez-Bazán, J. Magnaudet, and J. Tchoufag, *Paths and wakes of deformable nearly spheroidal rising bubbles close to the transition to path instability,* Phys. Rev. Fluids **1**, 053604 (2016).

[37] C. Veldhuis, A. Biesheuvel, and L. van Wijngaarden, *Shape oscillations on bubbles rising in clean and in tap water,* Physics of Fluids **20**, 040705 (2008).

[38] P. Saffman, *On the rise of small air bubbles in water,* Journal of Fluid Mechanics **1**, 249 (1956).

[39] K. Lunde and R. J. Perkins, *Shape oscillations of rising bubbles,* Applied Scientific Research **58**, 387408 (1997).

[40] C. H. J. Veldhuis, *Leonardo's Paradox: path and shape instabilities of particles and bubbles*, Ph.D. thesis, University of Twente, Netherlands (2007).

[41] D. Turney and S. Banerjee, *Transport phenomena at interfaces between turbulent fluids,* AIChE Journal **54**, 344 (2008).

[42] A. Tomiyama, G. Celata, S. Hosokawa, and S. Yoshida, *Terminal velocity of single bubbles in surface tension force dominant regime,* International Journal of Multiphase Flow **28**, 1497 (2002).

[43] J. Boussinesq, *Calcul du pouvoir refroidissant des fluides,* Journal de Mathématiques Pures et Appliquées **1**, 285 (1905).

[44] P. V. Danckwerts, *Significance of liquid-film coefficients in gas absorption,* Industrial & Engineering Chemistry **43**, 1460 (1951).

[45] J. Francois, N. Dietrich, P. Guiraud, and A. Cockx, *Direct measurement of mass transfer around a single bubble by micro-plifi,* Chemical Engineering Science **66**, 3328 (2011).

[46] F. Takemura and A. Yabe, *Gas dissolution process of spherical rising gas bubbles,* Chemical engineering science **53**, 2691 (1998).

[47] D. Colombet, D. Legendre, A. Cockx, P. Guiraud, F. Risso, C. Daniel, and S. Galinat, *Experimental study of mass transfer in a dense bubble swarm,* Chemical engineering science **66**, 3432 (2011).

[48] S. Nedeltchev, U. Jordan, and A. Schumpe, *Correction of the penetration theory based on mass-transfer data from bubble columns operated in the homogeneous regime under high pressure,* Chemical Engineering Science **62**, 6263 (2007).

[49] O. Bork, M. Schlueter, and N. Raebiger, *The impact of local phenomena on mass transfer in gas-liquid systems,* The Canadian Journal of Chemical Engineering **83**, 658 (2005).

[50] A. Tomiyama, I. Kataoka, I. Zun, and T. Sakaguchi, *Drag coefficients of single bubbles under normal and micro gravity conditions,* JSME International Journal Series B Fluids and Thermal Engineering **41**, 472 (1998).

[51] D. Rodrigue, *A general and correlation for the rise and velocity and of single and gas bubbles,* The Canadian Journal of Chemical Engineering **82** (2004), 10.1002/cjce.5450820219.

[52] D. W. Moore, *The velocity of rise of distorted gas bubbles in a liquid of small viscosity,* Journal of Fluid Mechanics **23**, 749 (1965).

[53] T. K. Tuoc, *Reflections on a penetration theory of turbulent heat transfer,* arXiv preprint arXiv:1009.2280 (2010), 10.48550/arXiv.1009.2280.

[54] J. Huang and T. Saito, *Influences of gas–liquid interface contamination on bubble motions, bubble wakes, and instantaneous mass transfer,* Chemical Engineering Science **157**, 182 (2017).

[55] J. C. Cano-Lozano, J. Tchoufag, J. Magnaudet, and C. Martínez-Bazán, *A global stability approach to wake and path instabilities of nearly oblate spheroidal rising bubbles,* Physics of Fluids **28**, 014102 (2016).

[56] C. D. Ohl, A. Tijink, and A. Prosperetti, *The added mass of an expanding bubble,* Journal of Fluid Mechanics **482**, 271 (2003).

[57] A. Dueñas, I. Wieland, W. Marcum, and Q. Wu, *Form drag coefficient quantification on rising bubbles using particle image velocimetry,* Flow Measurement and Instrumentation **80**, 101988 (2021).

[58] Y. Hori, K. Hayashi, S. Hosokawa, and A. Tomiyama, *Mass transfer from single carbon-dioxide bubbles in electrolyte aqueous solutions in vertical pipes,* International Journal of Heat and Mass Transfer **115**, 663 (2017).

[59] X. Yan, K. Zheng, Y. Jia, Z. Miao, L. Wang, Y. Cao, and J. Liu, *Drag coefficient prediction of a single bubble rising in liquids,* Industrial & Engineering Chemistry Research **57**, 5385 (2018).

[60] Y. Zhou, C. Zhao, and H. Bo, *Analyses and modified models for bubble shape and drag coefficient covering a wide range of working conditions,* International Journal of Multiphase Flow **127**, 103265 (2020).

[61] N. N. Greenwood and A. Earnshaw, *Chemistry of the Elements* (Butterworth-Heinemann, 2012).

5

CONCLUSIONS AND OUTLOOK

5.1. CONCLUSIONS

Bubbly flows, a subset of multiphase flows, are found in a variety of chemical and biochemcial applications. In the past decades, considerable research has been done at various scales, from laboratory to real industrial scale, in order to improve processes towards profitability, yet conforming to environmental regulations and ever increasing societal norms of sustainability. In developing 'green' technologies for the future, Prof. Dudukovic [1] rightly questions: *do our current design and scale-up methods incorporate scientific advances or are they extensions of previous largely empirical approaches having limited utility and reliability*? As the complexity of applications increases, a coupled understanding of the local phenomena in these processes, fluid dynamics, mass transfer, chemical reactions, and their interplay, becomes highly relevant, prior to extending any models towards large scale systems [2].

The current project was motivated by the necessity to understand the fundamental challenges in practical implementations of bubbly flows, specifically on two topics: CO_2 capture and electrolysis. Besides thermodynamic considerations and chemical reactions, bubbly flows play a strong role in scalability of these processes. We focus on answering key fundamental questions, as outlined in **Chapter 1**, towards building a mechanistic *picture* of the interplay involved, that can aid in the development of design models for these processes.

ELECTROLYTES

Presence of electrolytes inhibiting coalescence is well-studied in literature [e.g. 3]. In **Chapter 2**, we focused on extending this understanding towards electrolysis process. The role of bubble coalescence inhibition due to electrolyte (0-2M NaCl salt in water), at a fine-pore sparger (mimicking surface bubble generation at an electrode), on the hydrodynamics of a dense recirculating flow was investigated. An addition of 0.1M NaCl to water was sufficient to change the flow profile in the airlift column and induce recirculation; opaqueness of the flow increased with increasing salt concentrations and higher gas flow rates. This is strongly associated with change in the bubble size distribution at the sparger, due to coalescence inhibition; whereas 2-3mm size bubbles were produced

in water, the addition of NaCl led to the occurrence of a large fraction of micron-size bubbles (~ 100-300 μm). Here, due to opaqueness of the flow, we used X-ray imaging technique to quantify the gas fraction profiles across the column, and high speed imaging to quantify the bubble size distribution at an individual sparger[1]. Our results showed that the bubble size distribution at the sparger dictates the bubble plume dynamics, (local) gas fraction and recirculation in the column; this is verified by an agreement with a simple 1D drift flux model. Further, we use a Bubble Imaging Velocimetry (BIV) technique to demonstrate that the dynamics of foam formation & disintegration at the free-surface plays a role in the recirculation of the smaller micron-size bubbles in the airlift column.

Classification of a fluid as pure or contaminated aids in the choice of appropriate available correlation(s) for describing bubble motion. In **Chapter 3**, we study the rise of a single H_2 bubble in water and typical (chlorate)-electrolysis conditions: high concentration solutions of single and mixed electrolytes, at temperatures up to 80°C. We focussed on an ellipsoidal bubble; due to an interplay between interfacial behaviour and bubble motion, bubbles in this regime are strongly influenced by the presence of contaminants [5]. Our results show that both individual and collective effects of the temperature and high concentration electrolytes can be described by knowledge of the liquid properties (density, viscosity and *static* surface tension); the bubble motion can be described by well-known empirical data on pure liquids. Based on the experimental data, a simple non- dimensional parametrization extension is proposed for the bubble motion and drag coefficient, from viscous to practically-relevant intermediate *Re* regime ($\mathcal{O}(10^2 - 10^3)$).

CO_2 MASS TRANSFER

In **chapter 4**, we study the interplay between hydrodynamics and mass transfer for a single CO_2 bubble in demineralized water. A comparison of the experimental mass transfer coefficient (k_L) with well-used interfacial- mobility-based mass transfer models (Higbie and Frossling) showed a non-agreement with either correlation; this is specially the case for ellipsoidal and wobbly bubbles. While deviations from classical mass transfer models are previously reported, this is often attributed to possible contaminants in water. In contrast to such claims, bubble rise velocities in our experiments exhibit a free-slip pure water behaviour. Based on qualitative understanding of bubble wake, with Laser induced fluorescence (LIF) technique, we demonstrate that the two regimes in k_L data, as a function of bubble size, are associated with wake-induced effects: path and shape oscillations of bubbles deviating from a spherical shape. Mass transfer is quasi-steady in nature; equally-sized shrinking CO_2 and non-shrinking N_2 bubbles showed similar bubble motion.

The interplay between mass transfer and hydrodynamics is dependent on the bubble size regime; the current correlations used for ellipsoidal and wobbly bubbles (most found in practical cases) are based on classical models (Higbie and Frossling). These models, based on assumptions of potential/ creeping flow around a spherical bubbles, cannot be (semi-) empirically extended to non-spherical bubbles without a good understanding of the prevailing interplay between flow around the bubbles, wake effects and its influence on convective mass transport. Here, based on analogy between momentum and mass transfer, we propose a non-dimensional parametrization for describing

[1] Experimental data is available on 4TU research data platform [4]

convective aspects of bubble motion and mass transfer. The derived mechanistic correlation, based on Stanton number (St_m), can be used to predict k_L based on knowledge of a well-studied hydrodynamic parameter, the drag coefficient (C_D). Further, we observe an inherent link between the bubble path amplitude and the ratio of mass & momentum transfer coefficients ($k_L/h_u = St_m/C_D$), necessitating a deeper understanding of dynamic bubble behaviours in further development of mass transfer models.

5.2. DILUTE BUBBLY FLOW: ELECTROLYTES AND CO_2 MASS TRANSFER

In the previous chapters, we covered the role of electrolyte (on a single bubble and dense recirculating flow) and mass transfer (on a single bubble). As an extension to these studies, we further investigate the effect of electrolytes and CO_2 mass transfer at an intermediate scale of a homogenous dilute bubbly flow[2]. Experimental details and post-processing methods, used in this study, are outlined in Appendix A.

For the four cases studied, Figure 5.1 (a-d) shows instantaneous flow snapshots and bubbly velocity profiles, obtained from a Bubble imaging Velocimetry (BIV) technique, at the same gas superficial velocity. For the case of N_2 gas bubbles in water, a homogeneous flow profile is observed, with an unimodal bubble size distribution (BSD). Both the cases of electrolyte addition (up to 1M NaCl) and CO_2 mass transfer lead to a complex flow structure, with an oscillatory bubble plume and recirculation cells.

The complex flow dynamics, in both cases, arises from a bi-modal bubble size distribution (BSD) (Figure 5.1 (e-f)). In the electrolyte case, bubble generation process at the sparger is observed to be expedited, leading to a larger fraction of smaller bubbles with increasing concentration. CO_2 mass transfer gives rise to smaller bubbles, which are trapped in the circulation cells. As the liquid column get saturated with CO_2, the BSD and the flow behaviour tends towards a homogenous situation, similar to a N_2 case. The combined effect of electrolytes and shrinking CO_2 bubble size, on the hydrodynamics and the mass transfer, is also investigated. Here, the slower dissolution of CO_2 in saline solutions introduces an additional interplay, leading to differences in the bubble size distribution and in the transient nature of the oscillations in the bubble plume.

A part of finalizing this study would be a parametrization of the bubble plume dynamics, addressing the individual and collective effects of electrolytes and gas-liquid mass transfer through its influence on the bubble size distribution.

[2] This work is a part of a *manuscript-under-preparation* and has been presented at the International Conference of Multiphase Flow (ICMF), Brazil, 2019

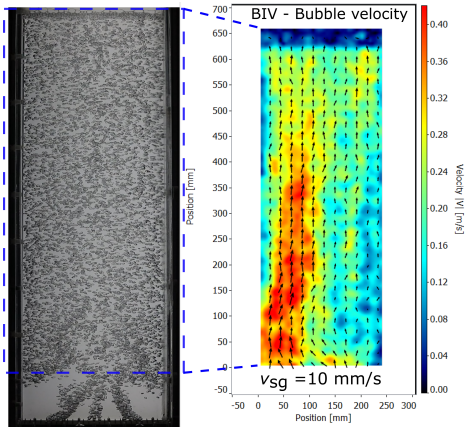

(a) N_2 bubbles in water

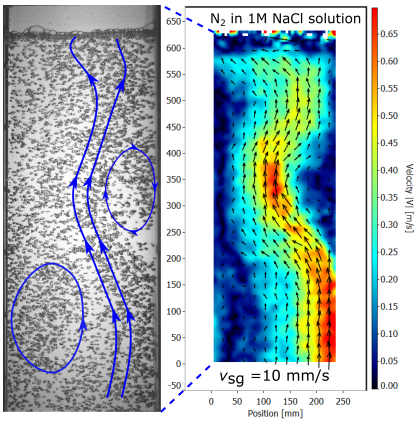

(b) N_2 bubbles in 1M NaCl solution

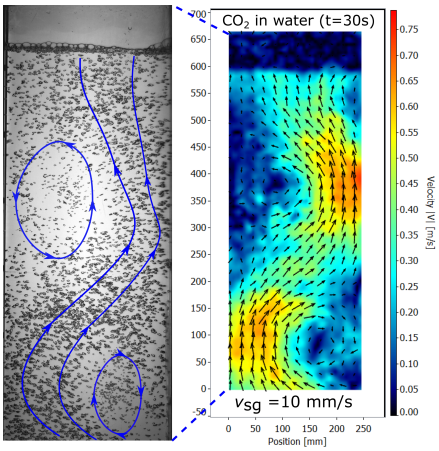

(c) CO_2 bubbles in water

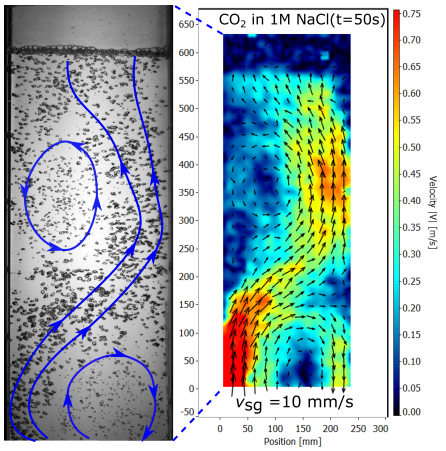

(d) CO_2 bubbles in 1M NaCl solution

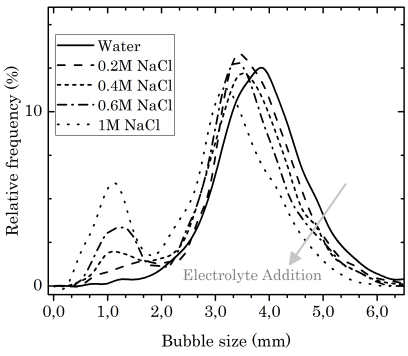

(e) Bubble sizes: Electrolyte effect

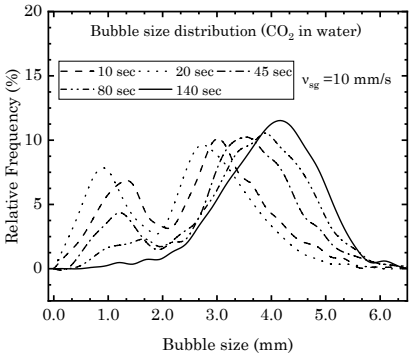

(f) Bubble sizes: CO_2 bubbles dissolution in water

Figure 5.1: Snapshots of flow and corresponding Bubble imaging velocimetry (BIV) results, at a gas superficial velocity of v_{sg}=10 mm/s, for: (a) N_2 gas in water (reference), (b) N_2 gas in 1M NaCl solution in water, (c) CO_2 bubbles in water. Blue markings indicates motion of plume and the circulation cells. Bubble size distribution at v_{sg}=10 mm/s: (d) as function of electrolyte concentration (0-1M NaCl), (e) CO_2 bubbles in water, at different times during dissolution (t=0 indicates start of gas sparging).

5.3. OUTLOOK

5.3.1. (DE)COUPLING MASS TRANSFER AND HYDRODYNAMICS

In **chapter 4**, we studied an analogy between hydrodynamics and mass transfer to correlate the mass transfer coefficient (k_L) in terms of the bubble drag coefficient (C_D). Since our study was limited to one fluid (water), the role of the Schmidt number ($Sc = \mu/\rho D_L$, Sc_{water} at 298K = 457) was not included. A further important extension to this study would be exploring a wider span of the parameter space of fluid properties, with different viscosities (μ) and diffusivities (D_L); at lower Sc, diffusion process at the mass transfer boundary layer would play a stronger role. Based on a similarity in C_D profile for bubbles in a variety of pure fluids, it can be speculated that the proposed analogy-based method in addressing the interplay would be applicable for other fluids with high Sc.

A further challenge in extending the knowledge from a single bubble to dilute bubbly flows is the inclusion of the dynamic bubble behaviour. In current meso-scale computational models, bubble shape and path oscillations are seldom included, limited by computational complexity and simplified models arising from rigorous DNS simulations/experiments. Recent studies [e.g. 6] have made progress in this direction, including a stochastic method for predicting bubble eccentricities and trajectories. Predictability of these models towards practical cases needs be addressed by generating good benchmarking experimental data. The measurement challenge is in correlating the local phenomena (bubble sizes, flow and concentration) in a bubble column to the global measurements; this complexity is amplified by non-ideal cases with strong change in flow behaviour, as observed in our study on dilute flow (up to 8%). A step further could be resource-intensive, utilizing a multi-camera/multi-technique system to investigate the local hydrodynamics and mass transfer at different locations in a column, coupled with Machine Learning (ML) based models for image analysis. As interfacial reflections limit laser-based techniques for measuring dissolved concentrations (e.g. LIF) to very dilute flows (few bubbles trajectories), pragmatic understanding of the hydrodynamics-mass transfer interplay would be pertinent for extending the knowledge to both dilute and denser flows.

5.3.2. INTERFACIAL RHEOLOGY & LOCAL PHENOMENA

A detailed analysis of multiphase flows in reactors relies on a precision in the prediction of the local-scale flow phenomena, based on models that describe the bubble hydrodynamics, and the interfacial processes of heat and mass transfer. Properties of fluids become highly relevant, specially for processes involving a multitude of solutes (salts, surfactant, alcohols, sugars, proteins etc.) [7]. Each solute can cause multiple behaviour in different contexts. For example: electrolytes show a strong ion-specific influence on bubble coalescence [3], while in terms of bubble rise behave as pure fluids (current thesis). Design models for describing fundamental mechanisms in such flows: bubble generation, dynamic rise behaviours, swarm effects, coalescence & breakup, are often based on ad-hoc studies done at meso- or macro-scale [e.g. 6, 8]. Decoupling the effects is crucial in developing scalable models; understanding solute behaviours at the gas-liquid interface and the impact on interfacial rheology could bring further insights into the bubble hydrodynamics and mass transfer processes.

Non-dimensional parametrization for bubble rise, based on experiments done half-a-century ago, such as Clift *et al.* [5] map for pure liquids and Loth [9] correlation for

contaminated fluids, are found to be still useful in predictions [3]. Newer models/regime maps based on measurable rheological parameters, such as power law models, dynamic surface tension, surface shear viscosity, surface elasticity, etc., would aid in developing a general understanding for the interaction between multiphase flow and industrial chemistry in applications, such as electrolysis, wastewater treatment, biotechnology, froth flotation and many more.

REFERENCES

[1] M. P. Dudukovic, *Frontiers in reactor engineering,* Science **325**, 698 (2009).

[2] M. Schlüter, S. Herres-Pawlis, U. Nieken, U. Tuttlies, and D. Bothe, *Small-scale phenomena in reactive bubbly flows: Experiments, numerical modeling, and applications,* Annual Review of Chemical and Biomolecular Engineering **12**, 625 (2021), pMID: 34097844.

[3] T. T. Duignan, *The surface potential explains ion specific bubble coalescence inhibition,* Journal of Colloid and Interface Science **600**, 338 (2021).

[4] M. Mandalahalli, E. Wagner, L. M. Portela, and R. Mudde, *Experimental data: electrolyte effects on hydrodynamics in an airlift bubble column [dataset],* 4TU.ResearchData (2023), 10.4121/15087255.v1.

[5] R. Clift, J. Grace, and M. Weber, *Bubbles, Drops and Particles* (New York: Academic Press, 1978).

[6] M. A. Taborda, P. Kováts, K. Zähringer, and M. Sommerfeld, *The influence of liquid properties on flow structure, bubble dynamics and mass transfer in a laboratory bubble column: Experimental analysis versus numerical modelling and computation,* Chemical Engineering Research and Design **185**, 51 (2022).

[7] R. Volger, L. Puiman, and C. Haringa, *Bubbles and broth: A review on the impact of broth composition on bubble column bioreactor hydrodynamics,* Biochemical Engineering Journal **201**, 109124 (2024).

[8] Y. Kawase, S. Umeno, and T. Kumagai, *The prediction of gas hold-up in bubble column reactors: Newtonian and non-newtonian fluids,* The Chemical Engineering Journal **50**, 1 (1992).

[9] E. Loth, *Quasi-steady shape and drag of deformable bubbles and drops,* International Journal of Multiphase Flow **34**, 523 (2008).

[3] Despite best efforts in developing rigorous models based on experimental and numerical investigations, current multiphase reactor models are often dependent on pragmatic simplistic correlations.

A

FURTHER WORK: DILUTE BUBBLY FLOW

In the previous chapters we covered the role of electrolyte (on a single bubble and dense recirculating flow) and mass transfer (on a single bubble). As an extension to these studies, we investigate the effect of electrolytes and CO_2 mass transfer at an intermediate scale of a homogenous dilute bubbly flow.

EXPERIMENTAL SETUP & METHODOLOGY

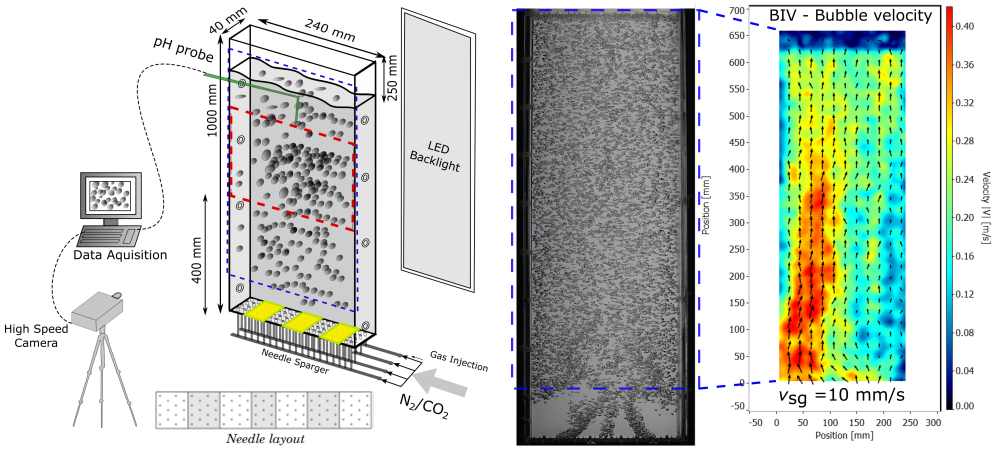

(a) **(b)**

Figure A.1: (a) Schematic of pseudo-2D bubble column equipped with 98-needle sparger. 3 groups of needles (grey color in needle layout) have been used to sparging gas. Dashed lines: red (- - - -) and blue (- - - -) indicate acquisition window for bubble size distribution and bubble imaging velocimetry (BIV), respectively. (b) Snapshot of flow and bubble rise velocity profile (from BIV analysis) for the case of N_2 gas in water at v_{sg}=10 mm/s. Note that a smaller acquisition window (not including the sparger section) has been used as an input for BIV analysis.

The experimental setup, a schematized in Figure A.1a, consists of a rectangular bubble column (WxDxH= 240 mm x 40 mm x 1000 mm), equipped with a needle sparger system, with 98 orifices. The large number of needles, divided into 7 groups, were originally designed to operate the column with different sparger configurations ; using all the needles enabled to operate in a homogenous flow regime for a high gas fraction [1]. For the current study, only a partial set of needles (groups 2, 4, 6) are used, enabling a generation of three bubble plumes at a lower gas superficial velocities ($v_{sg} \in [2;16]$ mm/s), corresponding to a gas fraction of 1.5 -8%. Unused needles are stubbed to avoid liquid weeping.

The two gases used: CO_2 (≥ 99.7 vol%, grade 2.7, Linde) and N_2 (≥ 99.9 vol%, grade 3.0, Linde), are supplied from separate cylinders (not in schematic). The flow of both gases is controlled independently, using each a thermal mass flow controllers (Bronkhorst B.V., 0-20 l/min). The initial non-sparged liquid height is maintained at 750 mm. All experiments are performed at room temperature (T=298K). For electrolyte studies, purified sodium chloride (Sigma Aldrich, laboratory grade NaCl) is used in the concentration range 0.1-1.0M (mol/liter). To avoid needle clogging or salt deposition, electrolyte solutions are externally prepared before adding to the column.

Operation : CO_2 experiments are performed using a degassing method. Before each experiment, the column is sparged with N_2 gas till a pH of 7 is reached (measured using pH meter). The gas flow is stopped in the column for c.a. 10 minutes to ensure no liquid flow. A switch between the gases is controlled using an electronically controlled 3-phase valve.

Measurement of dissolved CO_2 is done using a pH meter (MetrOhm 913 with Pt1000 electrode, sensitivity ± 0.01). Solving the equilibrium equations with corresponding rate constants (obtained from [2]), a conversion between pH and CO_2 concentration can be obtained (Eqn. A.1).

$$\begin{aligned} CO_2(g) &\overset{k_H}{\rightleftharpoons} CO_2(aq); \qquad k_H = 8.3\text{x}10^{-1} \\ CO_2 + H_2O &\overset{K_h}{\rightleftharpoons} H_2CO_3; \qquad K_h = 1.2\text{x}10^{-3} \\ H_2CO_3 &\overset{K_a}{\rightleftharpoons} HCO_3^- + H^+; \qquad K_a = 2.5\text{x}10^{-4} \\ K_W &= [OH^-][H^+] = 10^{-14} \end{aligned} \tag{A.1}$$

$$[CO_2] = \frac{[H^+] - K_W}{K_h K_a}; \qquad pH = -log_{10}[H^+] \tag{A.2}$$

Addition of electrolyte changes the equilibrium values and lowers the overall solubility of CO_2. The evolution of acid dissociation constant K_a (obtained from [3])is

$$pKa = \frac{3670.7}{T} - 62.008 + 9.7944 ln(T) - 0.0118S + 0.000116S^2 \tag{A.3}$$

Here S is the salinity of the solution in g/L. Higher salinity decreases the solubility of CO_2, but increase the dissociation constants, hereby, decreasing the measured pH.

IMAGE ACQUISITION & DIGITAL IMAGE ANALYSIS

Image acquisition is performed for three purposes:

- *Flow snapshots:* Instantaneous flow images are acquired using a DSLR camera (Canon EOS R, 50 mm, f2.8, at 30fps). The images here encompass the entire column, from sparger to the top free surface, and are used to characterize the oscillatory behaviour of the plume.
- *Bubble velocity:* Bubble image velocimetry (BIV) technique is used to compute the bubble velocity in the section above the sparger section. The technique has been used earlier in Chapter 2. Images are acquired at 1000fps using using a high speed camera: (LaVision Imager Pro HS 4M, resolution 2016x2016 px^2at a 1278 Hz frequency) with a field of view of 26 cm (W) x 65 cm (H), 10 cm above sparger section. Using a shallow focal depth (with aperture f/1.8), the *texture* of the gas-liquid interface can be captured with shadowgraphy imaging, similar to a sheet illumination. Subsequently, the images are inverted and cross-correlated using standard PIV algorithms in LaVision DaVis 8.0 software.
- *Bubble size and gas fraction:* Bubble size measurements are performed using a high speed camera: (LaVision Imager Pro HS 4M, resolution 2016x2016 px^2at a 1278 Hz frequency), 400mm above the sparger section with a field of view of 24 cm (W) x 24 (H). Image processing technique to obtain bubble size distribution is performed, as outlined in Fu and Liu [4]. From the raw images, following steps are followed:

  – Background subtraction, homogenization and brightness correction.
  – Edge detection to determine outline of bubble clusters & individual bubbles.
  – Watershed segmentation and bubble outline analysis.
  – Ellipsoidal bubble fitting to obtain bubble sizes.

  Based on ellipsoid fitting, bubble equivalent diameter and gas fractions are evaluated; here bubble shape is assumed to be of a spheroidal shape, with the vertical axis as the symmetry axis.

FLOW PATTERNS: INFLUENCE OF ELECTROLYTE AND CO_2 MASS TRANSFER

N_2-WATER CASE

For the reference case of N_2-water, two distinct regions in the flow pattern are observed (Figure A.1b): (i) an oscillating bubble plume region at the lower section of the column, (ii) a homogenous dispersed region at the upper part of the column. This behaviour can be attributed to the non-uniform aeration at the sparger; using a partial set of needles leads to a presence of two vortical structures in the column bottom [e.g. 5]. When the bubbles located at the extremes of the combined plume, from the three group of nozzles, they are displaced towards the column walls. Consequently, a low frequency meandering in the bubble plume is observed, leading to a fluctuations in the lateral bubble velocity profile in the lower sections of the column.

ELECTROLYTE EFFECT

Influence of electrolyte addition is studied with up to 1M (mol/liter) NaCl solution in water. The flow profile in presence of electrolyte shifts to a pseudo-heterogeneous regime (Figure A.2a); coupled to a centrally rising bubble plume, circulation cells are observed towards the wall. Bubble sizes measured in the column (400mm above sparger, Figure

A.2b), show an increasing bimodal distribution with the electrolyte addition. The circulation cells are not well-defined, counteracted by the buoyancy of predominantly ellipsoidal bubbles in them. Non-uniform bubble size can trigger bubble clustering and a higher rise velocities observed in BIV imaging.

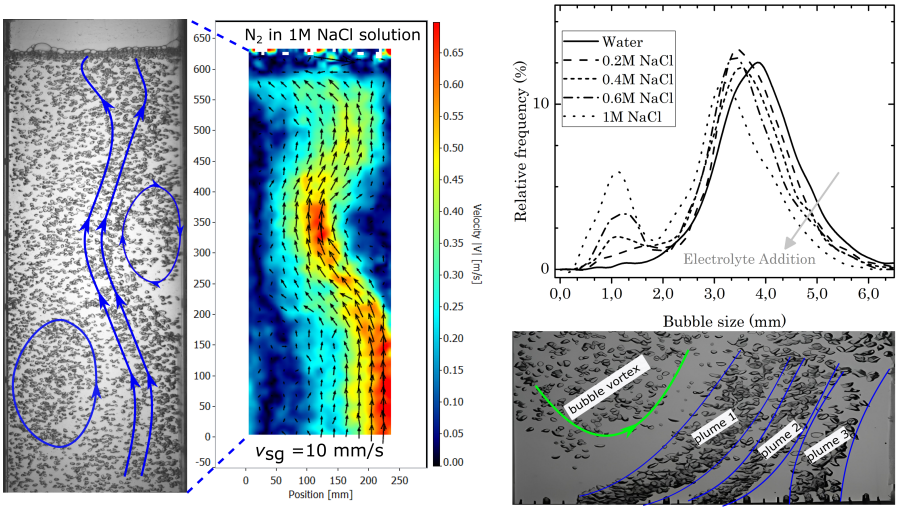

Figure A.2: (a) N_2 bubbles in 1M NaCl solution at v_{sg}=10 mm/s: Flow profile (blue markings indicating motion of plume and the circulation cells) and bubble velocity profile (b) top: Bubble size distribution as a function of electrolyte concentration at v_{sg}=10 mm/s; Bottom: snapshot of bubble flow close to the sparger (contrast enhanced) showing interaction of bubble vortex and plume generation from the sparger.

Bubble generation process at the sparger is observed to be expedited in the electrolyte solutions, possibly due to an interaction withe bubble vortex, leading to a larger fraction of smaller bubbles with increasing concentration. While this is also observed at the startup stage for the reference case of N_2 bubbles in water (without electrolytes), the bubble dispersion seemed to stabilize into low frequency meandering of bubble plumes Mudde [6]. For the electrolyte case, however, the instability seems to sustain for longer times with periodic liquid flow feedback to the sparger, generating smaller bubbles.

GAS-LIQUID MASS TRANSFER

A majority of investigations related to gas-liquid mass transfer are performed with an air-water system, monitoring O_2 dissolution in liquids [e.g. 7]; a mass transfer process with a slow dissolving gas has a limited effect on the bubble size and on the overall hydrodynamics. CO_2 dissolution in water, on the other hand, introduces a two-way coupling between mass transfer and hydrodynamics, arising from the dynamic nature of the bubble size distribution.

As shown in Figure A.3a, during the CO_2 absorption, the flow profile exhibits a strong oscillatory plume behaviour with circulation cells. Such a behaviour is triggered by mass transfer of bubbles along edges of a bubble plume (Figure A.3b), and migration of smaller bubbles, due to a difference in slip velocities, towards side-walls of the column. Smaller

bubbles, generated as a consequence of mass transfer, are more easily trapped inside the large scale vortices more frequently.

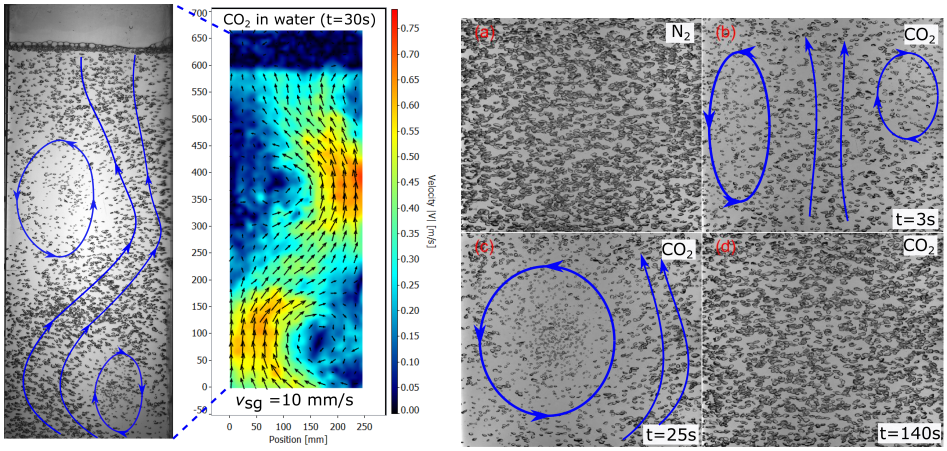

Figure A.3: CO_2 bubbles in water at v_{sg}=10 mm/s: (a) Flow profile (blue markings indicating motion of plume and the circulation cells) and bubble velocity profile at t=30 sec (b) Snapshots of bubble images (captured at 400 mm above sparger) comparing N_2 and CO_2 case (at t=3 sec, 25 sec and 140sec). Times stated here are from the start of gas sparging.

Figure A.4 shows flow profiles at different times during an absorption period (140 seconds for the case of v_{sg} =10 mm/s). Circulation cells with small bubbles are observed to move downward towards the sparger region and disperse due to interaction with the kinetic energy of incoming bubbles, leading to a meandering in the plume. As the liquid gets saturated, with smaller driving force for mass transfer, the bubble sizes moves towards a unimodal distribution (Figure A.5a). Correspondingly, the circulation cells are smaller and ultimately are confined to the sparger region as the flow profile tends towards the N_2 case. Final bubble sizes of CO_2 bubbles are found to be slightly larger than the N_2 ones. This could be attributed to the couter-diffusion of N_2 (from liquid to bubble) during the CO_2 absorption [8]; starting condition for the experiments is water degassing with N_2 gas.

The combined effect of electrolytes and shrinking CO_2 bubble size, on the hydrodynamics and the mass transfer, is also investigated. Here, the slower dissolution of CO_2 in saline solutions introduces an additional interplay, leading to differences in the bubble size distribution and in the transient nature of the oscillations in the bubble plume. A part of finalizing this study would be a parametrization of the bubble plume dynamics, addressing the individual and collective effects of electrolytes and gas-liquid mass transfer through its influence on the bubble size distribution.

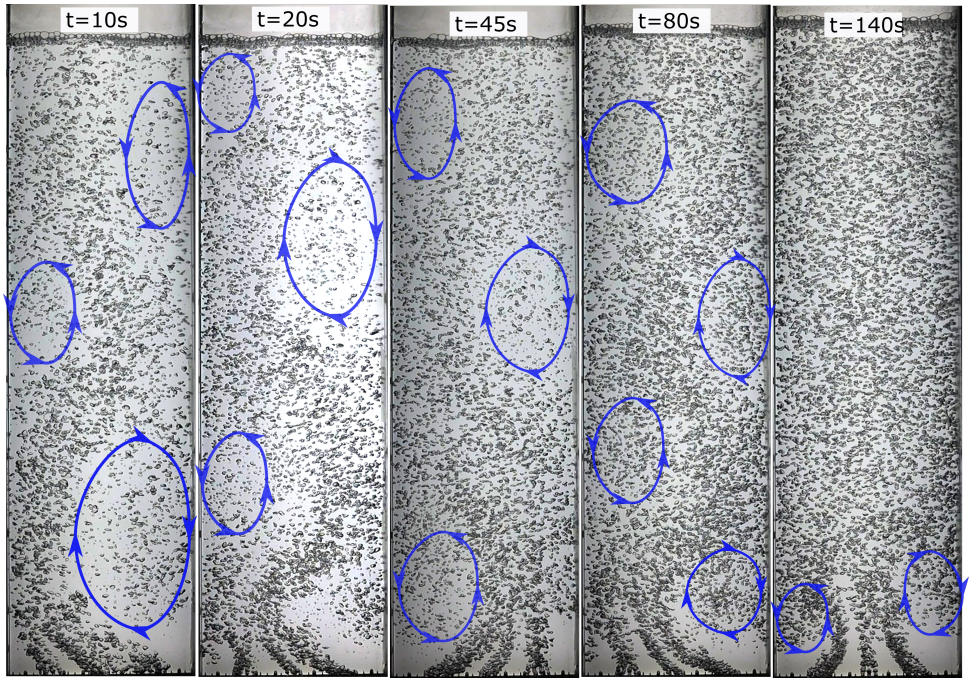

Figure A.4: CO_2 bubbles in water at v_{sg}=10 mm/s: Instantaneous flow snapshots at different times during the absorption process (blue markings indicate the circulation cells).

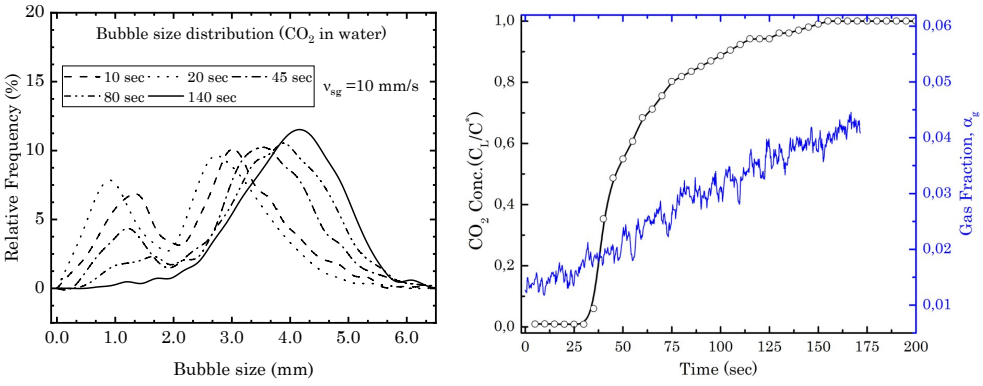

Figure A.5: CO_2 bubbles in water at v_{sg}=10 mm/s: (a) Bubble size distribution at different times (as indicated in Figure A.4). (b) Instantaneous CO_2 concentration (measured using a pH probe), normalized with equilibrium concentration C^* and gas fraction (measured using Digital image analysis). Times stated here are from the start of gas sparging.

REFERENCES

[1] D. Darmana, N. Deen, J. Kuipers, W. Harteveld, and R. Mudde, *Numerical study of homogeneous bubbly flow: Influence of the inlet conditions to the hydrodynamic be-*

havior, International Journal of Multiphase Flow **35**, 1077 (2009).

[2] N. N. Greenwood and A. Earnshaw, *Chemistry of the Elements* (Butterworth-Heinemann, 2012).

[3] A. L. Soli and R. H. Byrne, *Co2 system hydration and dehydration kinetics and the equilibrium co2/h2co3 ratio in aqueous nacl solution,* Marine Chemistry **78**, 65 (2002).

[4] Y. Fu and Y. Liu, *Development of a robust image processing technique for bubbly flow measurement in a narrow rectangular channel,* International Journal of Multiphase Flow **84**, 217 (2016).

[5] L. Liu, H. Yan, T. Ziegenhein, H. Hessenkemper, Q. Li, and D. Lucas, *A systematic experimental study and dimensionless analysis of bubble plume oscillations in rectangular bubble columns,* Chemical Engineering Journal **372**, 352 (2019).

[6] R. F. Mudde, *Gravity-driven bubbly flows,* Annual Review of Fluid Mechanics **37**, 393 (2005).

[7] D. Colombet, D. Legendre, F. Risso, A. Cockx, and P. Guiraud, *Dynamics and mass transfer of rising bubbles in a homogenous swarm at large gas volume fraction,* Journal of Fluid Mechanics **763**, 254285 (2015).

[8] S. Kastens, S. Hosoda, M. Schlüter, and A. Tomiyama, *Mass transfer from single taylor bubbles in minichannels,* Chemical Engineering & Technology **38**, 1925 (2015).

OUTREACH

JOURNAL PAPERS

4. M.M. Mandalahalli, J.L. Nienhuis, and L.M. Portela, *Electrolyte effect on bubble column with N_2 and CO_2: A visualization study on hydrodynamics and mass transfer*, (In Preparation) to be submitted to International Journal of Multiphase flow (2024).

3. M.M. Mandalahalli, J.C.L.M. Hermans, V.O. Oppeneer, and L.M. Portela, *An experimental study of the dynamics and mass transfer of a rising bubble*, International Journal of Multiphase flow (2024) (In Press).
DOI: 10.1016/j.ijmultiphaseflow.2024.104809.

2. M.M. Mandalahalli, J. Lif, R.F. Mudde, and L.M. Portela, *Electrolyte and temperature effects in a rising bubble*, Chemical Engineering Science, 270, 118276 (2023).
DOI: 10.1016/j.ces.2022.118276.

1. M.M. Mandalahalli, E.C. Wagner, L.M. Portela, and R.F. Mudde, *Electrolyte effects on recirculating dense bubbly flow: An experimental study using x-ray imaging*, AIChE Journal, 66, e16696 (2020).
DOI: 10.1002/aic.16696.

DATA PAPERS & PROCEEDINGS

1. M.M. Mandalahalli, E.C. Wagner, L.M. Portela, and R.F. Mudde, *Experimental data: electrolyte effects on hydrodynamics in an airlift bubble column*, 4TU. Research Data (2023). DOI: 10.4121/15087255.v1.

TRAINEESHIP & ANCILLARY WORK

2. *Making Bubbles, Breaking Boundaries - A quantitative model for Cross Flow Membrane Foaming process*, NWO-Physics with Industry & Friesland Campina B.V., Nov 2019.

1. *On-site traineeship on hydrogen production in chlorate electrolyzers*, AkzoNobel (now Nouryon) Pulp & Perfomance Chemicals A.B., Aug-Nov 2017.

CONFERENCE PRESENTATIONS & POSTERS

11. Netherlands Process Technology Symposium (NPS-16)
TU Eindhoven, Netherlands Nov 2019

10. JMBC Contact group on Multiphase Flow meeting with MARIN
Wageningen, Netherlands Sept 2019

9. International conference on Gas-liquid and Gas-Liquid-Solid Reactors (GLS-14)
   Guilin, China June 2019

8. International Conference on Multiphase Flows (ICMF)
   Rio-de-Janeiro, Brazil May 2019

7. AkzoNobel conference on Fundamentals in Electrochemical processes
   Sundsvall, Sweden Oct 2018

6. JM Burgers center symposium (poster)
   Lunteren, Netherlands Jun 2018

5. International workshop on Non-invasive experimental tools
   Hamburg, Germany Jun 2018

4. Delft Process Technology Institute (DPTI) symposium *(Best Poster award)*
   Rotterdam, Netherlands June 2018

3. Netherlands Process Technology Symposium (NPS-15) *(Best Poster award)*
   University of Twente, Netherlands May 2018

2. International conference on Gas-liquid & Gas-Liquid-Solid Reactors (GLS-13)
   Brussels, Belgium August 2017

1. Frontiers in Chlorate and Chlor-Alkali Research
   Ambes, France April 2017

CURRICULUM VITÆ

Manas Manohar Mandalahalli was born on 26th of November 1991, in Hindupur, Andhra Pradesh, India. He finished his primary and secondary education from Kendriya Vidhyalaya A.S.C, Bangalore, in 2009. He went on to do a Bachelors (B.E.) in Chemical Engineering from the B.M.S. College of Engineering, Bangalore, India, graduating in 2013. During his study, he spent the summer of 2012 as a research fellow at National Chemical Laboratory (NCL), Pune, India, that sparked his interest in reactor engineering and multiphase flows.

He then came to Netherlands in 2013, on a UTS Scholarship, for a Masters in Chemical Engineering at University of Twente, Enschede, with a specialization in Process Technology. During his Masters, he worked on multiple process design projects, including an Erasmus+ funded internship at Evonik Industries A.G., Germany, in 2015. He then worked in the Soft Matter, Fluidics & Interfaces (SFI) group at University of Twente for his MSc thesis on the intensification of liquid-liquid extraction in capillary flows, graduating in 2015. Manas then moved to Delft and joined the Transport Phenomena group as a PhD student, in the Department of Chemical Engineering, TU Delft. In a NWO- Industry partnership programme, he worked on studying multiscale gas-liquid flows with non-intrusive experimental techniques, culminating in the current thesis.

During 2020-21, Manas worked as a freelance technology consultant on analysing IP, academic & industrial literature towards building low-TRL portfolios in low-carbon biofuels, zero-water mining and 3D printing topics. Since 2021, Manas is working as a System Interaction Researcher at Canon Producting Printing B.V. (formerly Océ Technologies).

ACKNOWLEDGEMENTS

I would like to thank each and everyone: friends, family and colleagues who have supported me through this journey.

First of all, I am grateful to my promotor, Rob Mudde, and my co-promotor, Luis Portela, for your guidance and support. **Rob**, thank you for accepting me as a PhD candidate for this project. On my first day, I remember your advice on approaching a complex industrial challenge with a practical mindset. Our meetings have contributed greatly to shaping my research direction and in keeping my focus on addressing the most relevant fundamental questions. Over the past years, despite your busy schedule as the Vice-Rector Magnificus, you were quick in answering emails, offering words of encouragement, and giving feedback on manuscripts. **Luis**, you were on sabbatical at the time I joined the TP group. My first interaction with you was through your critical questions during my first presentation. While daunting for most students, your critical view, mechanistic approach, and quest for perfection have helped improve the quality of my work. Our *long* discussions would entail any topic: from non-dimensional analysis to the concept of freedom or the true definition of liberalism; I learned a lot from these conversations. Thank you for keeping me motivated to finalize the thesis.

I would like to thank other staff members of the TP group. **Chris**, as section leader, you were great at keeping the group lively and interactive, with lunch talks, company tours, BBQs, and Christmas dinners. **André**, we have known each other since my master's course on Process Design at UTwente. I enjoyed being the teaching assistant for your course on *Scheidingstechnologie*. Thank you for advising me during my transition to industrial research. **David**, you expanded my understanding of electrolysis. It was a pleasure to co-supervise many lab practical students with you. **Saša**, while our conversations were less scientific, you were always there to encourage me with a smile.

My experimental escapades wouldn't have been possible without the technical support. **Evert**, from Kramers Lab to the Reactor Institute, our X-ray experiments involved a lot of trial and error. You were amazing at coming up with new ideas to measure (3D) flows and helping with processing TBs of X-ray data. After working hours, I always enjoyed borrels with you, discussing travel ideas and photography. **Christian**, you were of immense help in setting up the laser imaging experiments, building electronics, and gently pushing me to speak in Dutch. **Stefan**, thank you for designing and building bubble columns and for putting up with the number of requests for changes that came your way. I had the pleasure of working together with various master's and bachelor student's, whose efforts led to interesting insights into measurement techniques. **Sander**, **Katerina**, **Johan**, **Lorenzo**, **Victor**, and **Job**, it was a pleasure to supervise you together with Luis. Besides your adventures in the lab, you were a great addition to the TP group.

My project being a part of a wider NWO project, I had the opportunity to interact with the industrial partners. I would like to thank the industrial representatives for their valuable feedback and input, during regular IPP meetings. I thank fellow bubbly flow PhD students: **Haryo**, **Aniruddha**, **Alessandro**, and **Biljana**, for interesting (technical)

conversations and for being the familiar fun faces during conferences and company visits. Thanks to NWO colleagues for organizing some amazing courses and helping out with the various administrative matters. **Joost** & **Maria**, without your timely support, I would have been struck in Sweden without a visa.

A part of my work involving electrolytes was in collaboration with Nouryon. **Bert Vreman**, thank you for both your scientific and industrial input during the project and for organizing discussions with various Nouryon experts. Symposiums and talks organized by Nouryon accounted for a significant part of PhD time travels. During my PhD time, I spent a couple of months as a trainee at the company's industrial site in Bohus, Sweden. **Johan Lif**, my company supervisor, it was a pleasure working with you and learning about the practical side of operating chlorate electrolysis columns. Thanks for your support with the experiments, that ultimately led to a nice scientific article. **Kalle**, **Mats**, and **Fredrik**, thanks for your warm Swedish hospitality, for the regular *fika* sessions, and for the tips to explore the Lapland. **Pavel**, our weekends, exploring Oslo and the neighbouring Gothenburg islands led to nice adventures. Thanks to the IAESTE community in Gothenburg, for organizing amazing social activities and *afterworks*.

Now, back to Delft, I had the privilege of having great colleagues at the TP group. I have had some fond memories, of discussing work and non-work things at the coffee-corner, and during borrels and lunch lectures. **Anand**, you were probably the only experimentalist by the time I arrived in the group. Thanks for your support in the Kramers Lab. I enjoyed our trip together to the ICMF conference in Florence. **Snehal**, you were the one I could discuss process technology and extraction techniques. Thanks for introducing me to North-Karnataka cuisine. **Romana**, you were an amazing officemate and fun to be around during conference parties, especially the Veldhoven ones. I can't remember ever having technical discussions with you. **Lorenz**, it was a pity that they had to take away your *megadesk*. **Annakaterien**, thanks for putting up with your noisy officemates and for the amazing cakes you brought to the office. **Hrushikesh**, no matter the weather, we couldn't see you without a winter jacket in the office. **Maulik**, you had a calming presence in the group, probably all antics were reserved for the PPE group. I will fondly remember my interactions with you and our time attempting to clear the *inburgeringsexamen*. It was nice to catch up with you in London. **Elin**, it was nice to see that you cared for general PhD life, except when it mattered for the TP cluster space. **Sid**, you were honestly the most creative and intelligent colleague, I have ever had. From photography to generative art or turbulence simulations, there was always something new to learn from you. Besides that, you made coffee breaks lively with your philosophical discussions and the occasional *Kanpuriya* logic. **Manu** cheta, you were always there to have a chat during impromptu coffee breaks and were always ready to help. But getting you away from your computer and movie-watching evenings was a tough task. A cycling trip to Rotterdam was all I could manage. **Cees**, you brought the energy to the group. At Borrels or at *Mario-Kart*, it was tough to go toe-to-toe with you. **Saeid**, I am still surprised that CBR didn't recognize your superior American driving skills. **Matheus**, it was fun to join parties with you and sing *vamos beber*, although I still await the famous Brazilian moves. **Shaurya**, your passion for science and *nasha*, both were equally contagious. Your molecular gastronomy ideas made your sense of humour bearable. If you ever write a cookbook, do send me a copy. **Karthik**, we have had lots of discussions about the life of an experimentalist, dealing with uncertainties and the occasional good

results. I am surprised our paths didn't cross during our times in NCL Pune, despite our common experiences. **Dries**, **Koen**, **Rudi**, and **Wenjie**, it was great to interact with you during my initial PhD days. **Corné**, although you left for Limerick by the time I joined the group, our similar topic and common experimental challenges led to some interesting discussions. Attending conferences in Brussels and Rio with you were some unique experiences. It was great to visit you and **Leila** in Dublin. Thanks for the Dutch summary translations in this thesis and for putting up with my broken Dutch over the years. **Kevin**, **Iman**, **Fei**, **Saidah**, **Xiaolin**, **Debasish**, **Jorrit**, **Aravind**, **Aswin**, and the large pool of M.Sc. and B.Sc. students the group hosted (a majority working with Sasa), thanks for the fun times and interesting conversations during the various TP activities. Many thanks to the secretaries of TP, **Anita**, **Jennifer**, **Fiona**, and **Sandra**, for helping me deal with the TU bureaucracy during my contract extensions.

For several years, I was part of YoungDelft, a TU Delft platform for organizing campus events and activities. For the fun times and the "unlimited" coins, I would like to acknowledge my fellow board members: **Alessandro** (a.k.a. Apulian Santa), **Tomasz**, **Christian**, **Anna**, **Anne**, **Claire**, **Roberto**, **Hamid**, and **Maideh**. Collectively, we came up with unique ideas to gather TU employees (besides the obvious free-drinks at PSOR): city trips, distributing ice creams, bowling, comedy shows, and karaoke. **Victor**, we had some nice borrels in the botanical garden and a great time organizing the DPTI event. It was an honor to be at your wedding. **Motassem**, my first flatmate in Delft, it was fun solving large jigsaw puzzles with you and your Syrian friends, and learning about the Middle Eastern cuisine. **Adi**, a classmate from masters and later a colleague at Delft, it is always a pleasure to catch up with you during my occasional visit to Ghent, and reminisce over the fun times. Let's hope Netflix doesn't crack down on password sharing.

Corona pandemic had an impact on social life, having great company (with ever-changing regulations) made it bearable. **Rumen**, your board game nights were enjoyable. You came in very handy decoding Cyrillic characters in *geoguessr*. **Uttiya**, your knowledge of science and politics triggered some lengthy evening debates, of course, paired with some good cooking lessons. **Luis**, **Ursa**, thanks for all those memorable evenings in Den Haag. **Stephan**, **Noura**, **Fatima**, and **Rishabh**, thanks for joining our multicultural bubble at various times. I particularly enjoyed our trip to Veluwe. **Anna**, **Carlos**, you redefine the limits of *pasqualizing* with your partying skills. There was never a dull moment with you being around. **Kosta** & **Ines**, we had some memorable evenings at your or my place and during our trips to Ardenne and Cologne. It was a pleasure to host you and Fras' at my wedding in India. Kosta, a fellow TPer, our bond goes beyond being just colleagues. Ines, "it is nice" to see that you find fun in doing little things. **Francesco** e **Francesca**, my southern *Ragazzi* and my moving company, we have shared countless fun moments over the years. I learned a great deal about Italian culture from you. *Grazie di tutto*! Francesco, I still can't believe how quickly you acclimatized to spicy food and bargaining skills in India. Wait till I am in Puglia! How to not mention the famous Italian co-host for the parties and my flatmate for a long time during the PhD time, **Simone**. It was amazing living with you in Van Embdenstraat. *Gli anni delle immense compagnie.* Thanks for the memorable trip to Milan (San Donato). If you are done experiencing American freedom, hope to see you back in Europe!

Surviving a decade in the Netherlands wouldn't have been possible without amazing Indian friends. **Naveen** & **Mitava**, we have followed each other around the country,

from Enschede to Delft and now to Eindhoven. Besides countless memories, thank you for often being on the other side of the phone offering advice. **Kartikeya** & **Harshitha**, proficient *mafia* duo, thank you for your warm hospitality, a pleasure to be at your place for the various dinners and chai-pe-charcha sessions. **Alka** & **Sumit**, thank you for some pleasant evenings and for dealing with my drilling mishaps. Sumit, thanks for introducing me to some "amazing" Punjabi music. **Aditya** & **Karthika**, I can't decide who is a better cook. Let's figure it out during our next meetup in Veldhoven. **Deva**, our yearly cycling trip to Zeeland and penchant for watching *bhai* ka movies made for some great memories. **Vasu**, making music videos with you kept me at my creative best. **Himanshu**, thanks for hosting me in Stockholm during my visit. **Poorvi**, your escapades during the Iceland trip with the group are one for the books. **Pramod-ji**, **Vishaka-ji**, **Ambati**, **Sangeeta**, thank you for your support over the years.

Acknowledgements wouldn't be complete without mentioning my friends from Enschede. For over a decade, we have shared common experiences in the Netherlands, with epic trips and yearly *thou shall not miss* gatherings. **Apurv**, all our midnight talks, though often inconclusive, are always fun. **Wiebke**, thank you for your warm German hospitality and for dealing with the shenanigans of me and Apurv. My northern lights trip in Sweden wouldn't have been possible without your support. **Patil**, your quips add to the charm of the gatherings, though often are just true translations from Marathi. Our epic adventures in Berlin, Spain, and Portugal shall not be forgotten. **Linh**, with some amazing Vietnamese food and K-pop music, you are a perfect antidote to Patil and fun to be around. **Pakhira**, the *belle-of-the-ball*, no gatherings are complete without stories of your adventures. Road trips are always amazing with you, discussing anything from the stock markets to the meaning of relationships. That is unless my car breaks down. **Anirudh**, our year-end gatherings at your place in Enschede are always fun, paired with some amazing Arabic music and the cooking skills of **Pavani**. **Vinayak**, **Ateeth**, **Suma**, **Naveen**, **Dipankar**, **Praneeth**, and **Vikram**, thanks for countless fun memories over the years.

Most importantly, I would like to thank my family for their love and support during all these years of me being away from home. I am grateful to my sister, **Vaishnavi**, for her unconditional support over the years and encouragement in my pursuits. Now that you moved to Germany, we can continue our common interests of exploring cities and watching Telugu cinema. *Atluntadi manathoni!* Words are certainly not enough to express gratitude to my parents who have sacrificed their lives for providing me and my sister a good education and a decent living. **Amma** and **Nanna**, thank you for everything. And finally my wife **Vasudha**. Thank you for your love and support. Balancing work and finalizing this thesis wouldn't have been possible without your encouragement. While this academic chapter nears its end, I can't wait for our next adventures together!

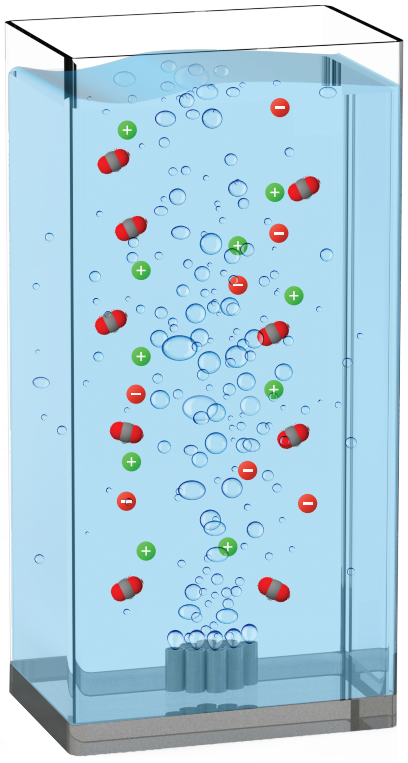

TU Delft Delft University of Technology

ISBN: 978-94-6384-587-8